Search for gravitons using merged jets from Z boson decays with the ATLAS experiment

Alexander Penson

Submitted in partial fulfillment of the
requirements for the degree
of Doctor of Philosophy
in the Graduate School of Arts and Sciences

COLUMBIA UNIVERSITY

2012

ABSTRACT

Search for gravitons using merged jets from Z boson decays with the ATLAS experiment

Alexander Penson

A search is presented for anomalous production of a pair of gauge bosons (ZZ or WZ) from the decay of a narrow massive resonance. Data corresponding to 2.0 fb^{-1} of integrated luminosity collected by the ATLAS experiment from proton-proton collisions at $\sqrt{s} = 7$ TeV. Events with two charged leptons and either two resolved jets or one merged jet are analyzed and found to be consistent with the Standard Model background expectation.

In the absence of an excess, lower limits on the mass of a resonance are set using the original Randall-Sundrum (RS1) model as a benchmark. The observed (expected) lower limit on the mass of an excited graviton decaying to ZZ is 870 (950) GeV at 95% confidence level. Limits are also set on a more recent version of the Randall-Sundrum model where Standard Model particles are allowed to propagate in the five dimensional bulk. An excited graviton in this model is excluded for masses between 500 and 630 GeV.

Table of Contents

List of Figures

List of Tables

Acknowledgments

I am very grateful to my supervisor Gustaaf Brooijmans for encouraging me to challenge myself and helping me to work on interesting topics. Many thanks also to John Parsons for guidance and help especially when I got to CERN. I got a lot of help from the Columbia ATLAS group. In particular, thanks to my classmates Dustin Urbaniec, Eric Williams and Evan Wulf and to Emily Thompson and Tim Andeen for helping me to find my way and for really detailed comments.

It was a pleasure to work with Koji Terashi and Thomas Gadfort, who consistently made me feel valued. I'm also grateful to the members of the ATLAS Collaboration that have made this all possible, it is an honor to work on such a fine experiment. I took inspiration from others when starting to write; thanks to Doctors Andeen, Caughron, Copic, Gray, Hooberman, Jen-La Plante, Lopez, Marshall, Miller, Ohm, Perez, Scherzer, Thompson & Tuggle. I am also much indebted to Flip Tanedo for some excellent explanation of extra dimensions.

I am very grateful to have met so many good friends while in New York and Geneva, thanks guys! I would like to thank my parents for all they have given me in the past and more specifically for asking great questions about particles when work was going well and for encouragement when it was not. Finally, I thank Ceri Perkins for challenging me to explain myself clearly, I look forward to many more adventures together.

for Ceri and my family

Introduction

The Standard Model (SM) of particle physics has provided a staggeringly accurate description of the results of particle physics experiments ever since it was developed in the 1970s. However, the description cannot be complete for particle interactions at energies much higher than those that have been studied so far. The Large Hadron Collider (LHC) is colliding protons with energies at which some of the shortcomings of the SM should finally become apparent. ATLAS is one of two all-purpose detectors at the LHC that will make precise measurements of the particles produced in LHC collisions.

Of the new physics models that address limitations of the SM, a prominent subset postulate warped extra dimensions. Since the original Randall-Sundrum model (RS1) was proposed, it has evolved to address several other limitations. One of the defining features of both the original and updated models is graviton excitations which, depending on their mass and interaction strength, could be produced and observed at the LHC.

The decay properties of the excited graviton depend on the nature of the extra dimension. The search described in this thesis is sensitive to the production of a pair of gauge bosons (ZZ or WZ) from the decay of any narrow massive resonance; with one Z boson decaying leptonically (to electrons or muons) and the other boson decaying hadronically. The dominant SM background process is Z+jets, although other processes contribute. No significant excess over the background expectation is found and new limits are set on the mass of excited gravitons decaying to a pair of Z bosons.

Chapter 1

The Standard Model

The Standard Model (SM) is a concise and consistent statement of current knowledge of fundamental particles and their interactions which was developed by unifying many successful physics theories. The SM describes the electromagnetic, weak and strong forces by requiring the conservation of electric charge, weak isospin, strong color charge, energy and momentum. It is a quantum field theory (QFT) based on gauge symmetry groups. QFT divides particles into two very distinct categories, fermions and bosons, according to their intrinsic angular momentum or spin [1].

Fermions Fermions have spin 1/2 which means that two fermions cannot occupy the same quantum state simultaneously, known as the Pauli exclusion principle. As a result, fermions are usually associated with matter. All the visible matter in the universe is made of electrons, protons and neutrons. Protons and neutrons are made of up and down valence quarks. The first generation of fermions in the SM consists of a pair of quarks: up and down quarks and a pair of leptons: the electron and its neutrino.

In total there are three generations, which means six quarks and six leptons, plus their antiparticles. There are three charged leptons (electron, muon and tau) and their corresponding neutrinos (ν_e, ν_μ and ν_τ). The quarks are divided into three up-type quarks (up, charm and top) and their corresponding down-type quarks (down, strange and bottom). As a result of their spin, fermions have either a left-handed or

right-handed chirality. This is particularly relevant for the weak interaction, which couples only to the left-handed component. Right-handed neutrinos do not interact and therefore cannot be seen.

Bosons Bosons have integer spin and mediate forces between matter particles. In atoms, electrons are bound to protons electromagnetically. Protons and neutrons are bound together with the strong force. Neutrinos interact only via the weak force, which is responsible for nuclear radiation.

The photon γ mediates the electromagnetic force and interacts directly only with particles with electric charge. The W and Z bosons carry the weak force. The gluon g mediates the strong force between particles with color charge. The particles in the SM are listed in Table 1.1 and their masses can be compared in Figure 1.1. The rest of the section will explore the forces described by the SM.

Electromagnetism Quantum electrodynamics (QED) can describe the interaction of electrons and photons with the help of Feynman diagrams. Feynman diagrams are used as shorthand for the mathematical calculation of the probability of a process. In principle, contributions from all possible diagrams can be combined to give the probability amplitude for the process as a function of the properties of the incoming and outgoing particles. This is referred to as the matrix element in QFT. For many processes, it is only possible in practice to include the diagrams making the largest contributions. Often 'tree level' or 'leading order' diagrams without loops are the most important, followed by 'loop corrections'.

Loop diagrams can also provide corrections to mass and energy via the probability of a particle travelling from one point in spacetime to another. Figure 1.2 shows an electron self-interaction diagram which gives an infinite contributions to the energy and mass of the electron. This problem can be solved by redefining the electron's mass in terms of finite and measurable 'dressed' quantities which include these infinite contributions; a 'dippy process' [3] known as renormalization.

Other loop diagrams give similar infinite contributions to the electron's charge. Renormalization of charge leads to an increase in the interaction strength or coupling

Particle	Symbol	Charge (e)	Mass (GeV)
quarks (spin 1/2)	q		
up	u	$+2/3$	$(1.5 - 3.3) \times 10^{-3}$
down	d	$-1/3$	$(3.5 - 6.0) \times 10^{-3}$
charm	c	$+2/3$	$(1.16 - 1.33)$
strange	s	$-1/3$	$(70 - 130) \times 10^{-3}$
top	t	$+2/3$	172.9 ± 1.5
bottom	b	$-1/3$	$4.20^{+0.17}_{-0.07}$
leptons (spin 1/2)			
electron	e	-1	0.511×10^{-3}
electron neutrino	ν_e	0	$< 0.46 \times 10^{-6}$
muon	μ	-1	105.7×10^{-3}
muon neutrino	ν_μ	0	$< 0.19 \times 10^{-3}$
tau	τ	-1	1.7768 ± 0.00017
tau neutrino	ν_τ	0	$< 18.2 \times 10^{-3}$
gauge bosons (spin 1)			
photon	γ	0	0
W^+ boson	W^+	$+1$	80.4 ± 0.03
Z boson	Z	0	91.2 ± 0.002
gluon	g	0	0
bosons yet to be discovered			
Higgs boson (spin 0)	h	0	$115 \lesssim m_h \lesssim 130$
graviton (spin 2)	G	0	0

Table 1.1: Particles in the SM.

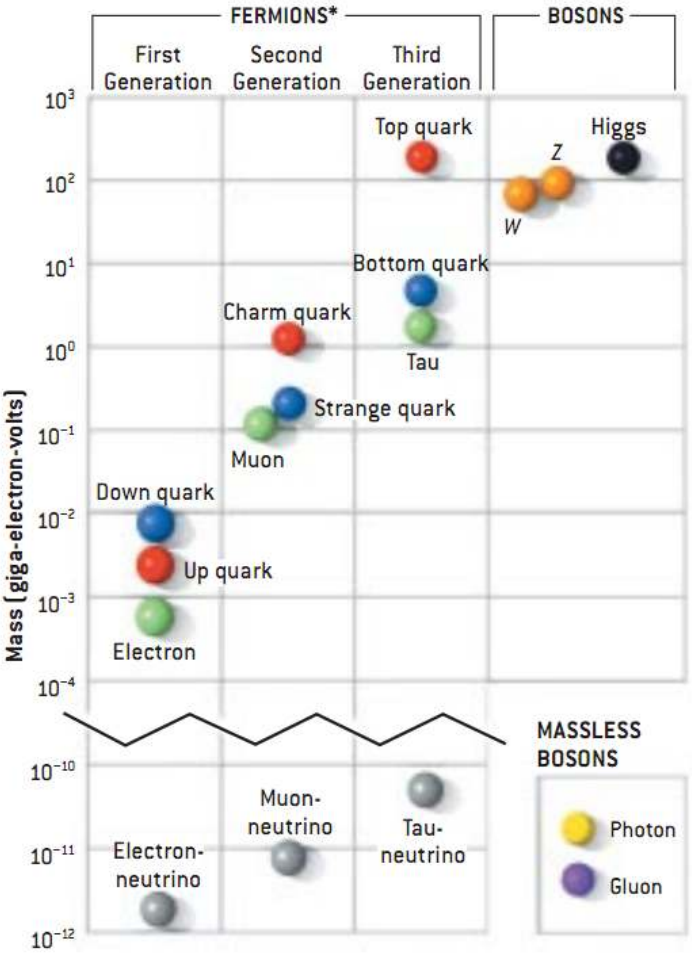

Figure 1.1: The masses of particle in the SM. [2].

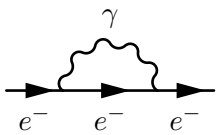

Figure 1.2: A Feynman diagram of electron self-interaction. It is a divergent diagram, giving an infinite contribution to the electron mass and energy. However, it can be fully described in QED by renormalization.

as a function of the energy of the interaction, referred to as a 'running' coupling; it can be visualized as follows. At an e^+e^- collider, the higher the electron energy, the shorter the distance of closest approach between the particles. The closer that the positron gets to the electron, the less it is 'screened' and the higher the coupling of the interaction. Note the inverse relationship between the distance and energy scales of the interaction.

Loop corrections were first used in the 1940s, in the explanation of the Lamb shift [4] between the $^2S_{1/2}$ and $^2P_{1/2}$ energy levels of hydrogen [5] in the 1940s. They are essential in all precise QED predictions, epitomized by the muon magnetic moment g_μ which deviates from exactly two as a result. The most recent predictions of g_μ involve more than a thousand QED Feynman diagrams with four loops, a few thousand of the most important five-loop diagrams and loops involving hadrons and weak bosons. The muon magnetic moment can be measured very precisely using the change in the decay angle of muons as they precess in a magnetic field [6]. The extent to which g_μ deviates from exactly two, $a_\mu = (g_\mu - 2)/2$, as given by theory and experiment is:

$$\begin{aligned} a_\mu^{\text{exp}} &= (116592089 \pm 63) \times 10^{-11}, \\ a_\mu^{\text{theory}} &= (116591802 \pm 49) \times 10^{-11} \text{ such that} \\ a_\mu^{\text{exp}} - a_\mu^{\text{theory}} &= (287 \pm 80) \times 10^{-11}, \end{aligned}$$

which is a 3.6σ discrepancy [7]. Loops involving particles beyond the SM could cause the measured value to deviate from the theoretical prediction. The close agreement places what is known as an 'electroweak precision constraint' on new physics models.

Weak Force The weak force is unique among the fundamental forces in several ways: it is carried by massive particles, which limits its range; it couples only to left-handed fermions - this is a peculiar feature of weak interactions - meaning that the mirror-image of a weak interaction does not occur; and it allows 'flavor changing'. In nuclear beta decay, for example, the flavor of a quark is changed via interaction with a charged W boson.

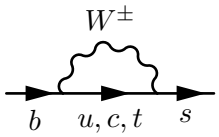

Figure 1.3: Flavor-changing neutral currents in the Standard Model.

However, flavor changing *neutral* currents (FCNCs) are heavily suppressed in the SM, in excellent agreement with experimental results [8]. FCNCs can only proceed via the weak interaction and all relevant Feynman diagrams, including Figure 1.3, contain loops; as a result of the couplings of the W and Z bosons rather than any symmetry. The probability amplitudes represented by diagrams with loops include an extra factor of the weak coupling coefficient. Since the weak coupling coefficient is small, loop diagrams are suppressed. FCNCs are further suppressed by cancellations between the contributions of u, c and t quarks in Figure 1.3, in what is known as the GIM mechanism [9]. Suppressing FCNCs can be a significant challenge for new physics models, since contributions to their probability from all possible diagrams including new particles must also be included.

Strong Force The theory of the strong force, known as quantum chromodynamics (QCD), was developed to explain how hadrons are composed. The observed hadrons are: mesons made of quark-antiquark pairs, baryons comprising three quarks, antibaryons comprising three antiquarks and nuclei made up of baryons; free quarks are not observed.

Although the strong force is described in a similar way to the electromagnetic and weak forces, unification of all three forces, known as grand unification, has not yet been possible; the strong force has a different coupling and a different gauge

group: $SU(3)_{color}$. As triplets of this group, quarks carry one of three color charges - red, green or blue; as antitriplets, antiquarks carry anticolor. Quarks are bound together in hadrons which must be in a color neutral singlet state. The strong force is carried by gluons g, which couple to color charge. In contrast to the photon, gluons are themselves 'charged' - they carry a color and an anticolor - and couple to each other.

The attraction between two quarks - proportional to the coupling of the strong force - also depends on energy but, unlike electromagnetism, it is stronger at *lower* energies and *larger* distances[1]. This results in color confinement. As two quarks are separated, it becomes energetically favorable for a new quark-antiquark pair to spontaneously appear, creating new hadrons. In a high energy proton collision, this process is repeated many times producing a shower of hadrons known as a jet.

At low energies the strong coupling is so large that Feynman diagrams with (many) loops become significant, making calculations intractable. Precise calculations, using a finite number of Feynman diagrams, can only be made if the energy of the interaction is greater than the QCD scale $\Lambda_{QCD} \sim 200$ MeV. Mesons and baryons only interact as distinct composite particles below this scale; above it, the interactions of individual quarks become dominant.

Higgs Mechanism In the SM, the Higgs mechanism gives mass to the W and Z bosons [10, 11, 12], and is necessary to regulate scattering of W and Z bosons. The probability of this interaction without the Higgs boson - including Figure 1.4a but not including Figure 1.4b - increases with increasing energy and becomes strongly coupled at an energy scale of around one TeV. At this point, diagrams with many loops become significant and once again calculation becomes impossible. If this was the case, analogy with the strongly coupled strong force suggests it ought to be possible to see the first signs of substructure in the W and Z bosons close to this energy scale. Since no substructure has been observed, a Higgs-like mechanism is assumed.

[1] This can be visualized as two quarks connected by a rubber band.

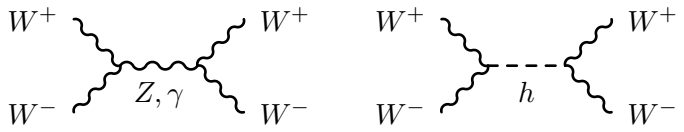

(a) via a Z or γ boson. **(b)** via a Higgs boson.

Figure 1.4: Two diagrams that contribute to WW scattering in the SM

1.1 Limitations of the Standard Model

The SM describes particle physics experimental results in precise detail, encompassing not only the features of particle interactions that it was designed for but also, seemingly accidentally, phenomena such as proton stability and FCNCs. However, the SM is also limited in a number of ways. Both in what it can explain and its internal consistency.

Gravity The SM does not include gravity. Direct effects of gravity on particles at collider experiments are utterly negligible. The current best theory of gravity, General Relativity, is incompatible with the SM; since it depends on *absolute* energies gravitation cannot be renormalized. The only known way to reconcile the two is string theory.

The Hierarchy Problem The Higgs boson solves one problem of the SM but creates another. By design, it couples to all particles with mass. Following renormalization, the physical mass of the Higgs boson should get contributions on the order of the largest relevant mass scale. The largest contribution from known particles is from the top quark via the diagram in Figure 1.5. The contribution from any such fermion is given by:

$$\Delta m_H^2 = -\frac{|\lambda_f|^2}{8\pi^2}\Lambda_{UV}^2, \tag{1.1}$$

where λ_f is the coupling of the fermion to the Higgs boson, proportional to the fermion mass. The ultraviolet cutoff Λ_{UV} is used to regulate the loop integral; it must extend at least as far as the theory is valid. In the SM, this is typically taken

to be the energy scale of grand unification or of gravity (the Planck scale), where the effects of quantum gravity become significant.

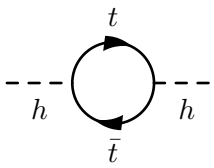

Figure 1.5: The first-order correction to the Higgs mass from a top quark loop.

The required small positive physical mass of the Higgs boson, after loop corrections, can be arrived at in a number of ways. One way would simply involve 'fine-tuning' enormous loop corrections, but this is generally considered implausible and a little distasteful. Another way is to introduce a new symmetry, such as supersymmetry, that requires large loop corrections to cancel one another. A third possibility - as considered in this thesis - is that the corrections are in fact small because the fundamental scale of gravity, instead of being enormous, is on the TeV scale.

Dark Matter There is a large and robust discrepancy between the mass of galaxies as determined from (a) their gravitational effects and (b) the visible luminous matter they contain: stars and hot gas and dust [13, 14]. The missing mass is known as dark matter. Estimates of the distribution of dark matter in the universe come from detailed measurements of cosmic microwave background (CMB) radiation.

Ordinary matter such as astronomical bodies and neutrinos can only account for a small fraction of the observed discrepancy. Explanations involving alternative theories of gravity or large numbers of small black holes have not become accepted by the broader physics community. There is a consensus among cosmologists that dark matter is mostly due to an as-yet-unknown heavy particle, the existence of which is a strong argument for particle physics beyond the SM.

Dark matter particles do not have to only interact gravitationally. If they interact via the weak force, like almost all known particles, they could be detected. Dark matter particles may even be produced directly at collider experiments.

Other Limitations The SM has several other limitations, and there are a number of open questions that an extended model might hope to address:

- The SM requires about 30 input parameters (masses, mixing angles and couplings) which cannot be calculated.
- The values of some of these parameters are quite puzzling. For example, similar particles in different generations cover a very wide range of masses, as shown in Figure 1.1, with no obvious explanation for why.
- The precise neutrality of atoms seems to imply an unexplained symmetry between quarks and leptons.
- The vast preponderance of matter over antimatter in the universe seems to be inconsistent with the persuasive assumption that equal amounts of each were produced in the Big Bang. The amount of CP violation in the SM alone cannot account for the large matter-antimatter ratio observed in the universe.
- Neutrinos are curious not only because of their small - but - non-zero masses; they may allow CP violation in leptonic interactions.

Chapter 2

Gravitons and Extra Spacetime Dimensions

In the early 1900s, Einstein's theory of Relativity forced physicists to start thinking of time as the fourth dimension of spacetime. There has been speculation about extra spacetime dimensions ever since. Extra dimensions could provide an elegant explanation for why gravity is so much weaker than the other forces, i.e. a way to address the hierarchy problem. Einstein's theory of gravity, General Relativity, fails to work at very high energy scales or put another way at very short distance scales, when the effects of quantum mechanics become significant. String theory is the only known way to reconcile the two but is only consistent if there are many extra dimensions.

If extra dimensions exist, it is natural to ask why we cannot see them. An extra dimension could be curled up ('compactified') with radius too small to be observed. In some models, as the ones to be discussed here, the extra dimension can have an endpoint. The edge of the proposed five dimensional space has the familiar four spacetime dimensions; analogous to the 2D square faces of a 3D cube.

Three dimensions of space are all that we readily experience, but given that extra dimensions could be compactified, or that particles could be localized in our 4D world - that is, restricted to be on the edge, generally referred to as a 'brane' -

how do we know that there are only three? There is a natural connection between the Newtonian equation for gravity $G_N m_1 m_2 / r^2$ and the three dimensions of space. The gravitational force of mass at a point in space acts equally *in all directions*. The density of the straight gravitational force lines then determines the strength of gravity. In three dimensions of space, this is proportional $1/r^2$. This inverse square relation is also true for electromagnetism, which is equivalently described by the emission of stable, massless particles - photons - in all directions. Gravitons, which transmit gravity, are postulated because of the great success of QFT at describing all other known forces via the exchange of elementary particles. Like photons, they must be stable and massless. The strength of gravity is proportional to the constant of gravitation $G_N = (10^{-35}\ \mathrm{m})^2$ using 'natural units'. The extremely small 'distance scale' of gravity is equivalent to the extremely large Planck energy $m_{Pl} \sim 2 \times 10^{18}$ GeV[1].

In quantum mechanics, when a particle is confined in space, the momentum in the direction of confinement becomes quantized - it may take only certain discrete values. In the models considered, the graviton, and other particles that propagate in the extra dimension, therefore acquire 'excited modes' also referred to as Kaluza-Klein (KK) modes [15, 16].

2.1 The Randall-Sundrum Model

The Randall-Sundrum (RS) model as it was originally proposed [17] is often referred to as RS1. It involves a thin slice of five-dimensional space, with two four-dimensional edges or 'branes'. Branes can carry energy or tension, and in the RS1 model one brane has positive tension and one has negative tension. A large negative cosmological constant, or bulk energy, is also assumed.

Under these conditions, the solution to Einstein's equations is a space with strong negative curvature, known as anti-de Sitter (AdS) space. It is 'warped' meaning that it is only curved in one dimension. Both branes remain flat; in fact, the 5D space

[1]The reduced Planck scale is used.

can be thought of as made up of many flat 4D layers. The difference between each layer is the inherent distance scales: an object would be much smaller on one brane than on the other! This difference in distance scale corresponds to a difference in energy scale between the branes. The energy scale of gravity on the brane with positive tension is assumed to be the Planck scale, and it is therefore referred to as the Planck brane. The energy scale of gravity on the brane with negative tension is dramatically reduced by the warping.

The geometry of the space is defined by a metric; the 'line element' $\mathrm{d}s$, which determines the arc length of a curve, is given by:

$$\mathrm{d}s^2 = e^{-2ky}\eta_{\mu\nu}\mathrm{d}x^\mu \mathrm{d}x^\nu - \mathrm{d}y^2 \tag{2.1}$$

where:

- $\eta_{\mu\nu}$ is the Minkowski metric for flat 4D space, $\mathrm{diag}(-1, 1, 1, 1)$;
- x^μ are the familiar four dimensions of spacetime ($\mu = 0, 1, 2, 3$), with $x^0 = t$;
- $0 \leq y \leq \pi r$ is the fifth dimension, where r is the size of the fifth dimension;
- k^{-1} is the fifth dimension's radius of curvature, assumed to be on the order of the Planck scale.

Within this spacetime, two types of fluctuations are possible: fluctuations of the metric and fluctuation of the size of the extra dimension r. In QFT these fluctuations are associated with particles - the graviton and the radion, respectively. The graviton is highly concentrated near the Planck brane, as shown in Figure 2.1.

The energy scale of gravity on the brane with negative tension is reduced by a factor $e^{-k\pi r}$. This can be around one TeV - as required to address the hierarchy problem - by choosing values of k and r such that $kr \sim 11$. SM particles are 'localized' on this brane, which is referred to as the TeV brane. Other pairs of names are often used for the branes including: the UV and IR branes or the gravity and weak branes. Since the graviton is confined in the fifth dimension it will acquire excited KK modes, whose masses and couplings will depend on the size and warping of the extra dimension.

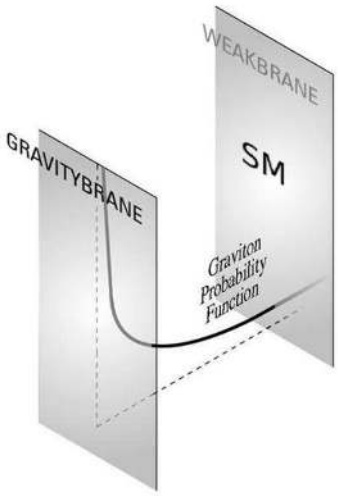

Figure 2.1: Graviton distribution in the RS1 model. The fact that the graviton's wave function is concentrated on the Planck (gravity) brane, away from the SM explains why gravitational interaction between SM particles is weak.

The main motivation for the RS1 model is that it can reduce the energy scale of gravity close to the scales of the other known forces. This means that the physical mass of the Higgs boson does not receive enormous loop corrections. Another strong motivation comes from the conjecture of AdS/CFT correspondence [18, 19]. This states that any model in warped AdS space has a equivalent ('dual') 4D interpretation. The 4D dual of the RS1 model is strongly coupled. Strongly coupled 4D theories, like QCD, are certainly more established than extra dimensional theories but they are generally less calculable. Warped models offer a new way to describe strongly coupled theories.

2.2 Stabilization

In the RS1 model, the problem of understanding the hierarchy of Planck and TeV scales is translated into understanding the size of the extra dimension. A mechanism that can stabilize the size is essential if the theory is to be viable.

The mostly commonly cited mechanism was proposed by Goldberger-Wise [20],

although other stabilization mechanisms have been suggested [21, 22]. In the Goldberger-Wise mechanism, the radion gains mass and its interactions are localized on the two branes. This stabilizes the extra dimension at a size appropriate for solving the hierarchy problem. The stabilized RS1 model has been shown to be consistent with cosmological observations [23] and may even provide a mechanism for cosmological inflation [24, 25]. The couplings of the radion are similar to those of the Higgs boson. Mixing between these two particles could have a variety of observable consequences [26].

2.3 Standard Model particles in the five-dimensional bulk

The RS1 model offers an elegant and consistent solution to the hierarchy problem. However, in the years since it was proposed, theoretical effort has focussed on variants that allow SM particles to propagate in the five-dimensional bulk rather than being localized on the TeV brane. These models are able to address several other limitations of the SM [27, 28].

The first proposals allowed gauge bosons to propagate in the bulk [29]. Gauge bosons do not make a large contribution to the bulk energy density. They are not concentrated near the Planck brane like the zero-mode graviton; their profile is roughly flat. Furthermore, since the extra dimension is small, the gauge bosons' strength is not diluted. In this model, all gauge bosons can access Planck energy scales and it has been shown that grand unification of the 5D gauge couplings is possible both with and without supersymmetry [30, 31] .

One of the problems with allowing gauge bosons in the bulk is that the coupling of the KK modes to SM fermions produces FCNCs [32, 33], but these can be heavily suppressed by allowing SM fermions in the bulk as well [34, 35]. The Higgs boson must remain on the TeV brane in order to solve the hierarchy problem.

SM fermions in the bulk have exponential probability density distributions (profiles) in the extra dimension. They are concentrated either on the Planck or TeV

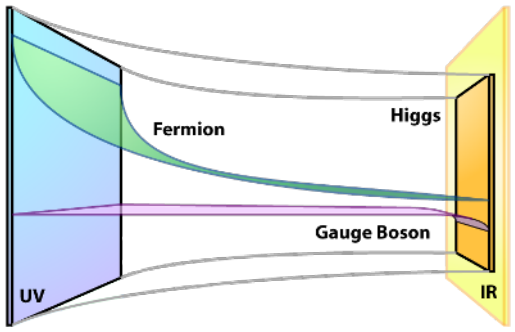

Figure 2.2: SM particles in the 5D bulk. The profile of a light fermion is shown; concentrated near the Planck (UV) brane. This is similar to the profile of the zero-mode graviton. The Higgs boson is localized on the TeV (IR) brane [36].

brane. Fermion masses are still determined by Yukawa couplings to the Higgs boson, which is localized on the TeV brane. A fermion concentrated on the Planck brane, as shown in Figure 2.2, will therefore be light. This exponential feature is able to generate the observed range of fermion masses, over several orders of magnitude, with a few numbers of order one. Neutrino masses can also be explained [37, 38]. FCNCs that were a problem without bulk fermions are suppressed as a result of the small overlap of light fermions with the TeV brane.

The 4D dual description of bulk RS models is also compelling. Every particle has an equivalent in the 4D theory - either an elementary particle, a composite particle or a mix of the two, analogous to the mixing of the composite ρ meson with the elementary photon. Bulk particles concentrated near the Planck brane will have mostly elementary equivalents in the 4D theory. The Higgs boson, localized on the TeV brane, has a fully composite equivalent. Bulk RS models are conjectured to be dual to well-studied theories with composite Higgs bosons [39, 40, 41]. Note that in 4D dual theory of the RS1 model all particles are fully composite.

Despite their advantages, bulk RS models are generally not consistent with all electroweak precision tests [42], specifically they give large contributions to the Peskin-Takeuchi T-parameter [43]. They also tend to give excessive corrections to the $Zb\bar{b}$ coupling in particular. This can be solved by imposing 'custodial' symmetries [44, 45]. Without further model-building, electroweak precision constraints

prefer heavy graviton KK modes: $m_{G^*} \gtrsim 3$ – 4 TeV.

Several consequences of bulk RS models are observable at the LHC [46]. The KK graviton does not couple to photons, by orthogonality, and its couplings to the light fermions are heavily suppressed; light fermions are concentrated near the Planck brane while the KK graviton is concentrated near the TeV brane - like all KK modes of all bulk particles. The production cross section of the KK graviton is reduced relative to the RS1 model, since the coupling to light quarks is small and production via gluon fusion dominates. Decays to pairs of heavy particles, $t\bar{t}$, WW, ZZ and perhaps Higgs bosons are preferred; for some sets of parameters, the branching fraction to ZZ dominates [47]. These models are characterized by the decay of the graviton to longitudinally polarized gauge bosons. In the laboratory frame, this tends to lead to a large opening angle between the two leptons from the decay of high p_T Z bosons. The precise bulk RS signal model used in this thesis was defined by Agashe et al [48].

KK modes of other particles in the five dimensional bulk may well be observed before a KK graviton. For example, KK gluons in a bulk RS model decay predominantly to a pair of top quarks [49, 50].

2.4 Previous Searches

The most recent limit on the mass of the KK graviton in the RS1 model was published by the ATLAS experiment at the LHC using up to 5.0 fb^{-1} data in the dilepton channel [51]. With values of the relevant coupling $k/m_{Pl} = 0.1(0.01)$, a KK graviton with mass below 2.16 (0.91) TeV is excluded at 95% confidence level (CL). Dilepton results such as this one can be combined with diphoton results to increase sensitivity [52].

Other decay channels are important, especially in bulk RS models where the easily detectable dilepton and diphoton decay channels of the KK graviton tend to be suppressed. In order to compare results using different decay channels at different colliders, the RS1 model with $k/m_{Pl} = 0.1$ is used as one benchmark.

The most stringent limits on the masses of WW and WZ resonances were published by the D0 experiment at the Tevatron, with 5.4 fb^{-1} data combining $\ell\nu\ell\ell$, $\ell\nu jj$ and $\ell\ell jj$ channels [53]. A KK graviton decaying to a pair of W bosons is excluded at 95% CL in the mass range 300 – 754 GeV.

The ATLAS experiment published a search in the ZZ channel with 1.0 fb^{-1} data combining the $\ell\ell\ell\ell$ and $\ell\ell jj$ channels [54] including work done in the context of this thesis. A KK graviton in the mass range 325 – 845 GeV is excluded at 95% CL. Observed (expected) limits are set on cross section times branching ratio $\sigma \times \mathrm{BR} < 360$ (300) fb in the mass range 1 – 1.5 TeV. This thesis further builds on this publication.

A search for a KK gluon decaying to a pair of top quarks in a bulk RS model, to be published by the ATLAS experiment with 2.1 fb^{-1} data, excludes a mass range of 500 – 1025 GeV at 95% CL [55].

Chapter 3

The Large Hadron Collider

The LHC [56] is a 7 – 14 TeV[1] proton-proton collider. It has drawn on technology from a long legacy of particle accelerators [57, 58] which have aimed to make as much energy as possible available for the creation of new high mass particles. Equally important for the quest to create and observe particles that have not been seen before is maximizing the number of proton collisions.

Colliders like the LHC - which collide two beams, rather than firing a single beam at a fixed target - are built because, in principle, all of the beam energy is made available. The disadvantage of the collider approach is that only a tiny minority of protons collide each time the beams cross. However, the LHC is a ring, as seen in Figure 3.1, which means that the same beams can be brought into collision at each revolution. Two counter-rotating beams can be kept circulating for many hours, as long as the loss of particles can be kept small. Due to the extremely high vacuum in the beam pipe, the loss of particles from collisions with residual gas is much lower than the loss from beam-beam collisions.

3.1 Collision Energy

The ring design is also essential in maximizing the beam energy. The rate at which particles can be accelerated in a straight line using superconductors is limited by the

[1] 1 eV is the energy given to a proton by an accelerating voltage of 1 V

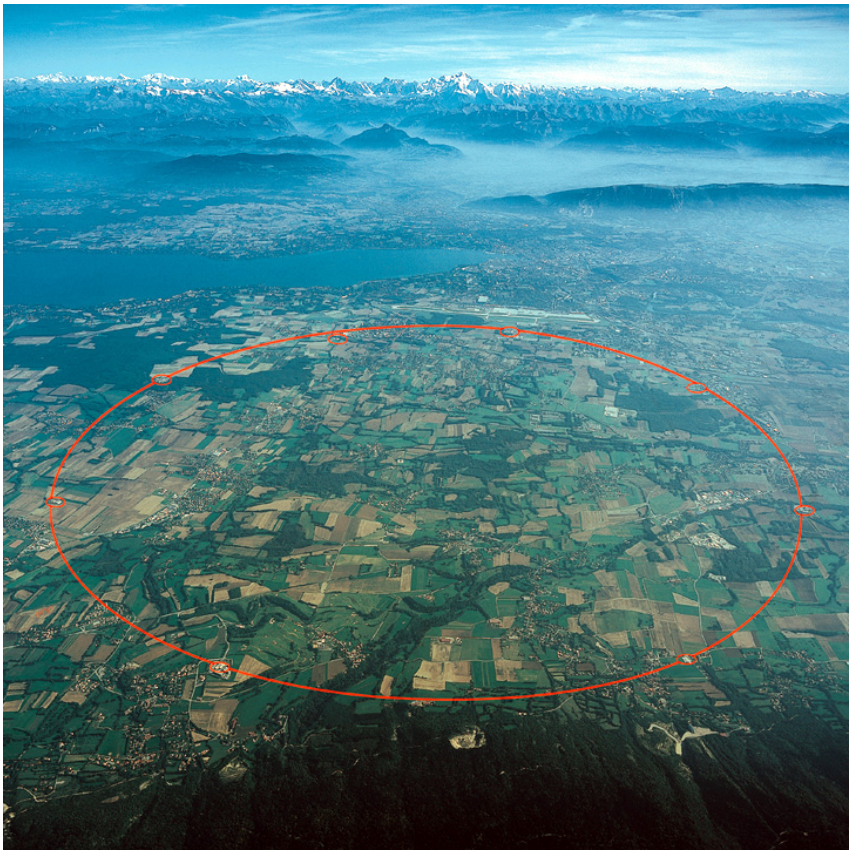

Figure 3.1: The LHC is built underground between Lake Geneva and the Jura mountains over which this photo was taken. Geneva airport can be seen just behind the accelerator. The French Alps including Mont Blanc are in the background. The ATLAS detector and main CERN campus are at about 2 o'clock.

strength of electric field that they can support. While orbiting the LHC, protons are accelerated by the same components millions of times.

The energy of proton beams is then limited by the ability to confine it in a circle. The maximum energy is proportional to the size of the accelerator and the strength of the magnetic field used for bending the beams:

$$E = 0.3Br, \tag{3.1}$$

where:

- E is the proton energy in TeV,

- B is the magnetic field in T and
- r is the radius of curvature in km.

The LHC is therefore as large as possible; built in the same 27 km tunnel as the Large Electron-Positron (LEP) Collider [59]. This fixes the radius of curvature of the dipole magnets, which cover most of length of the tunnel, to 2.8 km [60]. The beam energy is then limited by the strength of the magnetic field. Dipole magnets which bend the beam account for most of the €3 billion cost of the accelerator.

The LHC collides protons and also lead ions (not considered in this thesis), both of which are hadrons. Few kinds of particles can be accelerated; in practice, they must be charged and stable. That leaves electrons, positron, protons antiprotons and ions.

Electrons and positrons are not used at the LHC. At LEP, they lost about 2% of their 200 GeV energy - by emitting syncrotron radiation - on each orbit of the accelerator. This limited the collision energy that could be achieved. Protons are about 2000 times heavier than electrons which drastically reduces this effect. For 7 TeV protons, around 7 keV is lost per orbit or about a billionth of the proton's energy. The main disadvantage is that proton collisions are much messier, since protons contain at least three point-like partons.

3.1.1 Superconducting Magnets

The strongest magnetic field that can be reached with traditional 'warm' magnets is about 2 T. Stronger fields can be achieved with superconductors. The LHC, like several colliders before it, uses niobium-titanium (NbTi) cables for the dipole bending magnets [61, 62], shown in Figure 3.2. These are superconducting below a temperature of 10 K (−263.2 °C). Cooling the cables further means that they can carry an even larger current.

The LHC has taken a step beyond previous superconducting colliders by using the extraordinary 'superfluid' state of helium to cool its magnets to 1.9 K. Almost 40,000 tonnes of metal, mostly iron, is kept cold. Cables designed to carry a current

(a) There are 1232 of these blue dipole magnets around the 27 km of the LHC. Each dipole is 14.3 m long and weighs about 35 tonnes.

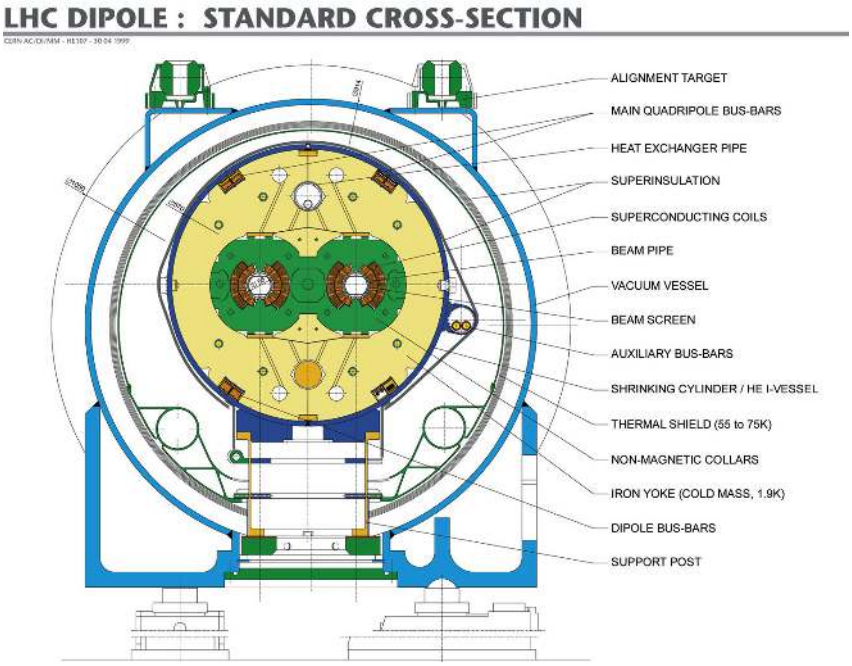

(b) One beam is carried in each beam pipe. The two sets of superconducting coils (orange) must therefore have opposite polarity to bend them in opposite directions. The collar (green) is designed to withstand the huge forces between the two. The iron yoke (beige) conserves the magnetic field. Outside this is an insulating vacuum and many layers of 'superinsulating' foil. There are also pipes to carry the helium coolant and bus-bars to carry the currents for quadrupole focussing magnets and in the event of a quench.

Figure 3.2: LHC dipole bending magnets.

of 11,700 A give a bending field strength of 8.3 T. Dipoles at the LHC's predecessor the Tevatron operated at 4.2 K and carried 4,350 A. This provided a bending field of 4.4 T [63].

Significantly for this thesis, the current and therefore beam energy in 2011 was limited to half that intended. This was the result poor interconnections in one of the systems used to protect the magnets. Imperfections with tiny resistances, or stray beam protons, are all that is needed to heat the cables too much, leading to the loss of superconductivity. This is known as a quench. Quenches are inevitable at the LHC, despite elaborate monitoring to avert them. If a quench is detected, the magnet current is switched very quickly into thick copper cables, placed alongside the superconductor, and out of the magnets. If this fails, the NbTi cables heat up enormously. Delicate parts of the magnets can melt away and huge forces can be put on the magnets as they expand [64].

3.2 Luminosity

In order to study very rare processes, a high rate of proton collisions is necessary. This depends on tight focussing of beams containing a large number of protons. These beam properties are usually summarized as the 'luminosity' $\mathscr{L}$ of the beams [65, 66]. The rate, and total number, of collisions expected are very important to know when analyzing data. They are calculated by measuring the luminosity, which is given by:

$$\mathscr{L} = \frac{n_b n_p^2 f}{A}, \tag{3.2}$$

where:

- n_b is the number of bunches per beam,
- n_p is the number of protons per bunch (bunch intensity),
- f is the frequency at which the beams circulate the ring in s^{-1} and

- A is the transverse cross sectional area of the overlap between the beams in fb or cm^2.

When trying to maximize the luminosity, various compromises must be made between the two approaches of focussing the beams more tightly (decreasing A) and increasing the number of protons per beam (increasing n_b or n_p). A number of effects can distort bunches and make them difficult to focus, although the bunch shape can be corrected to some extent with multipole magnets. This limits the luminosity that can be reached. The most important distorting effect is beam-beam interaction; the higher the luminosity, the stronger the repulsion between the protons of the two beams when they cross. The bunches can also be distorted by the walls of the beam pipe, imperfections in the bending field and by other bunches, especially if they are intense and closely spaced [67]. For each different arrangement of bunches, the focussing magnets are adjusted to focus the beams as tightly as possible at the interaction point, where they are brought into collision.

The luminosity at the Tevatron was limited by the difficulty of producing anti-protons, which is why the LHC collides protons with protons. The two beams must circulate in independent beam pipes under magnetic fields of opposite polarity. However, there was not enough room in the tunnel for two completely separate proton rings. This great engineering challenge resulted in the "two-in-one" design seen in Figure 3.2b.

The rate of a particular process in LHC collisions is given by $R_{\text{process}} = \sigma_{\text{process}}\mathscr{L}$, where σ is an area called the cross section. The total proton-proton cross section σ_{pp} can be thought of as the area that one proton presents to the other as a target. It should not be thought of as the geometric 'size' of a proton since they interact at a distance; it also varies as a function of the proton energy. The total proton-proton cross section has been measured at the LHC as about 100 millibarns $(\text{mb})^2$ [69, 70].

[2]The unit of area 'barn' has been used in nuclear and particle physics since it was dreamt up for communicating as secretly as possible by telephone in wartime [68]. One barn (10^{-24}cm^2) is roughly the cross section of a uranium nucleus.

The total number of proton collisions, Z bosons or other phenomena produced over an extended period of time is given by the 'integrated luminosity', shown in Figure 3.3, typically measured in fb^{-1}. The data used in this thesis corresponds to 2 fb^{-1} which corresponds to 200 million million proton collisions[3]. Rare processes have small cross sections. For example, the cross section to produce a Z boson is about 1.04 nb which corresponds to 2 million Z bosons in the 2 fb^{-1} data set. The cross section to produce an excited graviton with mass 1 TeV in the Bulk Randall-Sundrum model with $k/\overline{m}_{pl} = 0.1$ is 0.25 pb, as discussed in Section 2.3. If such a particle exists, 500 of them should have been produced.

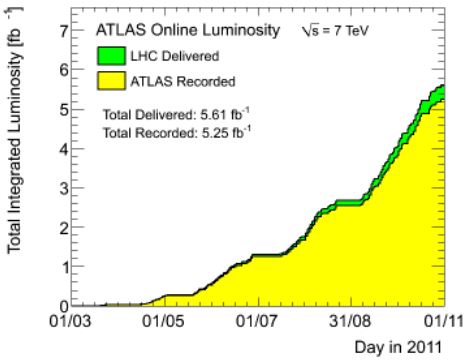

Figure 3.3: The integrated luminosity in 2011 as recorded by the ATLAS detector. ATLAS has almost always been fully functional when the LHC beam is delivered.

The LHC is designed to study processes as rare as the production of Z bosons and excited gravitons. The rate of proton collisions is therefore, by design, far too high for the results of all of them to be recorded in any detail. Indeed, in 2011, there was often an average of more than 20 collisions per bunch crossing. This increases the rate of interesting collisions, but these must typically must be distinguished from the results of many simultaneous low energy collisions. This effect is known as 'pile-up'.

[3] 2 fb^{-1} is multiplied by the total proton-proton cross section σ_{pp} of 100 mb (= 100 million million fb)

3.3 LHC Operation

On 19 September 2008, just over a week after the first beams were injected, a serious quench was caused by a resistance in one of the magnet connections of 220 nΩ, rather than the specified 0.6 nΩ which was small enough to avoid detection [60, 71]. The helium coolant was violently heated putting a force equivalent to 56 tonnes on the surrounding large dipole magnets and filling three miles of tunnel with helium gas. LHC operation was delayed by more than a year while 30 of the 1232 large bending magnets were replaced by spares and several improvements were made to the systems used to detect quenches and protect against them when they occur. In 2011, many of the faulty interconnections remained but the accelerator performed extremely well at half of the design energy.

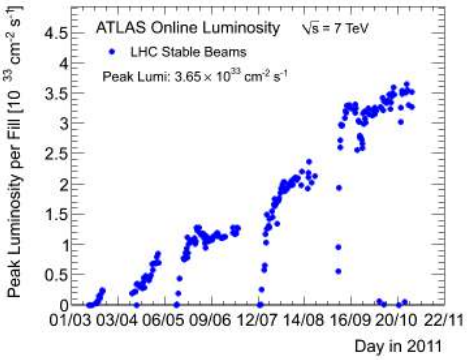

Figure 3.4: LHC luminosity in 2011. Design luminosity is 10^{34} cm^{-2} s^{-1}. The peak luminosity at the Tevatron was 0.35×10^{33} cm^{-2} s^{-1}.

Throughout 2011, the luminosity was gradually increased, with some collision-free periods for testing, as shown in Figure 3.4. The integrated luminosity of about 5 fb^{-1} reached by the end of the year exceeding official expectations from before the start of the year of 1 fb^{-1} and 2.5 ± 2 fb^{-1}.

3.3.1 Multiple Accelerators

As protons are accelerated in the LHC, their energy increases at each turn. The magnetic field must be increased in proportion to bend the beams by exactly the

right amount. It is essential that the beam does not touch the side of the pipe, which is 6.3 cm across and 27 km long. It is difficult to make magnets that provide a reliably uniform field over a very wide range of field strengths. The lowest energy of protons that can circulate in the LHC is 450 GeV and several accelerators are used to accelerate the protons to this energy.

A small quantity of hydrogen is fed into an instrument known as a duoplasmatron [72], shown in Figure 3.5a. Electrons are stripped from hydrogen atoms with a high voltage, leaving protons. These are accelerated in a linear accelerator, shown in Figure 3.5b, followed by a sequence of circular accelerators, listed in table 3.1, which includes the Proton Syncrotron (PS) which has been an important part of CERN since the lab's early days in 1959 [73]. The Super Proton Syncrotron (SPS) hosted the discovery of the W and Z bosons in 1983 [74, 75, 76]. A diagram of the accelerator complex at CERN can be seen in Figure 3.6. While injecting beams into the LHC it is important to account for the phase of the moon since it shifts the surrounding rock [77].

(a) The clear tubes hanging down carry hydrogen gas to the duoplasmatron. This strips off the electrons, leaving protons.

(b) Linac 2 is the first accelerator for protons for the LHC. The proton source is just out of the shot to the left. To the right, protons are sent on to the PSB.

Figure 3.5: Proton Source and Linac.

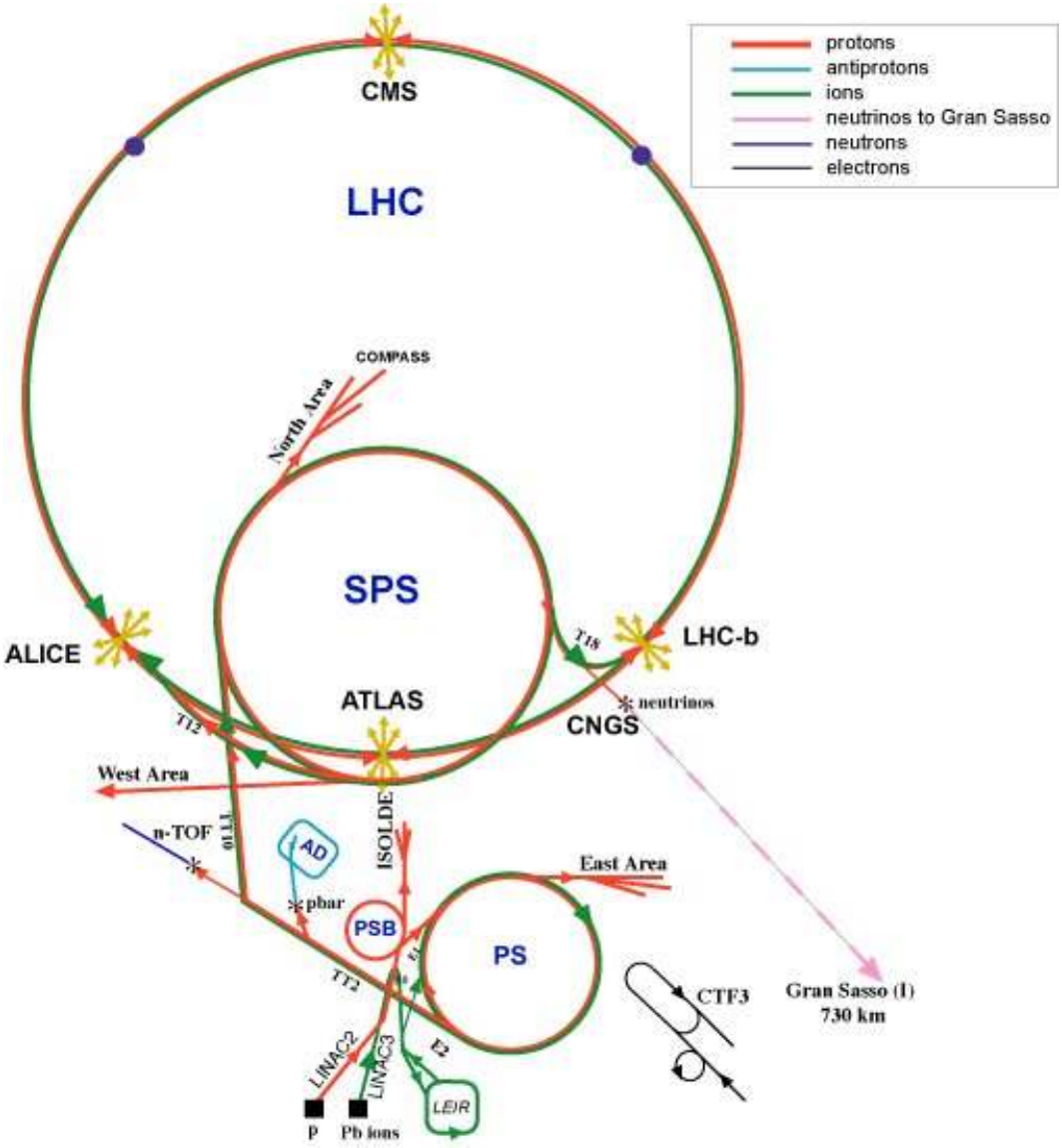

Figure 3.6: Protons for ATLAS are first accelerated by Linac 2 and then by a series of circular accelerators, listed in table 3.1 (the red path, not to scale). Protons are also used, often indirectly, for a wide range of other experiments at CERN. Three experiments are investigating antihydrogen at the Anti-proton Decelerator (AD); the ALPHA experiment has performed the first ever spectroscopic measurement [78]. The CLOUD experiment in the PS East Area is exposing gaps in current climate models by precisely reproducing early cloud formation [79].

Accelerator	Highest Energy Per Beam	Official Start Date
Linac 2	50 MeV	1978
Proton Synchrotron Booster (PSB)	1.4 GeV	1972
Proton Synchrotron (PS)	25 GeV	1959
Super Proton Synchrotron (SPS)	450 GeV	1976
Large Hadron Collider (LHC)	3.5 – 7 TeV	2009

Table 3.1: The LHC injection complex.

3.3.2 Bunches and Radio-Frequency Cavities

The LHC beams are organized into bunches separated by gaps which means that collisions occur on a regular schedule. This is a feature of the radio-frequency cavities used by all of the accelerators in the LHC injection complex. Strong electromagnetic fields oscillate back and forth in metal cavities. The bunches 'surf' on the electromagnetic waves, which come along once every 2.5 ns, timed so that they are accelerated in each cavity. In 2011, a 50 ns bunch spacing was used corresponding to a bunch every twentieth wave. Ultimately, 25 ns bunch spacing will be used.

The bunches in each LHC beam are arranged in up to 24 bunch trains. Each train corresponds to a single fill of the SPS. A gap between the trains is needed to allow time to switch on the abort magnet that diverts the beam between the accelerators. Each bunch train is made up of between two and four PS fills. The PS receives six bunches from the PSB and splits each into up to 12 smaller bunches. The bunches are originally produced by the Linac 2; 120 μs long with a total current up to 180 mA. The quality and stability of the beam from the Linac are important in limiting how tightly the beams can be focussed at the LHC experiments.

In 2011, using 50 ns bunch spacing, the LHC was completely filled with 1331 bunches per beam. Ultimately, with 25 ns bunch spacing, it should eventually carry 2808[4]. The number of bunches in the beam is an important factor in maximizing the rate of proton collisions.

[4]The Tevatron carried 108 bunches with 132 ns spacing

3.3.3 Beam Lifetime and Turnaround Time

The number of protons in the beam falls exponentially during a fill. The beam lifetime is limited by the intended proton-proton collisions as well as collisions with the residual gas in the beam pipe.

When a 3.5 TeV beam is circulating and the bending magnets are at 4.1 T, a huge electromagnetic energy of 300 MJ is stored in the magnets. It takes about 10 minutes to dissipate this energy safely after dumping the beam. Ideally, it should take about 15 minutes to completely fill the LHC [56], after which it takes at least 10 minutes to increase the bending field while accelerating the beams.

The theoretical minimum turnaround time from beam dump to the start of a new run is around an hour, after including another 10 minutes to make checks. However the LHC design report predicted, from long experience with many proton colliders, that even after years of operation the average could be more than six times this number [80]. Several attempts may be necessary at each injection stage and recovering from a quench can take hours. The fastest turnaround time recorded in 2011 was 2 hours 7 minutes. The mean of 11.1 hours while simultaneously increasing the machine performance represents an impressive achievement and has contributed significantly to the high integrated luminosity delivered in the year. Run lengths and turnaround times in a successful week can be seen in Figure 3.7.

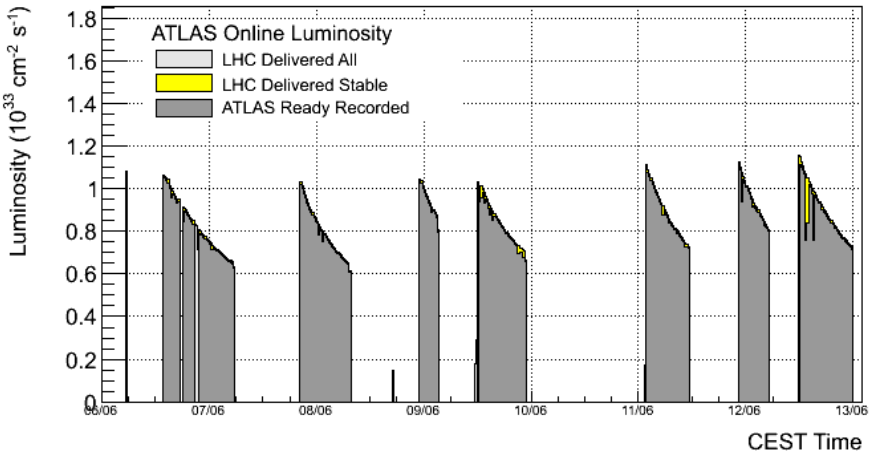

Figure 3.7: Luminosity during the week beginning Monday 6 June, 2011. The LHC was filled 13 times (fills 1853 – 1865) of which seven resulted in a significant number of collisions. Each fill corresponds to a dot in Figure 3.4. The turnaround time between these fills ranges from about six hours to more than 24. An integrated luminosity of 0.212 fb^{-1} was delivered to ATLAS, making it the week that contributed the most data to this thesis. (CEST = Central European Summer Time)

Chapter 4

The ATLAS Detector

ATLAS is an all-purpose particle detector designed to measure as many physical parameters of particles produced in LHC collisions as possible [81]. Its design principles follow those of many detectors at previous high energy colliders. It is roughly cylindrical in shape and made up of three main layers: the inner detector or tracker, surrounded by the calorimeter, followed by the muon system. Each of these sub-detectors, shown together in Figure 4.1, is in turn made of many layers and multiple electronic channels which are 'read out' by a triggering and data acquisition system. The working principles of the sub-detectors and sub-systems are described below and the details of the design which are specific to LHC experiments and to ATLAS.

ATLAS measures the energy and momentum of many physics objects such as electrons, muons and jets, more precisely than previously possible. ATLAS is the largest detector of its kind - 44 m long and 25 m in diameter - and weighs approximately 7,000 tons. It is finely segmented with 160 million read-out channels and over 300,000 km of cables. Around 3,000 scientists and engineers are involved in operating the experiment and analyzing the data it generates.

ATLAS uses a right-handed coordinate system with its origin at the center of the detector. The positive x-axis points towards the center of the LHC ring. The positive y-axis points upwards. The positive z-axis points in the direction of the beam, which travels anti-clockwise as seen from above. The azimuthal angle ϕ is measured from the positive x-axis. Instead of the polar angle θ, measured from the positive z-axis,

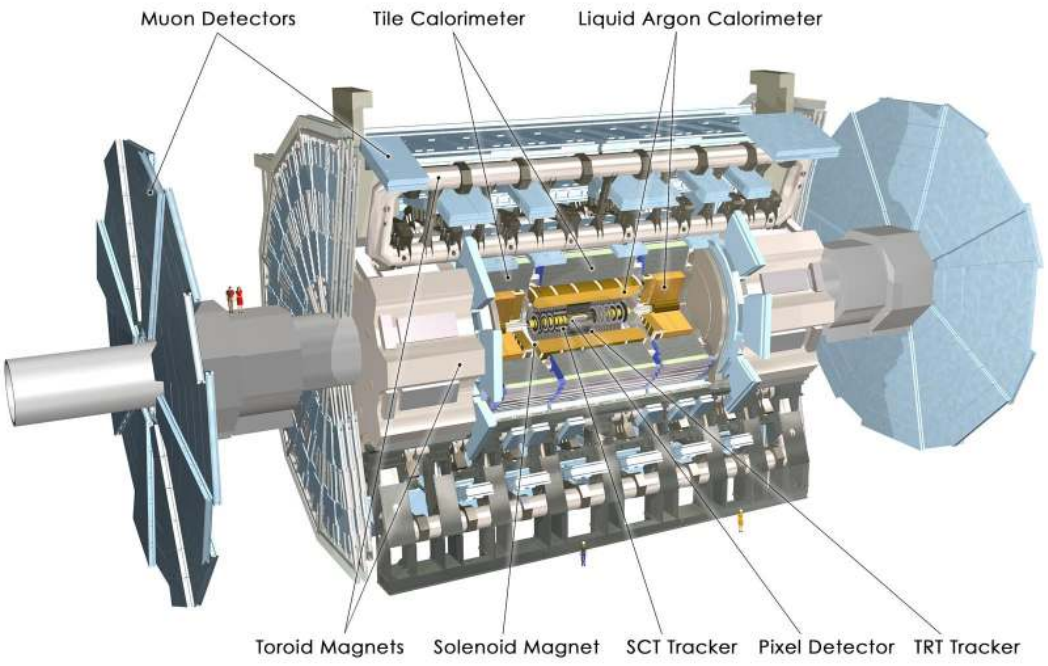

Figure 4.1: The ATLAS detector is made of many sub-detectors in order to measure as many as possible physical parameters of particles produced in LHC collisions.

it is more convenient to use the pseudorapidity, defined as $\eta = -\ln(\tan(\theta/2))$. The pseudorapidity is an approximation of the rapidity y and the two are equal in the limit of massless particles. Rapidity is defined as $y = 1/2 \times \ln[(E + p_z)/(E - p_z)]$, where E is the energy and p_z is the component of the momentum along the beam direction. The rapidity size of objects such as jets tends to be independent of rapidity since Δy of two particles is independent of Lorentz boosts along the beam axis. The area around $\eta = 0$, perpendicular to the beam axis, is referred to as the 'central region'. The area around $\eta = \pm\infty$, parallel to the positive/negative beam axis, is referred to as the 'forward region'. The radial distance from the beam axis is often referred to as r.

4.1 Principles of Particle Detectors

4.1.1 Tracking Detectors

Tracking detectors make precise measurements of the trajectories of charged particles. Software is used to reconstruct a particle's track from hits recorded in successive layers of the detector. Tracker components record particle hits from which a track is reconstructed. In a magnetic field, the trajectory is curved allowing a measurement of the particle momentum and charge.

At high energy colliders, tracking detectors are as light as possible in order to reduce particle scattering and energy losses before they reach the calorimeter. The components closest to the beam pipe are especially important for precisely locating the 'primary vertex' points of proton collisions and 'secondary vertex' points of heavy quark decays.

Two basic tracking technologies are used: semiconductors and gaseous detectors. The working principles of the two are similar. When a charged particle passes through the volume, it produces electron-ion pairs (in a gaseous detector) or electron-hole pairs (in a semiconductor detector). These are pulled apart by an applied voltage, creating a small current which must be amplified.

Semiconductor detectors are typically made of silicon wafers. They can be read out quickly relative to gaseous detectors and can be very finely segmented with relative ease, by photolithography. They have a comparatively high radiation tolerance but are more expensive than other tracker technology. Together, these qualities make semiconductor detectors ideal for the smaller innermost parts of a tracker.

Gaseous detectors were the first particle detectors, used since H. Geiger's single-wire counter in 1908. Since then a wide variety have been developed, typically using a large number of wires. Gas has the advantage of being light, although the detector's support structures may not be, and can be easily replaced before it suffers radiation damage. Gaseous detectors also take advantage of internal amplification, or gas gain, of the signal. If the applied voltage is high enough, electrons released in the ionization process gain enough energy to cause further ionization in

the surrounding gas. This can greatly reduce the need for electronic amplifiers and associated cooling.

Two modes of operation are used for gaseous detectors at ATLAS: proportional mode and avalanche mode. In avalanche mode, a very high voltage quickly ionizes the entire volume of gas fully each time a charged particle passes through the detector. This is especially useful for triggering. In proportional mode, a relatively low voltage produces a signal 10^3 – 10^4 times size of the original ionization. The original level of ionization can be used for particle identification. The 'drift time' in proportional mode tends to be long. However, precisely measuring it can significantly enhance the tracker's position resolution by allowing the distance between the track and the wire to be measured.

4.1.2 Calorimeters

Calorimeters measure the energy of particles by absorbing them completely. They are dense, in order that a shower of secondary particles develops quickly. The total energy loss is calculated from the interactions of these secondaries in an 'active medium'. Calorimeters are one of the only ways to detect neutral particles, which make up an important fraction of jet energy.

Understanding the ways in which particles lose energy in matter is essential in designing and using a calorimeter [82]. The most important processes are: bremsstrahlung, ionization, pair-production and nuclear interaction. The behavior of electromagnetically interacting particles (e.g. electrons and photons) is significantly different to that of hadrons.

High energy electrons (and positrons) lose energy exponentially by radiating photons (bremsstrahlung). The radiation length X_0 depends on $1/Z^2$ of the material, where Z is the atomic number. At lower energies, ionization dominates. Photons with energy above 1 MeV produce e^+e^- pairs after $\frac{9}{7}X_0$; below this they can only be absorbed by atomic electrons. When electrons or photons enter a calorimeter, a chain-reaction of bremsstrahlung and pair-production creates a characteristic electromagnetic shower, usually contained within $25X_0$. Electron showers generally

initiate sooner than photon showers.

High energy hadrons lose most of their energy from collisions with nuclei. These produce secondary hadrons with a wide variety of lifetimes and decay products. Hadronic showers are much more diverse than electromagnetic showers. In fact, electromagnetic sub-showers often account for a large fraction of the highest energy showers. Ionization by charged hadrons is significant but bremsstrahlung is not. Up to 40% of the energy in jets of hadrons is invisible since it is deposited in nuclear binding energy and recoil. The energy of muons and neutrinos that escape the calorimeter is also not included.

The mean free path of protons, before undergoing an inelastic nuclear interaction, is known as the interaction length λ, which increases with the mass number A of the material. This is typically longer than a radiation length; hadrons take longer to stop than electrons and photons.

Muons, because of their high mass, rarely initiate electromagnetic showers via bremsstrahlung. They lose a small amount of energy by ionization as they pass through calorimeter material. A muon system is built around the calorimeters to measure them precisely.

Since neutrinos interact so rarely with matter, there is no chance of being able to measure them. Instead they are identified by looking for missing transverse momentum. To measure missing transverse momentum accurately, it is important for the calorimeter to surround the interaction point as completely as possible.

4.2 Inner Detector

The ATLAS inner detector, shown in Figure 4.2, is made up of three subsystems: the three-layer silicon pixel tracker from 4 to 20 cm away from the beam axis, at $\eta = 0$; the four-layer silicon microstrip tracker (SCT) from 30 to 52 cm; and the three-layer transition radiation tracker (TRT) from 56 to 108 cm. It covers the central region $|\eta| < 2.5$. A solenoidal field, parallel to the beam axis, bends the trajectory of outgoing particles.

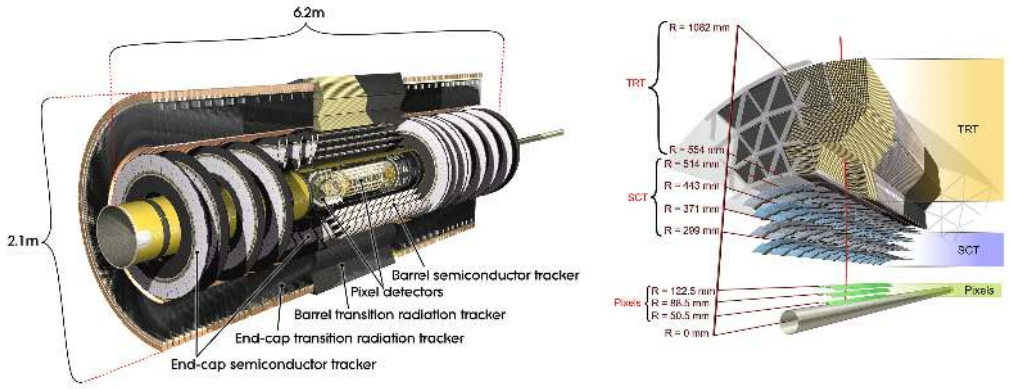

(a) Cut-away diagram of inner detector showing its sub-detectors.

(b) Wedge of the ATLAS inner detector. A high energy particle track is shown.

Figure 4.2: Two diagrams of the inner detector.

Tracks are used in several ways in this thesis. They are an important part of the identification and measurement of electrons and muons. They are also used to associate jets to primary vertices in what is known as the jet vertex fraction (JVF). Furthermore, 'track jets', reconstructed using only track information are used as an independent cross check of the energy of calorimeter-based jets.

4.2.1 Silicon Pixel Detector

The pixel detector is made of 1.8 m^2 of silicon, arranged in three layers in the barrel and three endcap disks on each side. There are 80 million channels with a minimum size 50 μm $\times$ 400 μm[1]. This size is chosen as a compromise between limiting the number of read-out channels while maximizing the position resolution and minimizing the occupancy - the fraction of channels read out in each event.

A particle crossing a layer of the pixel detector will release a few tens of thousands of electron-hole pairs. If this signal exceeds a tunable threshold, a hit is read out.

[1]Charge coupled devices (CCDs) in digital cameras typically have a few million pixels on a few cm^2 of silicon. However, their response is up to a hundred thousand times slower: several ms instead of a few hundred ns.

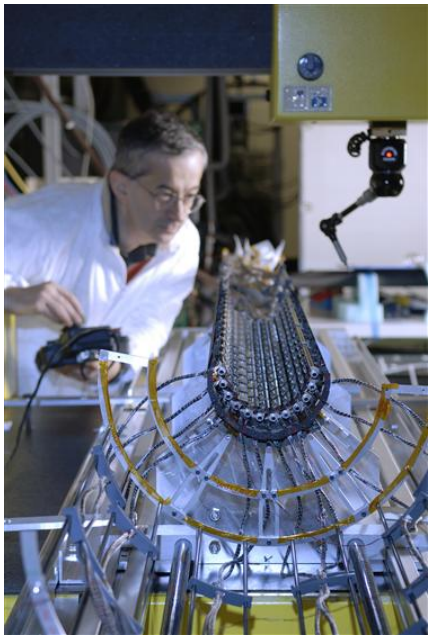

Figure 4.3: Testing the first layer of pixels, the 'b-layer'. Mounts for the second and third pixel layers can be seen.

During 2011 running, typically only a few pixels per 10,000 reached this threshold. The hit efficiency is over 99%. The signal in each pixel is compared to the threshold every 25 ns, and the length of time-over-threshold is recorded. This approach reduces noise, which typically has low time-over-threshold (about 125 ns), whereas hits from minimally ionizing charged particles are expected to have a time-over-threshold of about 750 ns.

The first layer of pixels, shown in Figure 4.3, is built right onto the beam pipe[2], at about $r = 5$ cm. It is known as the b-layer because of its crucial role in identifying secondary vertices of b-jets.

The pixel detector has been built to withstand the unprecedented flux of high energy particles at the LHC. At design luminosity, 40 million charged particles with momenta above 10 MeV will cross each cm^2 of b-layer every second. This

[2]The beam pipe must be strong enough to withstand the ultra-high vacuum of the accelerator without support and yet be as transparent as possible to particles. Within ATLAS, the beam pipe is made of beryllium.

corresponds to a radiation dose of about 160 kGy/year where 1 – 10 Gy is lethal for humans. Oxygenated silicon cooled to around $-10°$C is used to improve the pixel detector's radiation tolerance, however, it is not expected to survive more than five years of design luminosity and will then be replaced.

4.2.2 Silicon Microstrip Detector (SCT)

The SCT is made of 61.1 m^2 of silicon arranged in four double-sided layers in the barrel and nine endcap disks on each side. It has 6.2 million channels. The silicon microstrips are similar to the pixels except that they are long in the z direction: 80 μm $\times$ 13 cm. Only hits above a tunable threshold are read out but no time-over-threshold information is stored.

The momentum resolution of the inner detector is largely governed by the high ϕ resolution of the SCT. The resolution in the poorly measured z direction is greatly improved by gluing a pair of silicon wafers back-to-back with an angle of 40 mrad between strips on the two wafers. However, this leads to 'ghost' ambiguities at high occupancy. The hit occupancy at design luminosity is about 1%.

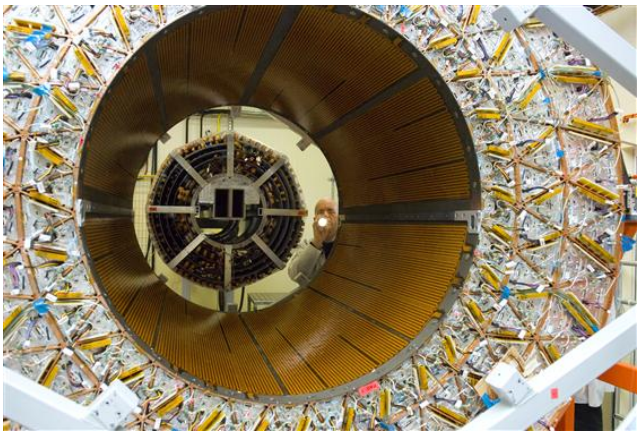

Figure 4.4: The SCT barrel being inserted into the TRT.

4.2.3 Transition Radiation Tracker (TRT)

The TRT is a gaseous detector in proportional mode with almost 300,000 single-wire straws. It covers the region $|\eta| < 2$. The TRT significantly contributes to

the momentum resolution of the inner detector and is also used for electron/pion discrimination. It surrounds the SCT as shown in Figure 4.4.

The TRT straws are 4 mm in diameter and made of carbon-fiber reinforced Kapton®. Those located in the barrel are completely surrounded by mats of fine polyethylene-clad polypropylene radiator fibers. In the endcaps, radiator foils are used. The active gas in the straws is xenon, which is mixed with a little CO_2 and O_2. The region between the straws is continuously flushed with CO_2 to avoid energy loss in escaped xenon outside the straws. A voltage of 1530 V provides a gas gain of 2.5×10^4. An extraordinary wire is needed to ensure that the gas gain remains uniform throughout the detector for many years. It is made of gold-plated tungsten and has been extensively inspected for defects.

Transition radiation is emitted by relativistic charged particles as they pass between media of different dielectric permittivity. In the TRT, this effect is mostly used to discriminate between electrons and pions with energies below 200 GeV. Electrons have lower mass and so emit much more radiation - mostly at a small angle to the electron - which leads to greater ionization. Two tunable thresholds are used in the TRT. Electrons give far more high threshold hits than pions. For an electron efficiency of 90%, pion rejection is typically as much as a factor of 5.

4.2.4 Performance

A particle with charge q and a transverse momentum p_T perpendicular to a constant magnetic field B will deflect by an angle $\alpha = qBL/p_T$, after having travelled a distance L. In a vacuum, the fractional momentum resolution is proportional to the measured precision of the angle $\delta\alpha$ and also to the momentum. However, if the particle crosses material it is deflected a little, multiple times, degrading the measurement of the angle; this 'multiple scattering' is parametrized by c_{MS}:

$$\frac{\delta p_T}{p_T} = \frac{p_T \cdot \delta\alpha}{qBL} \oplus \frac{c_{MS}}{qBL}. \tag{4.1}$$

The transverse momentum resolution of the ATLAS inner detector is: $\sigma_{p_T}/p_T = (0.05\% \times p_T) \oplus 1\%$. This significantly improves on that of the CDF detector, which

was upgraded for Run II of the Tevatron in 2001. The first term of the momentum resolution of the inner detector at CDF of was: $\sigma_{p_T}/p_T^2 = 0.09\%$ [83].

The track reconstruction efficiency ranges from 78% for tracks with $p_T = 0.5$ GeV to more than 85% above 10 GeV. The resolution on r of the primary vertex is 10 μm for high momentum particles as compared to 15 μm for CDF. The position resolution and η coverage of each of the ATLAS tracking sub-detectors is given in Table 4.1.

Subdetector	Coverage	Spacial resolution [μm]	Hits per track
Pixel barrel	$\|\eta\| < 2.5$	10 (r-ϕ), 115 (z)	3
Pixel endcaps	$2.0 < \|\eta\| < 2.5$	10 (r-ϕ), 115 (r)	3
SCT barrel	$\|\eta\| < 1.5$	17 (r-ϕ), 580 (z)	8
SCT endcaps	$1.3 < \|\eta\| < 2.5$	17 (r-ϕ), 580 (r)	8
TRT barrel	$\|\eta\| < 1.0$	130 (r-ϕ)	35
TRT endcaps	$0.8 < \|\eta\| < 2.0$	130 (r-ϕ)	35

Table 4.1: Summary of coverage and resolution of sub-detectors in the ATLAS inner detector. Spatial resolution refers to a single 'space point', which corresponds to one pixel hit or one double layer SCT hit.

4.3 Calorimeters

At ATLAS, the solenoid magnet is inside the calorimeter. Fewer restrictions were placed on the design of the calorimeter but particles must cross more material before they reach it. The probability of initiating an electromagnetic shower in the inner detector is given by the number of radiation lengths, shown in in Figure 4.5. The active parts represent a small amount of material but, including all of the support structures, and the solenoid and calorimeter cryostat not shown in the diagram, particles pass through about 1 – 4 radiation lengths of material before reaching the calorimeter. Corrections are applied to electrons to account for the associated energy loss, and tracking algorithms which account for bremsstrahlung are being developed to further increase the efficiency and to improve the energy resolution

at low p_T. 'Conversion' of photons into an e^+e^- pair in the inner detector are an essential part of photon reconstruction.

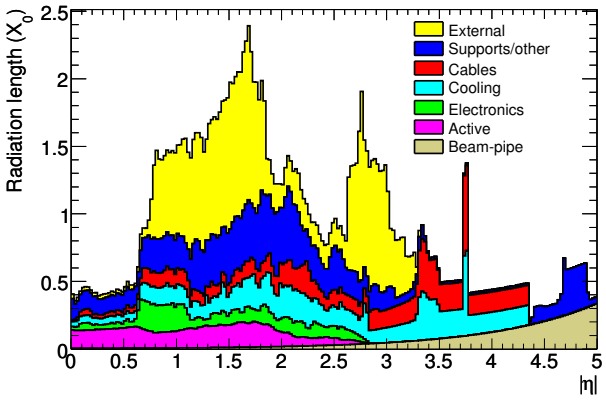

Figure 4.5: Radiation depth of the inner detector.

ATLAS uses sampling calorimeters which alternate thin layers of dense metal and active medium. Particles deposit a fraction of their energy in the active medium. The choice of active medium is a compromise between energy and position resolution requirements, radiation tolerance, cost, compactness and the material's behavior in the presence of magnetic field. Two types of medium can be used: ionization calorimeters, which can be more finely segmented, giving better position resolution and particle discrimination; and scintillators which typically give a better energy resolution, limited by photon statistics [84]. ATLAS uses both types of active media: liquid argon and plastic scintillating tiles. The design issues and read-out electronics of the liquid argon and the Tile calorimeter are described in detail in the sections below. Liquid argon is a monoatomic gas and is therefore intrinsically radiation resistant. It is also dense relative to other active media which helps to stop particles. The drift time in liquid argon is relatively slow which can lead to potential occupancy issues unless complex read-out electronics are used.

Since electrons and photons stop considerably sooner than hadrons in the ATLAS calorimeter, the first part of the calorimeter is designed with them in mind and is referred to as the electromagnetic (EM) calorimeter. Behind it is a more coarsely segmented hadronic calorimeter. In the central region, the Tile calorimeter serves as

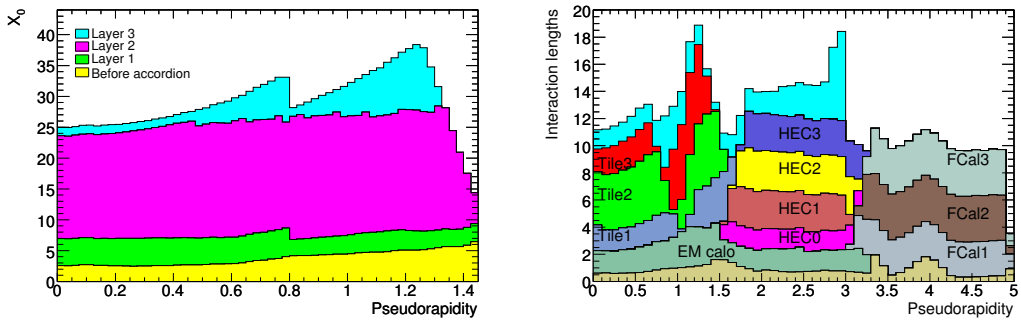

(a) Radiation depths of the barrel section of the LAr calorimeter. Most of the energy is deposited in the second (middle) layer.

(b) Interaction depths of the entire ATLAS calorimeter.

Figure 4.6: Radiation and interaction depths of the ATLAS calorimeter.

the hadronic part. The ATLAS EM calorimeter is about 20 – 40 radiation lengths thick as shown in Figure 4.6a and the entire calorimeter is at least 10 interaction lengths thick as shown in Figure 4.6b. This completely absorbs electrons and photons with energies up to about 1 TeV. The EM calorimeter also absorbs up to 70% of the energy of a typical hadronic shower. The entire ATLAS calorimeter, consisting of electromagnetic and hadronic LAr calorimeters and the hadronic Tile calorimeter, is shown in Figure 4.7.

4.3.1 Liquid Argon (LAr) Calorimeter

The EM barrel and endcap calorimeters cover the region $|\eta| < 1.475$ and $1.375 < |\eta| < 3.2$. They use a novel 'accordion' design, made of liquid argon and lead layers a few mm thick, as shown in Figure 4.8a. It ensures that particles cross the liquid argon several times while allowing a self-supporting structure covering a full 360° to be constructed without gaps. Electronic channels are etched on copper electrodes between the lead layers. The hadronic endcaps (HEC) cover the range $1.5 < |\eta| < 3.2$ and use flat liquid argon and copper plates, rather than an accordion structure. The forward calorimeter (FCal) covers the region $3.1 < |\eta| < 4.9$. It is built in three modules in each endcap, each 45 cm thick. The first module uses

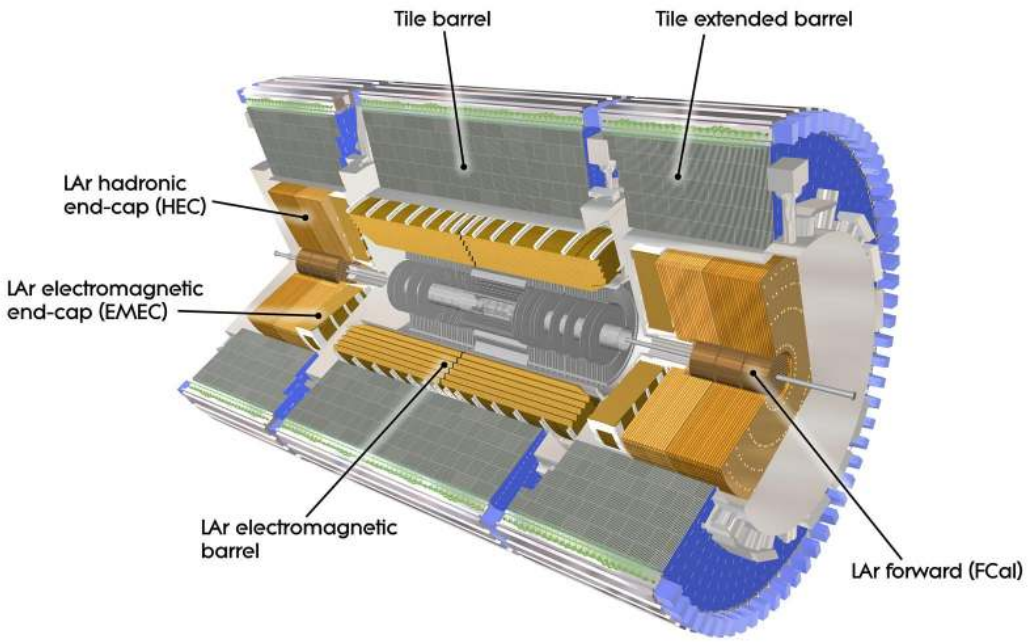

Figure 4.7: Diagram of the calorimeters. Two active media are used, liquid argon and tiles of plastic scintillator. The part of the calorimeter closest to the interaction point is referred to as the electromagnetic calorimeter.

copper as an absorber, the others use tungsten because, despite being difficult to work with, it is 1.7 times denser than lead. Rods of copper/tungsten absorber are inserted into holes drilled in stacks of copper/tungsten plates. The rods are also used as electrodes with a few rods to each read-out channel. A 0.3 mm or 0.5 mm gap between the rods and the plates is filled with liquid argon.

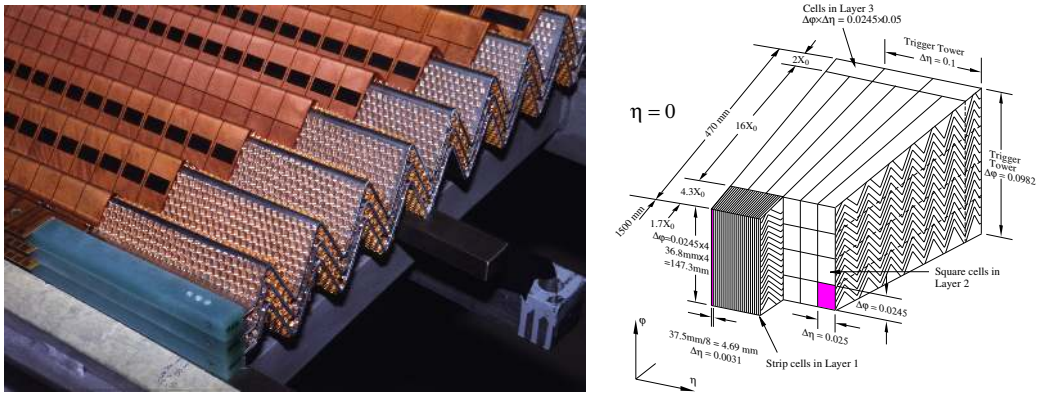

(a) LAr calorimeter accordion structure, Particles enter from the bottom left of the picture. The copper electrodes are spaced from the lead by honeycomb.

(b) Segmentation of the barrel section of the LAr calorimeter. The front layer is particularly finely segmented in η.

Figure 4.8: Design of the LAr calorimeter.

Electromagnetic (EM) Calorimeter An important task of an EM calorimeter is to identify electrons and photons from a sea of hadrons and measure their energy as precisely as possible. The EM calorimeter is divided into three layers. An extra active layer of liquid argon, the presampler, is placed before any lead in the central region. These layers are divided into cells of a fixed size in η and in ϕ, shown in Table 4.2 and in Figure 4.8b. In the central region, the front layer is segmented particularly finely in η. This is important for discriminating between neutral pion decays ($\pi^0 \rightarrow \gamma\gamma$) and electrons as well as obtaining a good estimate of the 'pointing angle' of the shower. Most energy is deposited in the middle layer. The back layer fully absorbs the highest energy electrons and photons.

	$\|\eta\|$ range	Layer 0	Layer 1	Layer 2	Layer 3
EM barrel	0 – 1.35	0.025×0.1	$0.025/8 \times 0.1$	0.025×0.025	0.05×0.025
	1.35 – 1.4	0.025×0.1	$0.025/8 \times 0.1$	0.025×0.025	–
	1.4 – 1.475	0.025×0.1	$0.025/8 \times 0.1$	0.075×0.025	–
EM endcaps	1.375 – 1.425	–	0.05×0.1	0.05×0.025	–
	1.425 – 1.5	–	0.025×0.1	0.025×0.025	–
	1.5 – 1.8	0.025×0.1	$0.025/8 \times 0.1$	0.025×0.025	0.05×0.025
	1.8 – 2.0	–	$0.025/6 \times 0.1$	0.025×0.025	0.05×0.025
	2.0 – 2.5	–	$0.025/4 \times 0.1$	0.025×0.025	0.05×0.025
	2.5 – 3.2	–	0.1×0.1	0.1×0.1	–
Tile	0 – 1.7	–	0.1×0.1	0.1×0.1	0.1×0.1
Hadronic endcaps	1.5 – 2.5	–	0.1×0.1	0.1×0.1	0.1×0.1
	2.5 – 3.2	–	0.2×0.1	0.2×0.1	0.2×0.1

Table 4.2: Granularity of the ATLAS calorimeter ($\Delta\eta \times \Delta\phi$). The granularity of the FCal ($3.1 < |\eta| < 4.9$) varies as a function of η because the cells are divided in x-y; it is generally a little coarser than the hadronic endcaps.

Energy Measurement Liquid argon is ionized by charged particles in an EM shower. Electrons and ions drift apart under a high voltage. This drift current is proportional to the number of charged particles in the shower which increases with the particle energy.

The drift current rises quickly and decreases constantly over a drift time of about 400 ns, many times that of the LHC bunch spacing. Figure 4.9 shows the triangular shape of the ionization current with time. This feature means that the peak current is strongly affected by prior ionization, which is unacceptable given the high pile-up conditions at the LHC. At design luminosity, a pion is expected to hit the larger cells almost every 400 ns, although it will generally have much less energy than particles of interest.

The solution chosen for ATLAS is a pulse shaping circuit which returns a fast peak corresponding to the *change* in ionization current. This peak is followed by a small negative current for the rest of the drift time since the integral of the pulse shape over time must be zero. A typical pulse shape is overlaid in Figure 4.9. This shaping reduces the effect of recent interactions on the height of the peak, leading

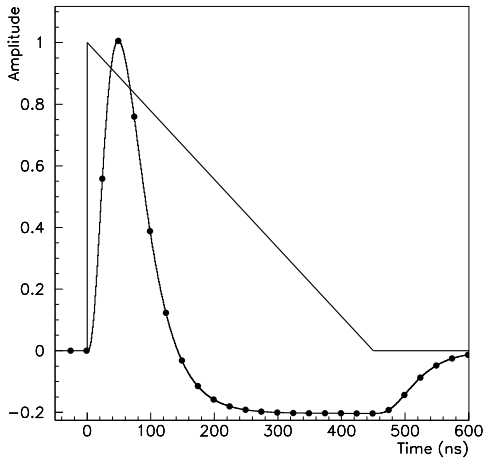

Figure 4.9: Pulse shape in the LAr calorimeter. A shaped signal pulse is produced from a triangular drift current by a passive circuit. The signal pulse is sampled every 25 ns. Usually the first five samples (from zero) are read out and used to calculate the energy. However, up to 32 samples can be read out in special runs for testing purposes.

to a smaller contribution to the energy uncertainty, referred to as 'pile-up noise'. A gain G of 1, 10 or 100 is used to amplify low energy signals before they are digitized. The pulse is sampled every 25 ns and five samples are read out for each cell.

Shaping, sampling and digitizing for 128 cells is performed by each front-end board on the detector. The digitized samples are first processed by DSP chips in a cavern about 100 m away from the detector. The five digitized samples s_i have the zero-signal 'pedestal' value p_{G} of the channel subtracted from them and are then multiplied by optimal filtering coefficients (OFCs) $a_{i,\mathrm{G}}$ and $b_{i,\mathrm{G}}$ to estimate the peak of the waveform and the time of the peak [85]:

$$E = \sum_{\text{samples } i} a_{i,\mathrm{G}}(s_i - p_{\mathrm{G}}) \qquad \text{and} \qquad Et = \sum_{\text{samples } i} b_{i,\mathrm{G}}(s_i - p_{\mathrm{G}}). \tag{4.2}$$

Scale factors are then applied to extract an energy measurement from the ADC counts for each gain.

Calibration Every step of this energy calculation has been validated and calibrated in test beam conditions [86], and, where possible 'in situ'. Multiple corrections are applied to get the best possible estimate of the energy. Two examples of such corrections included in the energy calculation, variations in drift time and timing alignment, are shown in Figure 4.10. The drift time across the liquid argon varies as a function of η, due to the change in high voltage applied and the thickness of the liquid argon [87]. Corrections have also been loaded onto the front-end boards to precisely align the timing of the sampling process.

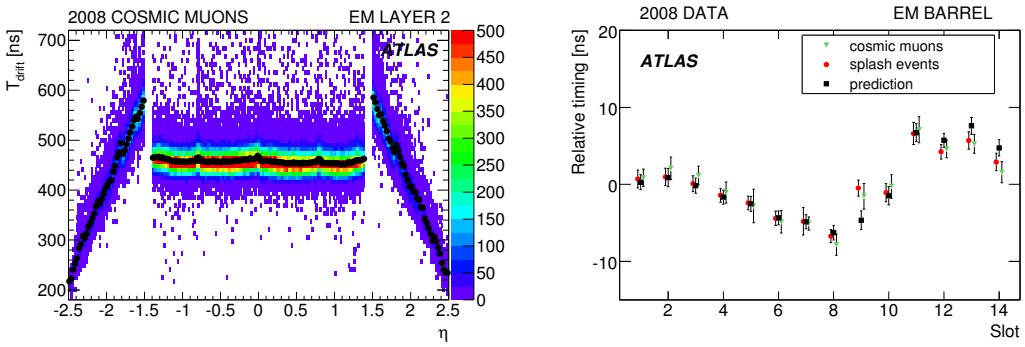

(a) The drift time as a function of η.

(b) Timing alignment of the barrel section. Front-end boards are numbered with a 'slot' which roughly identifies the layer and η position of the channels.

Figure 4.10: Examples of alignment and calibration applied to the signal in the LAr calorimeter before calculating the energy of the signal. Both sets of calibrations were derived before the first LHC collisions in 2010.

The amplitude of the ionization current corresponds to the energy deposited in the cell. It is best measured if the waveform is sampled precisely at peak of the pulse. In order to do this, each front-end board is connected to the LHC bunch crossing clock. Time delays of up to 15 ns are applied to compensate for the expected time of flight of particles from the interaction point as well as the differences in lengths of cables used for the timing signal. Precise estimation and validation of these delays were made after the entire calorimeter was in place, but before the very first LHC

collisions [88].

Three methods of estimating the time delays were used. The first prediction was derived from the measured lengths, impedances and temperatures of the cables used to relay the timing signals.

Second, delays were estimated from two sets of non-collision data, cosmic ray data and 'splash' events. During LHC commission periods, the full beam is occasionally guided to strike one of the beam collimators just upstream of the detector. Large showers of particles, mostly muons, travel through the detector roughly parallel to the beam line. These so-called splash events deposit significant energy in each cell, which is ideal for timing alignment, since the timing resolution is much crisper at high energy.

Thirdly, timing alignment was measured using almost 700,000 cosmic muon events recorded by ATLAS in 2008. Energy deposits that could be distinguished from noise were compared to times measured in the Tile calorimeter and the TRT. Good agreement was observed between all three methods across the entire calorimeter.

At the start of LHC collisions, the timing resolution of the LAr calorimeter was measured to be about 1 ns, thought to be dominated by residual timing misalignment. A study using 2011 data has since shown that - after applying timing corrections as a function of cell energy, the channel within each front-end board and primary vertex position - a timing resolution of about 0.3 ns can be achieved.

4.3.2 Tile Calorimeter

The Tile calorimeter is designed to fully stop hadrons in the central region and measure their energy. It is divided into a long barrel section covering $|\eta| < 1.0$ and extended barrels on each side covering $0.8 < |\eta| < 1.7$. It is made of 3 mm doped-polystyrene scintillating tiles between $4 - 5$ mm layers of steel absorber. Scintillating tiles were found to be more cost effective than liquid argon for this part of the calorimeter but they are susceptible to radiation damage. The signal they produce is expected to decrease by several percent over the lifetime of the

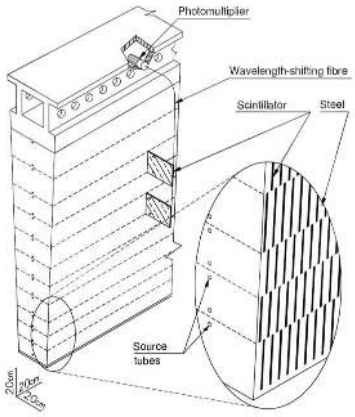

(a) Diagram of a Tile Calorimeter module. Particles enter from below.

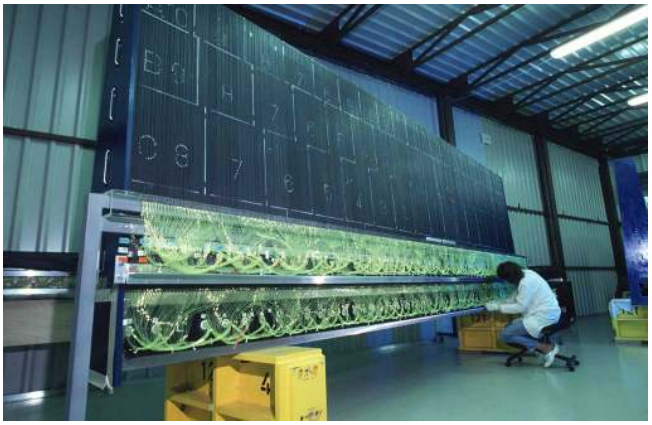

(b) A complete barrel module. Particles enter from above. Green light is coming from the wavelength-shifting read-out fibers which run vertically through the module.

Figure 4.11: A Tile calorimeter module.

experiment. Surprisingly, the scintillating tiles are oriented in the r–ϕ plane, parallel to the direction of the incoming particles at low η. This is not a problem since at the end of a hadronic shower, low energy charged particles are nearly isotropic. Indeed the orientation has the advantage that the read-out fibers attached to the long edges of the tiles can run directly to the outside of the calorimeter, which practically eliminates the need for gaps, as shown in Figure 4.11. These wavelength-shifting fibers produce low energy photons and increase the efficiency of the photomultiplier tubes which are arranged around the outside of the calorimeter.

The Tile calorimeter is supported on a steel yoke at $r = 4.25$ m, which also provides a return for the solenoid field. This results in a negligible magnetic field in the barrel section of the LAr calorimeter, which would otherwise distort particle shower shapes.

4.4 Muon System

The muon system is designed to make precise measurements of the momentum and charge of muons by tracking their trajectories, as they curve in the magnetic field.

It follows many of the principles of a tracking detector as described in section 4.1.1, but on a much larger scale than the inner detector. In contrast to the inner detector, the field is toroidal, bending muons in the r-z plane. This allows a more precise measurement of forward muons.

ATLAS relies on excellent stand-alone performance of the muon system, although the inner detector improves the measurement of low momentum muons [89]. A moderate magnetic field (0.5 T on average) is achieved throughout a huge volume (26 m $\times$ 20 m diameter) by 'air-core' magnets, reducing the amount of material and, as a result, the multiple scattering. Momentum resolution is limited instead by the position resolution of muon hits. The deviation from a straight line, or sagitta, of muons with $p_T = 1$ TeV is 0.5 mm over at least 5 m in the muon system. The design goal of the muon system is to measure such muons to within 10% accuracy. To achieve this, the sagitta resolution must be 0.05 mm.

Gaseous detectors are the only practical technologies able to achieve such high position resolution over such a wide area. Two types of proportional-mode detectors are used in the central and forward regions. The position resolution of these detectors depends on a long drift time, which is generally much longer than the LHC bunch spacing. However, a fast measurement is also crucial for triggering purposes and to associate muon track with the correct bunch crossing. Therefore, two types of avalanche-mode triggering detectors are used in parallel. The detectors which make up the muon system are described in the sections to come and shown in Figure 4.12 [90].

4.4.1 Precision Muon System

Monitored drift tubes (MDTs) are used throughout the muon system, in the barrel and endcaps ($|\eta| < 2.7$). The drift tubes are wide compared to the segmentation of other ATLAS tracking technology (3 cm diameter). They are arranged in chambers which are 1 – 6 m long and 1 – 2 m wide, depending on their position in the detector. Each chamber has one or two sets of three or four layers of tubes, as shown in Figure 4.13a; 'in-plane alignment' lasers - which measure the expansion of

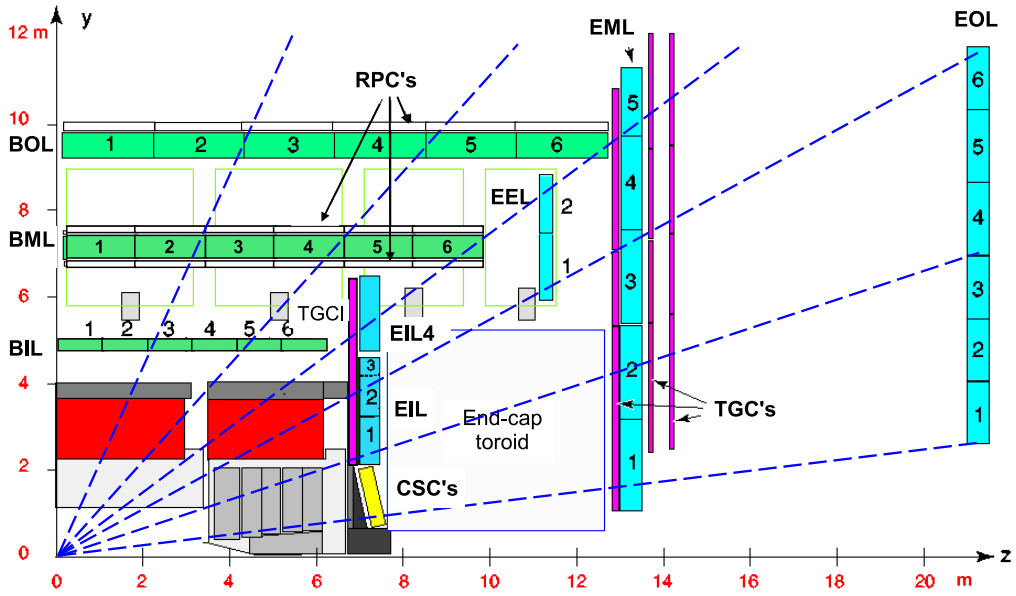

Figure 4.12: Diagram of the Muon System. The numbered modules are all precision detectors (MDTs).

the MDT chambers and their relative alignment to within 30 μm - can also be seen.

The maximum drift time in the MDTs is 700 ns, which is very slow compared to the 25 ns bunch spacing and in addition the tube is inactive ('dead') for the duration. Measuring this drift time improves the position resolution by a factor of 50, since it is roughly proportional to the distance between the track and the wire. The resolution is further improved by a factor of about of three by pressurizing the gas to 3 bars. Each chamber can measure one position coordinate to within 40 μm and one angle to within 3×10^{-4} radians.

The size and long dead-time of the MDTs limit the muon hit rate they can handle to about 150 Hz cm^{-2}. Cathode strip chambers (CSCs), installed in the forward region on each side ($2.0 < |\eta| < 2.7$), can cope with hit rates up to 1 kHz cm^{-2}. CSCs read out a segmented cathode as well as the perpendicular anode wires, giving two position coordinates, as shown in Figure 4.13b. The CSCs are relatively finely segmented: 2.5 mm anode separation, 5.1 mm cathode separation. The amplified flow of electrons to the anode wires induces a current on several cathode strips. The

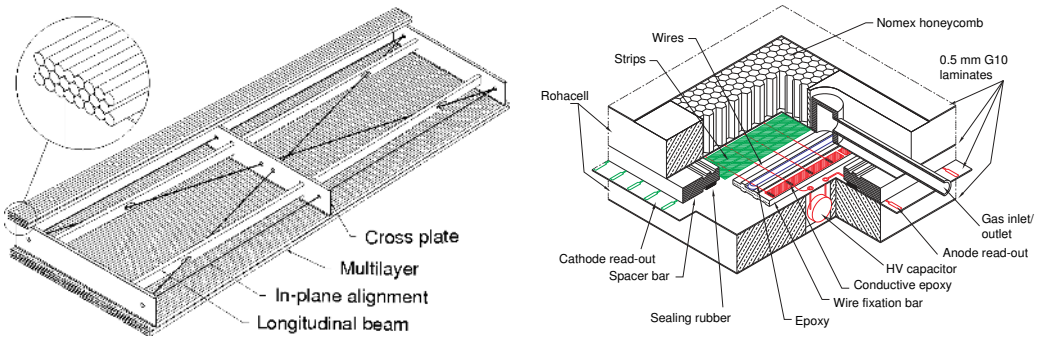

(a) An MDT chamber **(b)** A CSC chamber

Figure 4.13: The precision muon system

shape of the current distribution is used to further improve the position resolution.

Both CSCs and MDTs use a voltage of around 3 kV and a gas mixture of Ar and CO_2. They each have a similar drift time and neither can be used for triggering.

4.4.2 Triggering Muon System

Two technologies are used to make fast measurements of muons. Both typically give a spatial resolution of about 1 cm and a timing resolution of about 1 ns. They lead to trigger efficiencies generally over 99% for muons within the geometric acceptance of the detectors.

Resistive plate chambers (RPCs) cover the central region ($|\eta| < 1.05$). They use highly resistive anode and cathode plates instead of anode wires. Two 2 mm gas gaps are enclosed between the plates. Segmented strips on the plates, one in the ϕ-direction and one in the η-direction, are used to give the coordinates of a hit.

Thin gap chambers (TGCs) are used in the endcaps ($1.05 < |\eta| < 2.4$). They are traditional multi-wire chambers, in that the ionization current is read from the anode wires. To reduce the occupancy, TGCs have two or three thin gas gaps (2.8 mm), closely spaced (1.8 mm) wires and a fast drift time as a result of CO_2/n-pentane gas mixture. This mixture is flammable but operates safely thanks to an elaborate gas system.

4.5 Forward Detectors and Luminosity

Measuring luminosity is very important in order to estimate the total number of expected collisions, but the luminosity delivered to ATLAS varies constantly during each LHC fill. It is measured for each two minute period, referred to as a luminosity block and is determined independently using forward detectors, shown in Figure 4.14, and several algorithms [91, 92].

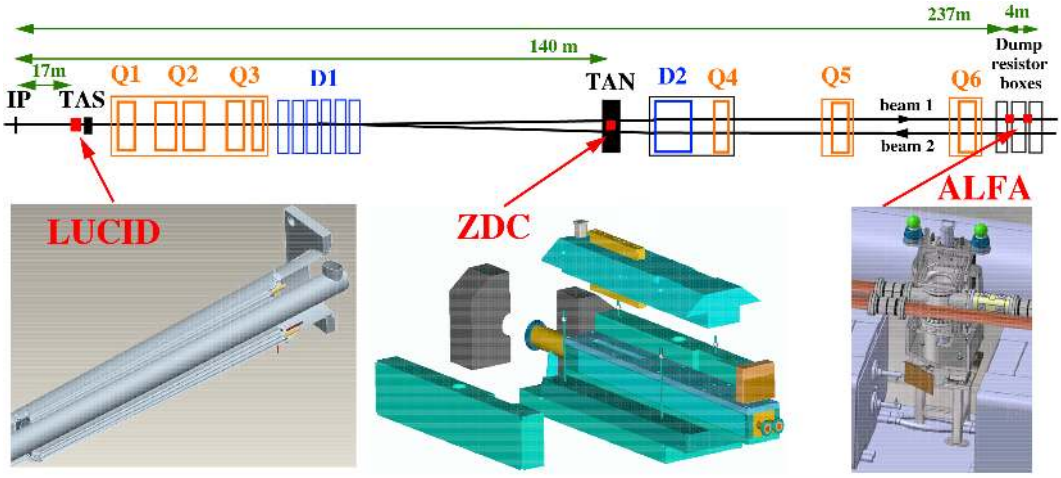

Figure 4.14: Forward Detectors at ATLAS.

LUCID (LUminosity measurement using Čerenkov Integrating Detector), which is made of gas Čerenkov tubes pointing towards the interaction point is found in the shielding near the muon endcaps, at $z = \pm 17$ m and $5.6 < |\eta| < 6.0$.

The BCM (Beam Conditions Monitor) is located at $z = \pm 1.8$ m and $r = 55$ mm ($|\eta| \sim 4.2$) and is generally considered to be part of the inner detector. It has an important role in the luminosity measurement, although it is primarily a beam abort monitor and can trigger a 'beam dump' automatically. It is made with diamond sensors which are designed to tolerate radiation doses even larger than the pixel b-layer.

The ZDC (Zero Degree Calorimeter) is only used in proton-proton collisions with luminosities below 10^{33} cm^{-2} s^{-1}, to avoid radiation damage. It was chiefly designed to measure the centrality in lead-ion collisions by detecting neutrons and

photons with $|\eta| > 8.3$. It also enhances the acceptance for diffractive processes and provides an additional minimum-bias trigger.

ALFA (Absolute Luminosity For ATLAS) is a tracking detector made of scintillating fibers inside Roman pots 240 m from the interaction point. It is used to measure elastically scattered protons - another important cross-check of luminosity.

LUCID and the BCM are used to count the number of events per beam crossing that have a hit on both sides (as well as the number with a hit on either side). The currents in the FCal and Tile calorimeter, discussed in section 4.3.1, are also used for monitoring luminosity. Event counting is only used to estimate *changes* in luminosity.

These measurements must be calibrated to give absolute luminosity by measuring the parameters A and n_p in Equation 3.2. The transverse cross section of the overlap between the beams (A) is measured with van de Meer (vdM) scans [93]. Performing a scan involves measuring the interaction rate while the beams are separated in steps of known distance. The horizontal and vertical beam sizes at the interaction point Σ_x and Σ_y are measured directly; typical values in May 2011 were 60 μm. These are combined to give $A = 4\pi\Sigma_x\Sigma_y$.

The number of protons per bunch n_p is measured with two independent beam current monitors - the Direct Current and Fast Beam Current Transformers. In 2011, this measurement was the dominant source of uncertainty in the luminosity. All luminosity measurements are generally found to be in good agreement, however, resulting in a total uncertainty of 3.7%.

4.6 Trigger and Data Acquisition System

ATLAS is designed to make precise measurements of a variety of very rare processes. Triggers are used to select events, based on reconstructed objects including electrons, photons, muons, jets, b-jets, τ-jets and $E_{\mathrm{T}}^{\mathrm{miss}}$.

The rate at which data can be recorded is limited, necessitating a compromise between the amount of information recorded for each event and the rate at which

events can be kept. Around 200 events can be recorded per second out of around 20 – 40 million bunch crossings.

The ATLAS trigger system selects events to record in three stages or trigger levels [94]. The first level (`L1`) can accept around 75,000 events per second. It makes a decision in 2.5 μs, during which time, complete information from around 100 events must be stored. The `L1` trigger uses information from dedicated calorimeter read-out electronics which sum cell energies into coarse trigger towers. Dedicated muon detectors are also used, as discussed in Section 4.4.2. Level two `L2` trigger decisions include inner detector information and reduce the rate of accepted events to around 3 kHz. The third trigger level, known as the event filter `EF`, uses more detailed information and can reconstruct entire events.

Triggers with low p_T thresholds are essential to observe low p_T objects, but if the event rate is too high, a trigger may be 'prescaled', meaning that only a preprogrammed fraction of the events that pass are recorded. To maintain a high acceptance for many kinds of analysis, the unprescaled trigger with the lowest threshold is used. Triggering on multiple objects also proves useful if, for example, events with two electrons are required.

It is essential to understand how different triggers affect the expected rate of reconstructed objects. This can be explored by comparing with independent triggers or similar triggers with a lower threshold, which may be prescaled. Ultimate validation of low threshold triggers comes from comparison with a random trigger, which selects a small sample of events.

Since the luminosity changes during each run, the trigger criteria are adjusted in order that ATLAS constantly records at the maximum possible event rate. The prescale rate for each trigger can be adjusted each two minute luminosity block.

4.7 Data quality and conditions in 2011

Many detector effects can result in poorly measured or entirely spurious physics objects. These effects are continuously monitored while the detector is in operation

and another series of checks are made after the data has been fully reconstructed. Various data quality flags are assigned to each luminosity block and can be used to remove it from the data sample.

The two most significant detector effects accounted for in this way are both associated with the LAr calorimeter: Trips of the high voltage applied across the liquid argon and noise bursts. Noise bursts are an extreme example of coherent noise. They affect a large number of channels for a few microseconds, but the origin of the effect is still unclear. Due to the short duration of noise bursts, sometimes good events can be recovered from luminosity blocks containing a noise burst by using an event flag.

In both cases, it is very important that the exact time and duration of the effect is correctly flagged so that the right luminosity blocks can be removed from the data set. The fraction of good quality data in each subdetector is shown in Figure 4.15.

ATLAS 2011 p–p run

Inner Tracking			Calorimeters				Muon Detectors				Magnets	
Pixel	SCT	TRT	LAr EM	LAr HAD	LAr FWD	Tile	MDT	RPC	CSC	TGC	Solenoid	Toroid
99.9	99.8	100	89.0	92.4	94.2	99.7	99.8	99.7	99.8	99.7	99.3	99.0

Luminosity weighted relative detector uptime and good quality data delivery during 2011 stable beams in pp collisions at √s=7 TeV between March 13th and June 29th (in %). The inefficiencies in the LAr calorimeter will partially be recovered in the future. The magnets were not operational for a 3-day period at the start of the data taking.

Figure 4.15: Luminosity weighted fraction of good quality data for runs between March 13th and June 29th. This corresponds to 1.25 fb^{-1} of the 2.0 fb^{-1} used in the analysis presented in this thesis.

Chapter 5

Data and Monte Carlo Samples

5.1 Data Samples

This thesis uses data corresponding to an integrated luminosity of 2.04 ± 0.08 fb^{-1} collected during the 2011 LHC run.

Data is only used if the LHC is in stable beam mode and the ATLAS magnets and relevant sub-detectors are all switched on. Various offline quality checks are also made. Some two minute luminosity blocks are removed from the data set, for example, many noisy cells are seen. A few individual events are also removed due to noise bursts in the LAr calorimeter.

Independent data samples are used for the electron and muon channels. In order to maximize the acceptance, the trigger chain with the lowest p_T thresholds are chosen out of triggers that are not prescaled. For the electron channel, events are required to pass through either a single electron or a dielectron trigger chain. The last level in the electron trigger chain (`EF`) uses an approximation of the medium level quality criteria using the hadronic leakage and shower shapes of calorimeter clusters.

`L1_EM14` → `L2_e20_medium` → `EF_e20_medium`

`L1_2EM7` → `L2_2e12_medium` → `EF_2e12_medium`

The last level in the muon trigger chain relies on software used for offline reconstruction, matching tracks in the muon system and inner detector. For the muon

channel, events are required to pass through one of two single muon trigger chains:

`L1_MU10` → `L2_mu18_MG` → `EF_mu18_MG`

`L1_MU10` → `L2_mu40_MSonly_barrel` → `EF_mu40_MSonly_barrel`

These triggers became prescaled in later high-luminosity runs which correspond to about one third of the data set. The trigger thresholds at `L1` were therefore increased:

`L1_EM16` → `L2_e22_medium` → `EF_e22_medium`

`L1_2EM10` → `L2_2e15_medium` → `EF_2e15_medium`

`L1_MU11` → `L2_mu18_MG_medium` → `EF_mu18_MG_medium`

`L1_MU11` → `L2_mu40_MSonly_barrel_medium` →
`EF_mu40_MSonly_barrel_medium`

The trigger efficiency was measured in data and MC by the Standard Model Diboson group. It was found to be slightly higher in MC than in data. A scale factor slightly less than one was therefore applied to each electron in the MC and propagated to the total event weight.

5.2 Monte Carlo Samples

Monte Carlo (MC) events are used to simulate physics processes as observed by the ATLAS detector [95]. Production of MC is divided into several steps. Event generators calculate matrix elements (ME) from the relevant Feynman diagrams and use these to produce four-vectors of particles from the proton-proton interaction and from their immediate decays. The evolution of quarks and gluons is modeled using the parton shower (PS) technique and the partons produced are grouped into color-neutral hadrons. Subsequent interactions with the detector are simulated using GEANT4 [96] and a detailed detector model. The energy deposited in active regions of the detector is digitized in analogy to the ATLAS read-out system. Finally, the results are passed through standard ATLAS reconstruction software to produce output in an identical format to the real data, with the addition of 'truth' information about the particles produced and their decays.

Jets are typically described by combining complimentary PS and ME approaches. The ME approach can provide an accurate description of well separated jets from hard interactions, but fails at low p_T as discussed in Chapter 1. The PS approach is more successful in describing roughly collinear, low p_T parton splittings.

5.2.1 Generators

Pythia [97] and Herwig [98] are general purpose MC generators. They calculate leading order (LO) MEs using perturbative QCD. Pythia then uses a p_T ordered PS, the Lund string model for hadronization and multiple parton interactions for the underlying event. Herwig uses an angular ordered PS and a cluster model for hadronization and the underlying event. Both Pythia and Herwig reweight events so that the highest p_T emission from the PS matches the ME calculation for one additional parton. However, they fail to produce enough jets in association with W and Z bosons to match experimental results [99]. The MC@NLO [100] generator includes Feynman diagrams with one loop, known as next-to-leading order (NLO) diagrams. The NLO parton-level integrator MCFM [101] is also used to cross check kinematic distributions including one loop corrections although it cannot be used to produce entire events.

Alpgen [102] and Sherpa [103] calculate LO MEs for up to five hard parton interactions. The difficulty with this is that, since the PS may subsequently split the hard partons from the ME, there are two ways of arriving at the same final state: for example, $Z+gg$ with no PS splitting and $Z+g$ with one PS splitting. A method of deciding when to use ME and PS must be used to avoid double counting [104].

The MLM matching algorithm [105] - used by Alpgen - and the CKKW algorithm [106, 107] - used by Sherpa - both introduce an extra arbitrary energy threshold. Partons from the ME are required to be hard and well separated according to the threshold. The CKKW algorithm modifies the PS in Sherpa by vetoing parton splittings more energetic than the threshold for matrix element production. Hard partons from Alpgen are passed to Pythia or Herwig for PS. The MLM algorithm clusters PS partons into jets and vetoes events if they do not match to

the hard partons. This can happen either if an extra jet is produced in the PS, if two partons are part of the same jet or if a hard parton does not become a jet.

5.2.2 Background Samples

The background processes simulated are Z+jets, top quark pair, single top, diboson and W+jets production. A summary of generators used is shown later in Table 5.3.

Background samples for $Z \to ee$, $Z \to \mu\mu$ and $Z \to \tau\tau$ are produced using ALPGEN in association with up to five hard partons. HERWIG is used for PS and hadronization, and JIMMY [108] is used for simulating underlying events. CTEQ6L1 parton distribution functions (PDFs) are used [109]. For systematic uncertainty studies, inclusive samples of $Z \to ee$ and $Z \to \mu\mu$ events with up to five hard parton interactions are generated with SHERPA with CTEQ6.6 PDFs [110].

Background samples for $t\bar{t}$ and single top production are generated with MC@NLO interfaced to HERWIG for hadronization and JIMMY for underlying events. CTEQ6.6 PDFs are used. A generator-level filter requiring one lepton with $p_T > 1$ GeV is applied to the $t\bar{t}$ sample. Diboson backgrounds of WZ, ZZ and WW processes are simulated with HERWIG and MRST2007LO* PDFs [111]. All decay channels are simulated. W+jets background samples are produced in the same way as the Z+jets samples. Lepton decays of all flavors, and up to five hard partons, are simulated with ALPGEN interfaced to HERWIG and JIMMY using CTEQ6L1 PDFs.

5.2.3 Signal Samples

Graviton signal samples using the original RS model [17] are produced with PYTHIA. The process $G^* \to ZZ \to \ell\ell qq$ with all lepton flavors ($eeqq$, $\mu\mu qq$ and $\tau\tau qq$) is generated for graviton masses of 350, 500, 750, 1000, 1250 and 1500 GeV. A warp factor of $k/\overline{M}_{pl} = 0.1$ is chosen.

Graviton signal samples using a modern RS model with fermions and bosons in the bulk [112] are generated with CALCHEP V2.56 [113], the results are passed to PYTHIA for showering and hadronization. CALCHEP is used because, unlike the PYTHIA generator, it retains all spin information for the graviton and Z boson

decays [114]. This is especially important due to the longitudinally polarized Z bosons. Samples with graviton masses of 300 to 900 GeV in 100 GeV steps are generated, again with all lepton flavors. A warp factor of $k/\overline{M}_{pl} = 0.1$ is also chosen.

Additional jets from initial state and final state radiation (ISR/FSR) could increase the signal acceptance. FSR near the leading jet is expected to be especially significant. Both effects was studied by producing signal samples with modified parameters in PYTHIA. MC events were not fully reconstructed: ATLFAST was used, which smears MC truth to estimate the energy deposited in the calorimeter. Only kinematic cuts were applied. ISR and FSR parameters were varied by a factor of two to four, as shown in Table 5.1. The largest variation in graviton acceptance for $350 < m_{G^*} < 1500$ GeV was 10%.

Parameter	PARP(67)	PARP(64)	PARP(72)	PARJ(82)
Nominal	4.0	1.0	0.192	1.0
ISR/FSR up	6.0	0.25	0.384	0.5
ISR/FSR down	0.5	4.0	0.096	2.0

Table 5.1: PYTHIA parameter settings used in the ISR/FSR varied samples for the graviton acceptance uncertainty.

The uncertainty on the graviton acceptance due to parton distribution functions (PDFs) was assessed using CTEQ6.6, NNPDF2.0 and MSTW2008NLO PDF sets as recommended by the PDF4LHC group [115]. Uncertainties in these PDF sets are parametrized in several additional sets each corresponding to independent uncertainty eigenvectors. PDF event weights are calculated using MC truth information about the flavor and momentum fraction x of the incoming partons and the total momentum transfer Q^2 for each event. The acceptance is calculated for all PDF sets and their eigenvector sets. The difference between the largest and smallest values of acceptance is taken as the uncertainty, shown in Table 5.2.

	CTEQ6.6	NNPDF2.0	MSTW2008NLO	Combined Uncertainty
$m_{G^*} = 350$ GeV $(eejj)$	0.87%	0.33%	0.39%	1.1%
$m_{G^*} = 350$ GeV $(\mu\mu jj)$	0.97%	0.34%	0.3%	1.3%
$m_{G^*} = 750$ GeV $(eejj)$	1.1%	0.62%	1.0%	1.4%
$m_{G^*} = 750$ GeV $(\mu\mu jj)$	1.3%	0.63%	0.68%	1.6%

Table 5.2: Relative uncertainty on the acceptance due to PDF uncertainty.

Process	Generator	Reference
W+jets	ALPGEN	[102]
Z+jets	ALPGEN, SHERPA	[102, 103]
$t\bar{t}$	MC@NLO	[100]
Single top (tb, tqb, tW)	MC@NLO	[100]
Inclusive Dibosons (WW, WZ, ZZ)	HERWIG	[98]
RS1 graviton signal	PYTHIA	[97]
'Bulk' RS graviton signal	CALCHEP	[113]

Table 5.3: Short summary of the event generator used for each physics process.

5.2.4 Cross sections and Branching Ratios

The production cross sections used for all relevant background processes are taken from the most recent and precise results available; they are summarized with for each process in Table 5.4. Uncertainties on the cross sections are combined with appropriate weights to give a contribution to the systematic uncertainty on the total background. The uncertainty on the W and Z boson production cross section is estimated using FEWZ [116]. It is given by the sum in quadrature of contributions from the MSTW2008NNLO eigenvector PDF sets, from varying the factorization and renormalization scales by two and one half respectively, and from varying $\alpha_s(M_Z)$ by $\pm 1\sigma$. Uncertainties on the other cross sections are given by the sum in quadrature of contributions from the relevant eigenvector PDF sets and from varying the factorization and renormalization scales by two and one half respectively.

Cross sections and branching ratios for the signal processes are calculated by

Process	Cross section		
W+jets	10.46 ± 0.52 nb	$\pm 5\%$	[117]
Z+jets	1.070 ± 0.054 nb	$\pm 5\%$	[117]
$t\bar{t}$	$164.57^{+11.45}_{-15.78}$ pb	$^{+7.0}_{-9.6}\%$	[118]
tb	$4.63^{+0.29}_{-0.27}$ pb	$^{+6.3}_{-5.8}\%$	[119]
tqb	$64.57^{+3.32}_{-2.62}$ pb	$^{+5.1}_{-4.1}\%$	[120]
tW	$15.74^{+1.34}_{-1.36}$ pb	$^{+8.5}_{-8.6}\%$	[120]
WW	44.9 ± 2.2 pb	$\pm 5\%$	[121]
WZ	18.5 ± 1.3 pb	$\pm 7\%$	[122]
ZZ	5.96 ± 0.30 pb	$\pm 5\%$	[123]

Table 5.4: Cross sections for background processes

the generator, either PYTHIA or CALCHEP. The production cross section for the graviton in the 'bulk' Randall-Sundrum model described is lower than in the RS1 model as a result of the suppression of $qq \to G^*$ production mechanism; it also falls slightly faster as a function of graviton mass. The branching ratio BR($G^* \to ZZ$) is 4.5% in the RS1 model; it takes the higher value of 13% in the 'bulk' Randall-Sundrum model, since decays to photons and light fermions are suppressed. This branching ratio is included in the values in Tables 5.5 and 5.6. The branching ratio for $ZZ \to \ell\ell jj$ is 14%.

5.2.5 Event Weights

Events in MC are weighted to predict the number of events seen in data. The event weight w is calculated as follows:

$$w = \frac{\sigma B \varepsilon_{\text{filter}} \mathscr{L}_{\text{int}}}{N'} w_{\text{pile-up}} w_{\text{eff}}, \tag{5.1}$$

where:

- σ is the production cross section (including the k-factor from LO to N(N)LO),
- B is the decay branching fraction,

m_{G^*} [GeV]	Cross section $\times$ BR [pb]
350	41.7
500	6.45
750	0.692
1000	0.128
1250	0.0291
1500	0.0082

Table 5.5: Cross section $\sigma(pp \to G^*)$ times branching ratio BR($G^* \to ZZ$) in the RS1 model.

m_{G^*} [GeV]	Cross section $\times$ BR [pb]
500	1.86
600	0.556
700	0.204
800	0.0800
900	0.0393

Table 5.6: Cross section $\sigma(pp \to G^*)$ times branching ratio BR($G^* \to ZZ$) in the 'Bulk' Randall-Sundrum model.

- $\varepsilon_{\text{filter}}$ is the Monte Carlo filter efficiency,
- $\mathscr{L}_{\text{int}}$ is the integrated luminosity,
- $w_{\text{pile-up}}$ is a weight associated with the number of interactions per bunch crossing simulated,
- w_{eff} is a scale factor chosen to match trigger and reconstruction efficiencies in data and
- N' is the sum of event weights from the generator.

The sum of event weights over the generated events $N' = \sum_N w_{\text{gen}}$. SHERPA applies a weight w_{gen} to each event in the Z+jets samples used. The MC@NLO generator also applies weights $w_{\text{gen}} = \pm 1$. Negative weights are a feature of interference in the MC@NLO amplitude calculation. All other event generators use event weights $w_{\text{gen}} = 1$.

Pile-up is simulated with MC by overlaying a number of additional pp interactions on the events of interest before simulation with GEANT4. The number of reconstructed vertices is suitable as a measure of the 'in-time' pile-up, ie. interactions occurring in the same bunch-crossing. However in the 2011 data, with a bunch spacing of 50 ns, the contribution from 'out-of-time' pile-up was significant. Pile-up is therefore parametrized by the average number of pileup interactions $\langle\mu\rangle$ in each luminosity block, which is estimated as part of the relative luminosity calculation.

Monte Carlo events are simulated with μ values corresponding to a wide range of luminosity scenarios. These are reweighted to match the $\langle\mu\rangle$ distribution in data. The μ distribution before MC reweighting is shown in Figure 5.1.

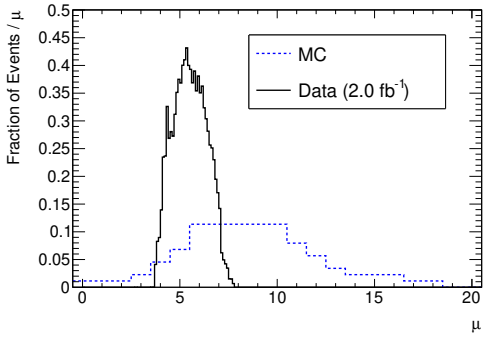

Figure 5.1: Number of pp interactions per bunch crossing μ for data and MC. Distributions are normalized to a unit area.

Chapter 6

Object Reconstruction and Selection

The methods of reconstructing physics objects, such as vertices, electrons, muons, jets, and $E_{\mathrm{T}}^{\mathrm{miss}}$ have been chosen as a compromise between maximizing the efficiency for true objects and rejection of mis-identified backgrounds. The event selections were guided by those used in the search for the Higgs boson in the same final state [124].

6.1 Vertex

All events are required to have a primary vertex reconstructed from at least three tracks ($p_T > 150$ MeV) so as to be consistent with a hard-scatter proton-proton collision.

6.2 Electrons

6.2.1 Reconstruction and Identification

Electrons are first identified using a sliding-window algorithm. The EM calorimeter is divided into an η-ϕ grid of 0.025×0.025 and the energy in cells in all longitudinal layers is summed to give 'towers'. A 5×5 tower window slides over the grid of

towers. A seed is formed if the combined E_T in the window is 3 GeV or more. A 3×3 window, which is less sensitive to noise, is then used to estimate the position of a seed. If two seeds are found within a 2×2 square, the lower E_T seed is rejected.

A rectangular cluster of cells is formed around this seed, the size of which depends on position. The precise cluster position, hadronic leakage and shower shapes for each layer are then calculated. Nearby tracks ($\Delta\eta < 0.2$ and $\Delta\phi < 0.1$) are extrapolated through the calorimeter and $\Delta\eta$ and $\Delta\phi$ are calculated in each layer. The closest track in the second layer is used in the energy calculation. Matching of TRT-only tracks depends only on ϕ since very limited track η information is available. Calorimeter variables plus track quality, track/cluster matching and transition radiation information are used to define three levels of electron quality: loose, medium and tight.

Loose electrons are identified based on information from the calorimeters. Requirements are made on the hadronic leakage and on lateral shower-shape in the middle layer of the LAr calorimeter. Since collision data became available, electromagnetic showers have been seen to be wider in data than in MC. Requirements on lateral width of the shower have therefore been loosened. They are placed in the tail of the relevant distributions for signal in order to reduce the systematic uncertainty from mis-modeling of the shapes.

Medium electrons are selected based on several variables from the first layer of the LAr calorimeter and on the tracking variables in addition to the loose requirements. The first layer of the calorimeter is finely segmented in η 'strips' to provide effective rejection of $\pi^0 \to \gamma\gamma$ decays which often have two energy maxima. If two maxima are found, a requirement is applied on the energy of the second maximum and the difference between minimum and the second maximum. Requirements are made on the total shower width, the shower width over three strips around the maximum energy deposit and the fraction of energy deposited outside these three central strips. Track quality requirements are made on the number of hits in the pixels and SCT and the transverse impact parameter. Finally a requirement is made on $\Delta\eta$ between the cluster and the extrapolation of the track to the calorimeter.

Tight electrons must pass several requirements in addition to the medium set. Extra requirements are made on the number of pixel hits to reject electrons from photon conversions. To reject charged pions, requirements are made on the number of TRT hits and on the fraction of high-threshold hits in the TRT. Further requirements are made on the track-cluster separation in η and ϕ.

6.2.2 Selection

Medium electrons are used in this thesis. Electrons candidates are also required to be isolated to reject jets. Jets can mimic electrons especially if they contain photons or semileptonically decaying heavy flavor hadron. In both cases the reconstructed electron tends to be surrounded by larger energy deposits than electrons from electroweak processes such as a leptonic Z boson decay. The sum of track p_Ts around the electron track in a cone of radius 0.2 is required to be less than 10% of the electron p_T.

Electrons candidates are rejected in dead or poorly understood regions of the calorimeter, for example the 'crack region' between the barrel and endcap ($1.37 < \eta < 1.52$). For a period corresponding to about 40% of the data set a small region of the LAr calorimeter could not be read out. The effect is simulated in MC, by removing electrons in this region for an appropriate fraction of the MC events.

6.2.3 Energy Corrections

After a calorimeter cluster has been identified as an electron, several energy corrections of a few percent are applied to correct for:

- the sampling fraction is different for electrons, muons and jets which varies as a function of shower depth.
- modulations of the calorimeter response. Much of the variation in the the thickness of the layers of LAr and lead and the high voltage is accounted for at the cell level. However, residual corrections are made as a function of η and ϕ.

- lateral and longitudinal leakage. The energy deposited outside the cluster is parameterized as a function of η, ϕ, energy and shower depth.
- energy deposited upstream. One to two percent of the energy of an electron is typically deposited before the presampler. In the 'crack region', around $|\eta| = 1.5$, the fraction can be as high as 10 – 20% although an estimate of the energy losses can be made using extra scintillators in this region.
- dependence on the point of impact in the cell in the middle layer.

Many of these corrections were derived using test beam electrons [125, 126]. Residual corrections are derived in situ by a dedicated group, using $J/\psi \rightarrow ee$ and $Z \rightarrow ee$ samples and their well-known line-shapes [127]. The corrections applied to data, as a function of η, are shown in Figure 6.1. They systematic uncertainty on this correction is propagated to the final result by using central values $\pm 1\sigma$.

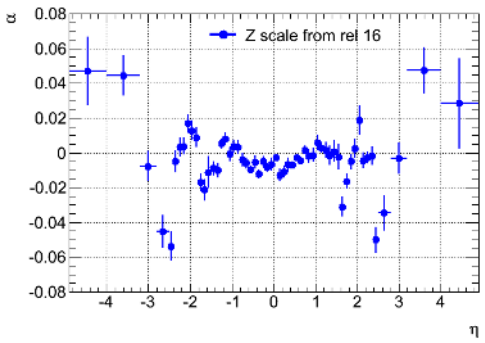

Figure 6.1: Electron Scale Corrections (2011)

The electron p_T resolution in MC does not precisely match the data. The $Z \rightarrow ee$ line shape is also used to derive smearing factors for MC to reproduce the resolution measured in data. The energy is smeared before applying any p_T requirement. Again, the systematic uncertainty on this correction is propagated to the final result.

The electron energy and p_T use track p_T information combined with the energy of the calorimeter cluster. The electron η is also typically taken from the higher resolution tracker. However, if the electron track has less than four silicon hits then the track η measurement is not used since it would rely on the very poor η resolution

of the TRT. In this case, only the calorimeter energy is used. The calorimeter η is used with the help of the 'pointing' of the cluster.

6.2.4 Efficiency

The loose electron requirements provide excellent identification efficiency (above 95%), but low background rejection. Medium requirements increase the jet rejection by a factor of 3-4 with respect to the loose requirements, while reducing the identification efficiency to about 90%. The tight efficiency reaches about 80% and is more strongly dependent on p_T. Tight requirements are not appropriate for this analysis due to the loss of signal acceptance with two electrons.

Electron reconstruction and identification efficiencies in MC do not fully reproduce those measured in data. They are measured by a dedicated group using the 'tag-and-probe' method on $Z \rightarrow ee$ events. The scale factor is defined as the ratio of the efficiencies in data and MC. A scale factor for each electron is applied as an event weight which is then used in all histograms. Scale factors for medium electrons are roughly 0.97 depending a little on η. Systematic uncertainties on the scale factors are also provided and are propagated to the final result

6.3 Muons

Two muon algorithms are used: combined muons and segment-tagged muons. Combined muons are first identified in the muon system when three-hit tracks are available. Two-coordinate hits from the trigger chambers or CSCs are used to define a region of activity. A track is then fitted to three MDT hits in this region and extrapolated to the primary vertex. An estimate of the total loss, including the energy deposited in the calorimeter, is added back in. This track is then associated with an inner detector track. The combined track parameters are calculated with a χ^2 fit of muon system and inner detector track parameters.

Segment-tagged muons begin with inner detector tracks not already used as part of combined muons. These are associated with two-hit track segments. Muons in

η-ϕ regions where there are less than three layers in the muon system can thus be recovered.

Several recommended requirements are made on the quality of the inner detector track:

- a b-layer hit,
- at least two pixel hits and
- at least six SCT hits.
- For the last three requirements, a dead sensor crossed by the muon track counts as a hit. However, no more than three dead sensors in the pixels and SCT are allowed along the trajectory.
- The track must be consistent with the primary vertex. The inner detector track must intersect the beam axis within 10 mm of the primary vertex in the z direction. In addition, the distance of closest approach in the x-y plane (d_0) divided by its uncertainty must be less than 10.
- The track must have fewer than six TRT hits if it is in the region $|\eta| < 1.9$.
- The tracks is rejected if the sum of TRT hits is greater than five and the fraction of TRT outlier hits is greater than 90% (as long as the muon track falls within the η acceptance of the TRT).

The same definition of isolation is used for muons as for electrons. The sum of track p_Ts around the muon track in a cone of radius 0.2 must be less than 10% of the muon p_T.

6.3.1 Energy Corrections

The momentum resolution of the muon system, shown in Figure 6.2, follows the inner detector resolution equation 4.1 with an extra term inversely proportional to the p_T:

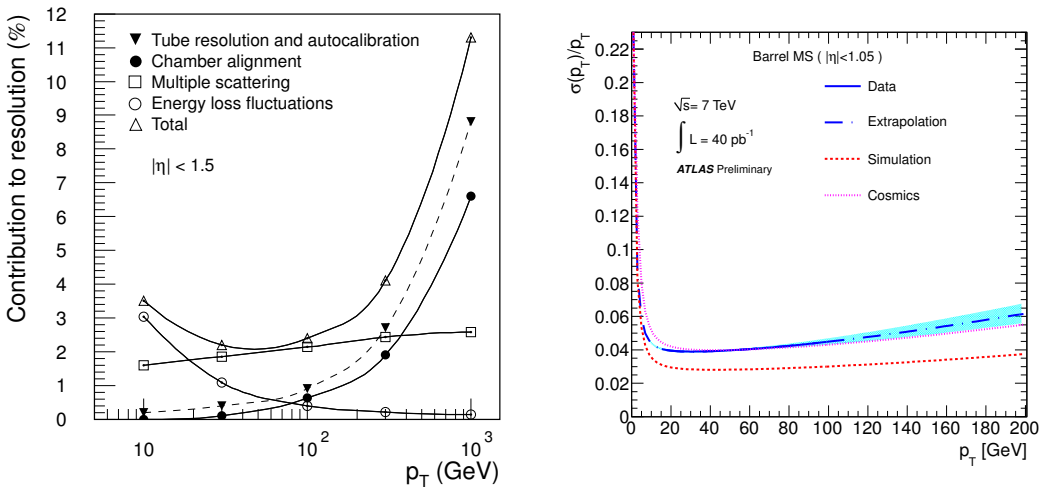

(a) Contributions to the muon p_T resolution (Technical Design Report 1997)

(b) Measured muon p_T resolution (2011)

Figure 6.2: Muon p_T resolution

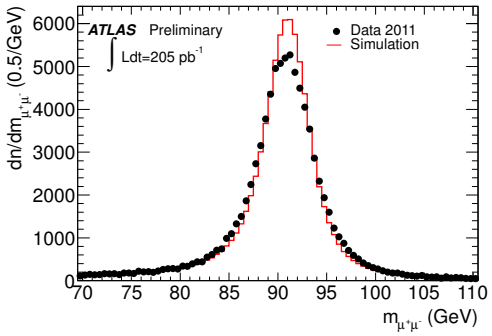

Figure 6.3: Comparison between data and MC for the Z lineshape.

$$\frac{\delta p_T}{p_T} = p_T \cdot C_{curve} \oplus C_{MS} \oplus \frac{C_{loss}}{p_T}, \tag{6.1}$$

The first term ($\propto p_T$) comes from the 50 μm precision on the sagitta. The second term comes from multiple scattering in the material. In 2011, it has been measured to be a little worse than the design specification. The last term corresponds to the loss of energy before the muon system. This contribution is reduced by using the energy deposited in the calorimeter, roughly 3 GeV in the barrel, less in the endcaps.

The muon p_T resolution is not fully reproduced in the MC, as can be seen in Figure 6.3. Smearing factors were derived using $Z \to \mu\mu$ events from 2011 data by a dedicated group [128]. These are used to adjust the p_T resolution in the MC to match the data. Both the muon spectrometer and inner detector track are smeared and the result is propagated to the combined muon p_T measurement. Systematic uncertainties on the smearing factors were also derived for the inner detector, muon spectrometer tracks. These are propagated to the final result by 'over-smearing' ('under-smearing') the muon p_T using the smearing factors once for the MS and once for the ID. The total uncertainty is taken from the maximum variation of these two uncertainties.

A small correction to the muon p_T scale is applied to MC along with the smearing. The uncertainty associated with this is evaluated by noting the change in acceptance with and without the correction.

6.3.2 Efficiency

Using segment-tagged muons considerably improves the reconstruction efficiency as shown in Figure 6.4. The reconstruction efficiency has been measured in 2011 data to be as high as 98% for most η regions. The efficiency is lower around $\eta = 0$ due to a gap in the muon system as shown in Figure 6.5.

Muon reconstruction efficiency is also not fully reproduced in MC. A small correction factor is derived also using $Z \to \mu\mu$ events. This is applied to muons in MC. The systematic uncertainty is estimated by noting the change in acceptance.

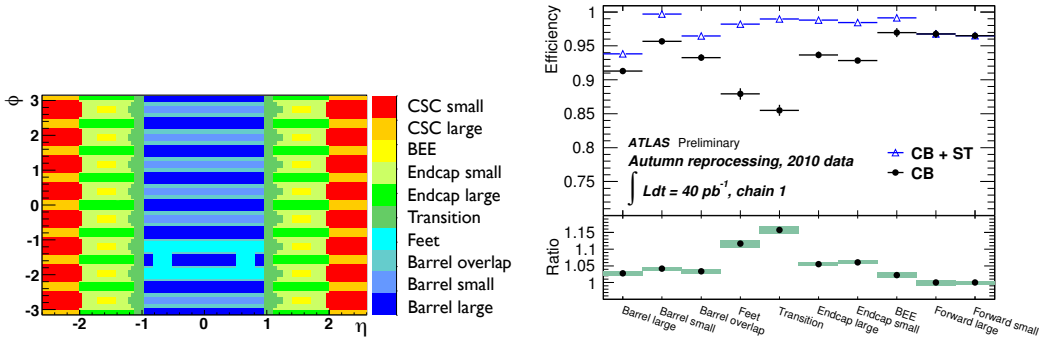

(a) The regions of the ATLAS muon system in η-ϕ.

(b) The efficiency for combined and segment-tagged muons in each of the η-ϕ regions.

Figure 6.4: Muon reconstruction efficiency in 2010 data [129]. About 85 – 90% of muons are first identified in the muon system using the combined (CB) muon method. The segment-tagged (ST) method is especially useful for recovering muons in η-ϕ regions where the muon system coverage is limited.

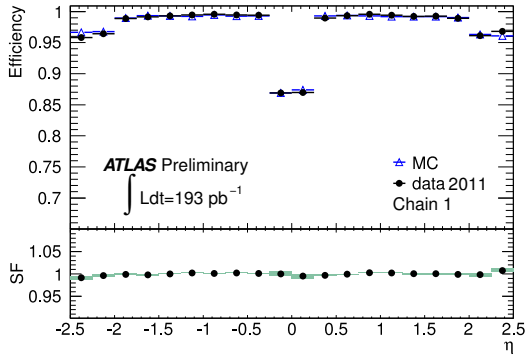

Figure 6.5: Preliminary studies with 2011 data show that the muon reconstruction efficiency is as high as 98% across most of the detector acceptance. Small deviations between data and MC are accounted for.

6.4 Jets

When quarks or gluons are produced with high momentum, QCD confinement leads to the production of a parton shower and hadronization, producing collimated jets of hadrons. Since the resulting jets are color-neutral in the final state, **jets cannot be mapped uniquely to partons**. However, jets are studied in order to estimate the properties of the original partons as much as possible. For example to precisely reconstruct the mass of a hadronic Z boson.

6.4.1 Jet Algorithms

A jet algorithm is a set of mathematical rules that takes many vectors and assigns them to groups. Jet algorithms are applied to many different kinds of object. Standard jets at ATLAS are groups of calorimeter clusters. An independent cross check of these calorimeter jets is provided by using the same jet algorithm on tracks. In MC events, jet algorithms are used on particles at truth level. In triggering at ATLAS, jet algorithms are used on trigger towers.

The jet algorithm used determines the number of jets in an event. It is important to note that **jets have no existence independent of the algorithm used to reconstruct them**. It is therefore essential that algorithms can be used consistently between theory and experiment [130].

There are a number of other important considerations when choosing jet reconstruction methods at the LHC. Effects that cannot be modeled with perturbative QCD, generally should have a effect of less than around a GeV. The hadronization stage of jet formation is modeled with MC tuned to data. Another intrinsic aspect of proton-proton collisions is partons not involved in the hard scatter, which are collectively known as the "underlying event". The effects of hadronization and the underlying event on the properties of jets must be small and stable. High energy jets are used for triggering in events that may contain dozens of jets. The triggering algorithms must be fast and yet must correspond well to the jets reconstructed offline. High-energy jets of interest will be surrounded by large numbers of low-energy

deposits from pile-up. The effect of pile-up as well as electronic noise must also be small.

A wide variety of jet algorithms are available. Historically, the first to be used try to maximize the energy in a cone of a fixed size. Such cone algorithms are simple and have a well-defined shape. However, naive cone algorithms are not appropriate for use at ATLAS. Scanning over all the cells in the calorimeter is computationally intensive. This can be mitigated by using the highest energy deposits to 'seed' a cone algorithm. However, many seeded cone algorithms suffer from infrared and collinear divergences. This means that collinear splittings of input partons or the addition of arbitrarily soft particles can lead to large fluctuations in jet observables, as shown in Figure 6.6. Algorithms with these properties are more sensitive to non-perturbative "soft" physics, such as hadronization and the underlying event and they generally cannot be implemented in higher-order QCD calculations.

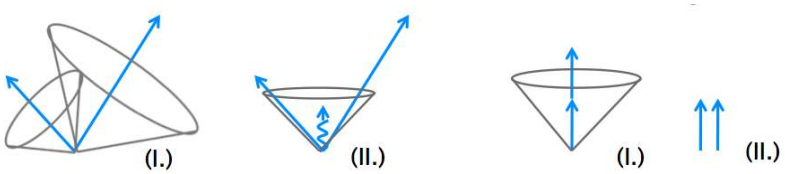

Figure 6.6: Infrared and collinear divergences: the two diagrams on the left (I. & II.), differ only by a very soft particle, yet a non-infrared-safe jet algorithm reconstructs a different number of jets. The two diagrams on the right (I. & II.), differ only by a collinear splitting of particles, yet a non-collinear-safe jet algorithm reconstructs a different number of jets [131].

Three infrared- and collinear-safe clustering algorithms used at ATLAS: k_t [132], anti-k_t [133] and Cambridge/Aachen [134, 135]. These are defined as follows, where $n = +1$, -1 and 0, respectively. For each cluster i, define $d_i = p_{T,i}^{2n}$, and for each pair of clusters define:

$$d_{ij} = \min(d_i, d_j)\frac{\Delta R_{ij}^2}{R^2} \tag{6.2}$$

where R is the distance parameter or cone size of the jet.

- Find the minimum of all d_i and d_{ij}.

- If $d_{\min}$ is d_{ij}, merge clusters i and j or
- if $d_{\min}$ is d_i, cluster i is a jet.
- Repeat until no clusters remain.

Clusters are merged by summing their four-vectors, although other recombination schemes are possible.

The k_t algorithm (with $n = +1$) merges nearby soft particles first. This gives a close correspondence between experimentally reconstructed jets and those from theoretical predictions and has been used at many e^+e^- collision experiments [136]. However, in the busier LHC environment, k_t jets often have irregular shapes which can make them less stable and difficult to calibrate.

Using the anti-k_t algorithm (with $n = -1$), soft particles are first merged to hard particles. Nearby soft particles therefore do not change the shape of a jet, but hard particles do. For two overlapping jets, if $p_{T,1} \gg p_{T,2}$ then jet 1 will be conical; jet 2 will miss the part overlapping with jet 1. However, if $p_{T,1} = p_{T,2}$ then the two jets will be divided equally by a straight line. For this reason, the anti-k_t algorithm is much less sensitive to nearby soft radiation than other clustering algorithms, for example from pile-up. It is used as the default jet algorithm for most physics analyses, including this one.

6.4.2 Energy Corrections

Several corrections are applied to the energy of calorimeter jets for the best possible comparison with truth particle jets and to optimize the jet energy resolution. Most of the corrections are derived from MC, where the relationship between jets from truth particles and jets reconstructed in the calorimeter or tracker can be directly studied. Several data samples including γ+jet and Z+jet events [137] are used to study the uncertainty on the jet energy scale. It a significant source of systematic uncertainty in this analysis.

The `EM+JES` calibration scheme is used to corrected jet energies. This is a relatively simple calibration scheme using mostly MC derived corrections. It is divided

into three stages. The first stage is a correction for pile-up. Contributions to the jet energy from additional pp collisions is subtracted. This offset correction was extracted from 2010 data using a fit to the distribution of jet energies as a function of η and number of reconstructed vertices. The correction also varies as a function of the bunch spacing and the instantaneous luminosity. Next, the primary vertex associated with tracks with the highest sum of p_Ts is chosen. The jet position, and therefore its p_T, is reset relative to this primary vertex rather than the nominal interaction point. Several corrections to the jet energy and position are then applied.

Since ATLAS uses a non-compensating calorimeter, the response to electrons is greater than to hadronic particles, especially in the LAr. This is the largest part of the jet energy scale correction. The jet energy is also corrected for losses in dead regions of the calorimeter using the EM scale energy deposited in neighboring cells. The highest energy jets may punch through the entire calorimeter. A correction is applied for this longitudinal leakage. Corrections for 'out-of-cone' energy deposits are also derived.

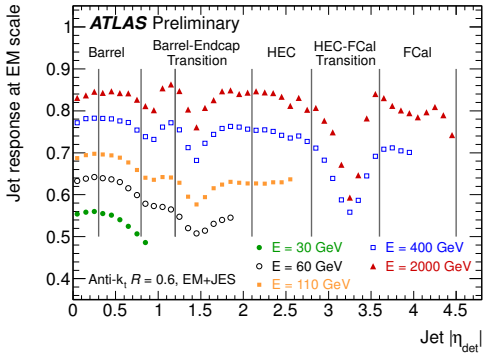

Figure 6.7: EM scale jet response, as determined in 2010 data. This is the inverse of the jet energy scale correction. [138].

The inverse of the jet energy scale, as calculated from 2010 data is shown in Figure 6.7. The correction to the highest energy jets is only about 15 – 20%, however for the lowest energy jets used in this thesis, $p_T > 25$ GeV, the JES correction is almost two. The uncertainty on the jet energy scale, which is a significant source of

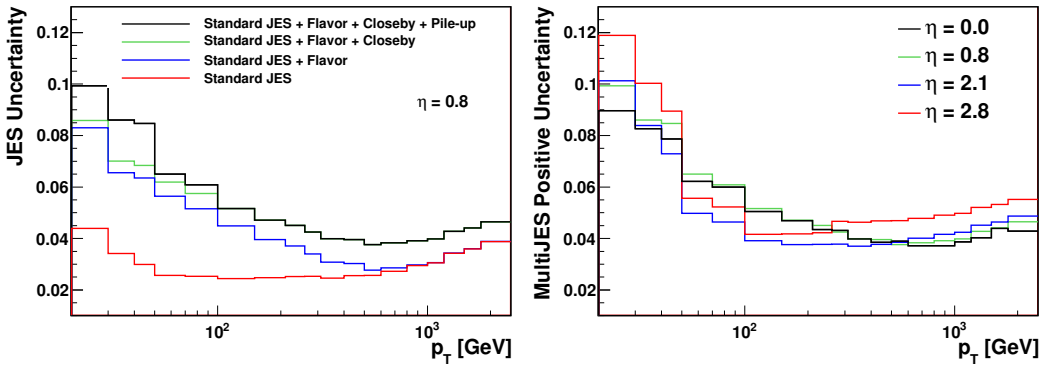

(a) Contributions to the JES uncertainty **(b)** Jet energy scale uncertainties as a function of p_T

Figure 6.8: Jet Energy Scale uncertainty in 2011 data.

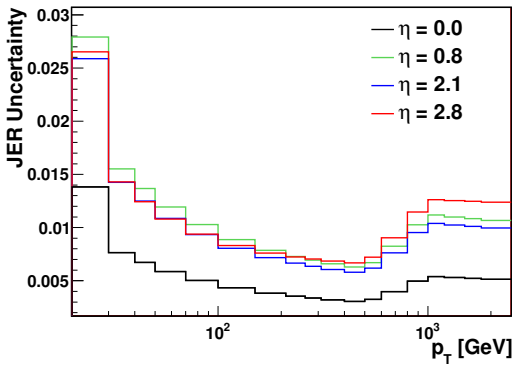

Figure 6.9: Jet Energy Resolution uncertainty in 2011 data.

systematic uncertainty in this analysis is correspondingly large. Various components of uncertainty on the jet energy scale are shown in Figure 6.8a. The total uncertainty, as a function of p_T and η is shown in Figure 6.8b. When only a small fraction of the jet energy is directly measured, the jet resolution tends be poor. The uncertainty on the jet energy resolution is shown in Figure 6.9, as a function of p_T and η.

The effect of the hole in the LAr calorimeter is accounted with the use of an alternative correction for the jet energy lost due to dead cells is used. Instead of the default cell-based correction, the full shape of the calibrated jet is used. Using this alternate correction, events are vetoed if a jet with $p_T > 40$ GeV is found in the hole. The same veto (using the default correction for dead cells) is applied to an appropriate fraction of MC events. The LAr hole is defined by $-0.1 < \eta < 1.5$ and $-0.9 < \phi < -0.5$ for these purposes.

6.4.3 Jet Mass

Calorimeter clusters used to forming a jet are considered massless, but the jet acquires mass from the invariant mass of its many constituent clusters. It is strongly affected by clusters a the edge of the cone. Additional energy deposits near the edge of the cone could have a a small effect on the jet energy but a large effect on the jet mass. An estimate of the jet mass scale (JMS) uncertainty is made following the procedure used for large cone-size jet algorithms [139]. An independent cross check of the jet mass is provided by track-jets, which are defined by applying the same jet algorithm to inner detector tracks. Systematic uncertainties on track-jet mass are assumed to be uncorrelated with calorimeter jets.

The ratio of jet mass to track-jet mass is shown in Figure 6.10. Leading jets in Z events are used. Jets are required to be in the central region ($|\eta| < 1$) of the tracking detector, which includes 48% of the sample. The track-jet mass is lower than the calorimeter jet mass because around half of the energy in jets is carried by neutral particles. This is accounted for by comparing this ratio to MC in a 'double

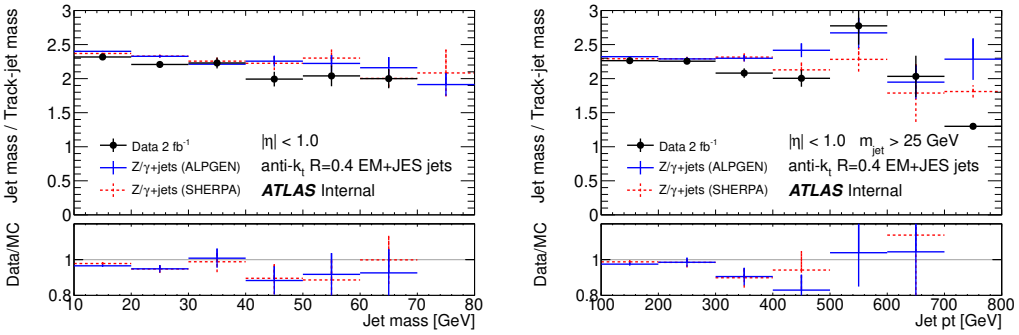

(a) **(b)**

Figure 6.10: Ratio of jet mass to track-jet mass.

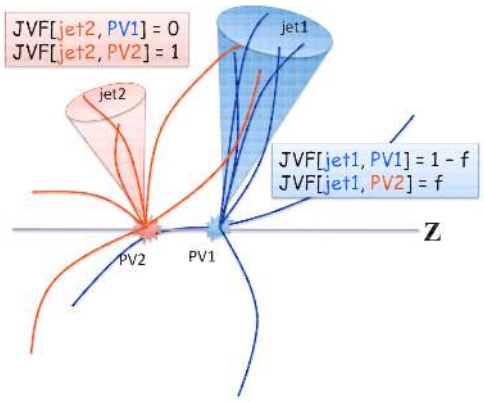

Figure 6.11: The Jet Vertex Fraction variable. JVF = 1 corresponds to a jet associated only with tracks from the primary vertex.

ratio':

$$R^{m}_{\text{track-jet}} = \frac{\left\langle \frac{m_{\text{jet}}}{m_{\text{track-jet}}} \right\rangle_{\text{data}}}{\left\langle \frac{m_{\text{jet}}}{m_{\text{track-jet}}} \right\rangle_{\text{MC}}} \tag{6.3}$$

The maximum deviation of the double ratio from one, as shown in the bottom plot in Figure 6.10a, is 10%. This is symmetrized and taken as JMS uncertainty. This uncertainty may be overestimated since it also includes systematic uncertainties on track-jets and a large statistical uncertainty.

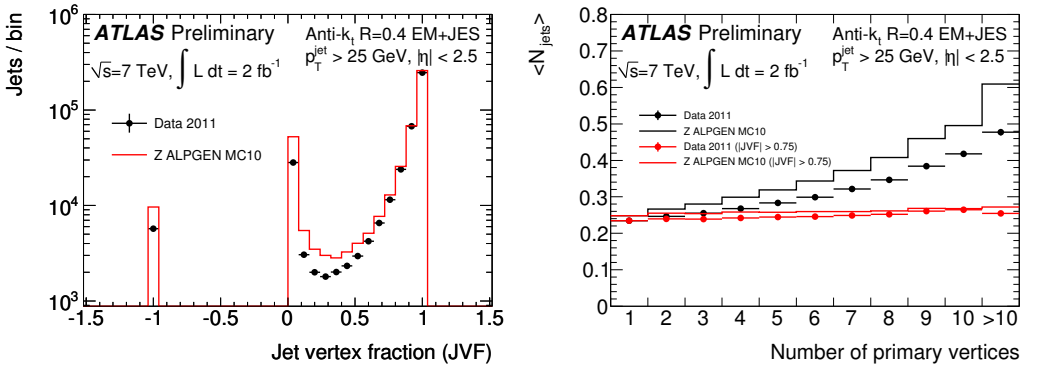

(a) JVF in Z boson events.

(b) Average number of jets in data as a function of number of vertices (with and without JVF).

Figure 6.12: Jet Vertex Fraction (JVF) in 2011 data.

6.4.4 Jet Selection

The jet vertex fraction (JVF) is used to reject jets from pile-up. It is defined by the fraction of tracks associated with the jet that point to the primary vertex, as shown in Figure 6.11. The primary vertex with the highest sum of track p_Ts is used. The distribution of `JVF` is shown in Figure 6.12a. the fraction of jets with low values is overestimated in MC. However, the agreement is good in the region where the requirement is applied. The requirement is very effective at reducing the contribution from pile-up, as shown in Figure 6.12b. Jets without matched tracks, or beyond the tracking acceptance ($|\eta| > 2.5$) have `JVF` $= -1$ and are accepted.

Jet quality criteria are designed to reject jets that result from hardware problems such as coherent noise in the EM and HEC calorimeters as well as from non-collision backgrounds: directly from the LHC beam or from cosmic rays [140]. Requirements are applied on the time and the pulse shape of the energy deposit as measured by the calorimeter. Jets are also rejected if a large fraction of the energy is lost in dead cells or inactive regions such as the barrel-endcap transition region.

Anti-k_t algorithm with cone size $R = 0.4$ is used and the following requirements are made:

- $|\eta| < 2.8$. The value of η defined at the EM scale is used.
- $p_T > 25$ GeV. Using `EM+JES` calibrated p_T.
- $|\texttt{JVF}| < 0.75$
- jet quality criteria.

6.5 Missing Transverse Energy

In this analysis, missing transverse energy ($E_{\mathrm{T}}^{\mathrm{miss}}$) is used to select top quark pair events, which have high $E_{\mathrm{T}}^{\mathrm{miss}}$ as a result of neutrinos escaping. Initially, the $E_{\mathrm{T}}^{\mathrm{miss}}$ is calculated from the vector sum of transverse energy (at EM scale) in all calorimeter cells. However, after objects have been defined, refined calibrations are applied to the associated cells to improve the $E_{\mathrm{T}}^{\mathrm{miss}}$ reconstruction [141].

6.6 Overlapping Objects

6.6.1 Electrons and Jets

The jet reconstruction algorithm is applied to all calorimeter energy deposits. All electrons are therefore also reconstructed as jets. These must be removed from the list of available jets. Jets close to selected electrons ($\Delta R(j, e) < 0.3$) are rejected. Objects that fail any of the electron selection criteria may be considered as a jet.

6.6.2 Electrons

Occasionally a single electron is reconstructed as two distinct electrons. If two electrons are found very close to each other ($\Delta R(e, e) < 0.1$) the electron with lower p_T is rejected. This was shown to have a negligible effect on the reconstruction of $Z \to ee$ decays from a graviton with a mass up to 1.5 TeV.

6.6.3 Electrons and Muons

A muon sometimes radiates a photon in the calorimeter. This photon may be reconstructed as an electron, using the muon track. Electrons close to muons ($\Delta R(\mu, e) < 0.1$) are rejected.

Chapter 7

Event Selection

Three kinds of event samples are selected. First a large preselected sample is chosen. From this, signal regions and control regions are selected. Signal regions are based on the characteristics of a particular new process in order to maximize sensitivity to it. Control regions are important for comparing expected background to data. Ideally a control region should be very similar to the signal region and yet contain a negligible amount of signal.

This is a search for gravitons decaying to a pair of Z bosons, where one of the Z bosons decays leptonically, to electrons or muons, and the other hadronically. Since the graviton is expected to have high mass, both Z bosons are likely to have high p_T.

The leptons are used for triggering the event as discussed in Section 5.1. More precise offline cuts are then made on the leptonic Z boson in the preselection. Definition of the signal region involves identification of a hadronic Z boson candidate and cuts on the p_Ts of the Z bosons.

7.1 $Z \to \ell\ell$ Preselection

This analysis selects a final state with two high p_T leptons (electrons or muons). The p_T thresholds and object quality criteria are the following:

- two electrons with $p_T > 20$ GeV or

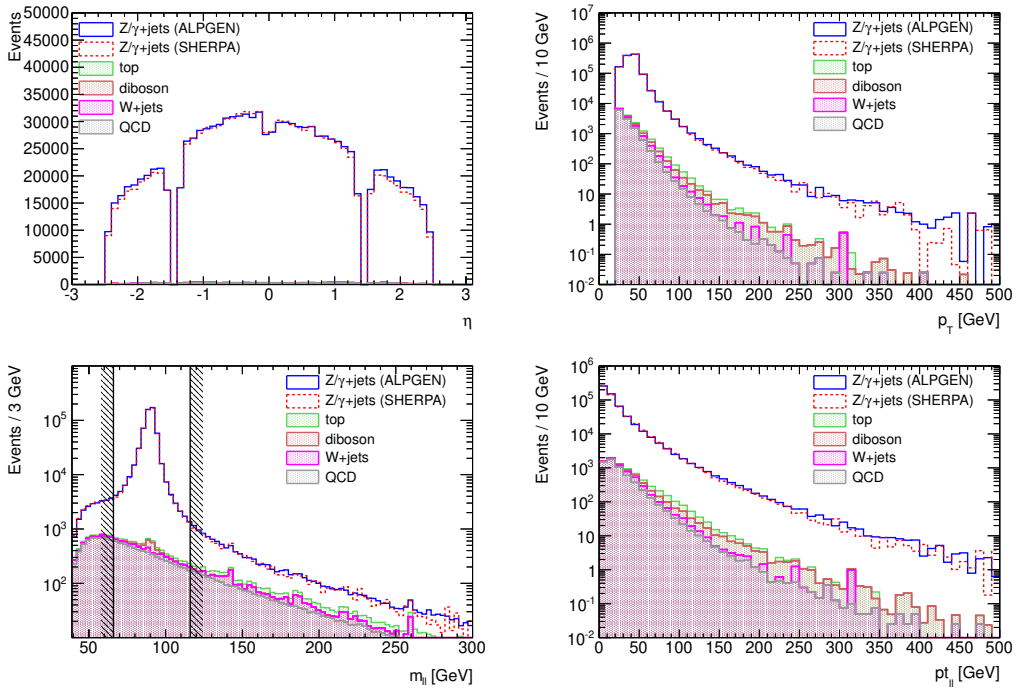

Figure 7.1: Distributions of η and p_T for preselected electrons. Dielectron mass and p_T are shown on the bottom row. The electron η is asymmetric due to a small dead region in the calorimeter in part of the data set. A Z boson mass window cut is made on the dielectron mass, indicated by the hashed bands. Events outside this region are shown for reference only and are not used.

- two oppositely-charged muons with $p_T > 20$ GeV,
- dilepton mass consistent with a Z boson ($|m_{\ell\ell} - 91\text{ GeV}| < 25$ GeV) and
- no other electrons or muons with $p_T > 20$ GeV.

The opposite-charge requirement is not made for the electrons because of relatively high charge misidentification rate, which can result from a poorly reconstructed inner detector track. Studies using 2011 data indicate that the rate depends on η. It varies from about 1% for $0 < |\eta| < 0.8$ to 7% for $2.0 < |\eta| < 2.47$. For muons, the charge measured in the inner detector is required to agree with that measured in the muon system. This reduces the charge misidentification rate to negligible levels.

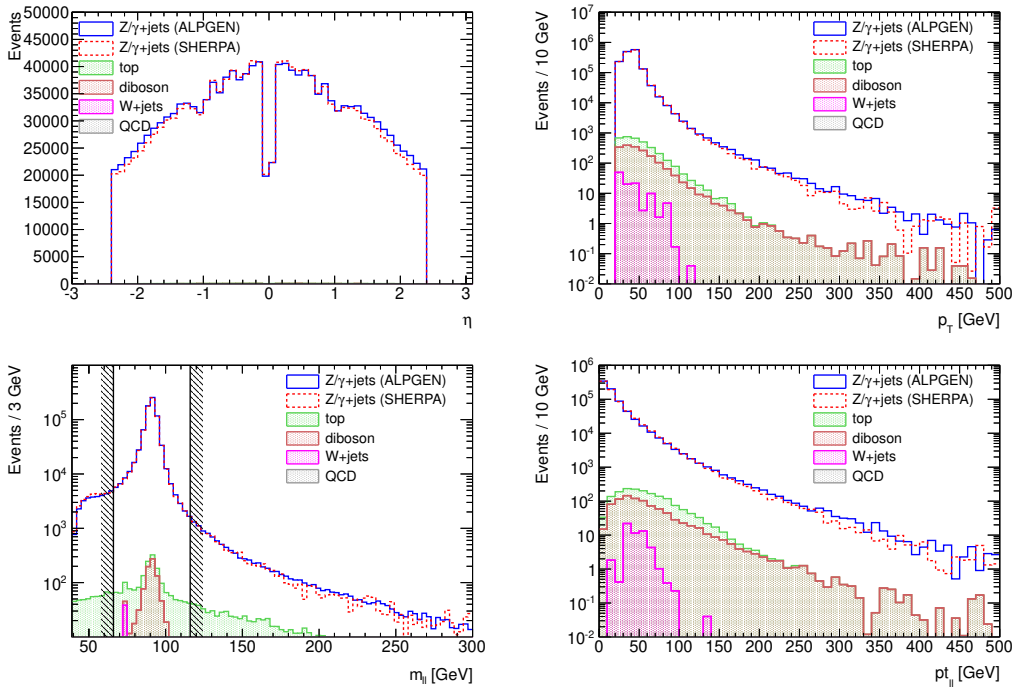

Figure 7.2: Distributions of η and p_T for preselected muons. Dimuon mass and p_T are shown on the bottom row. A Z boson mass window cut is made on the dielectron mass, indicated by the hashed bands. Events outside this region are shown for reference only and are not used.

7.2 Signal Region Definition

Three signal regions are used to maximize sensitivity for a wide range of graviton masses. Since the Z bosons in a graviton signal are expected to have high p_T, a cut is made on the p_T of the preselected leptonic Z boson. A high p_T hadronic Z boson is also required. As a result, this search is not sensitive to gravitons with a mass below 350 GeV.

For graviton masses greater than about 1 TeV, the p_T of the hadronic Z boson can be larger than 400 GeV and the separation of the decay products $\Delta R(q, q)$ less than 0.4. In this case, a single 'merged' jet is reconstructed, which typically has high mass. In the **Merged jet** signal region, the leading jet is required to have $m_j > 65$ GeV, which also considerably reduces the background from Z+jets events. The leading high-mass jet is required to have $p_T > 200$ GeV in order to be consistent with a hadronic Z boson decay. The p_T of the dilepton system is also required to be greater than 200 GeV.

The leading jet mass distribution above 30 GeV was found to be well described by an exponential, plus a Gaussian for the merged jet component. The width of the Gaussian approximates the jet mass resolution. It was measured to be 7.7 ± 0.4, 7.8 ± 0.4 and 8.3 ± 0.3 GeV for mass points 1, 1.25 and 1.5 TeV respectively, with a peak of 87 ± 1 GeV. The chosen cut is more than 2σ away from this peak to maintain a high signal efficiency.

For lower graviton masses, the p_T of the hadronic Z boson is generally low enough that two jets from its decay can be resolved. The mass of the two leading jets is required to be consistent with a Z boson: in the range $65 < m_{jj} < 115$ GeV. Two **Resolved jets** signal regions are defined. To maximize sensitivity to graviton masses of 500 GeV and above (**High Mass signal** region), the transverse momentum of the dijet system p_T^{jj} is required to be greater than 200 GeV. Again, the dilepton p_T is also required to be greater than 200 GeV. To preserve sensitivity to lower graviton masses, a third signal region is used with relaxed cuts on the p_T of the reconstructed Z bosons: $p_T^{jj} > 50$ GeV and $p_T^{\ell\ell} > 50$ GeV (**Low Mass signal** region). The **Merged jet** region and **High Mass signal** region are used simultane-

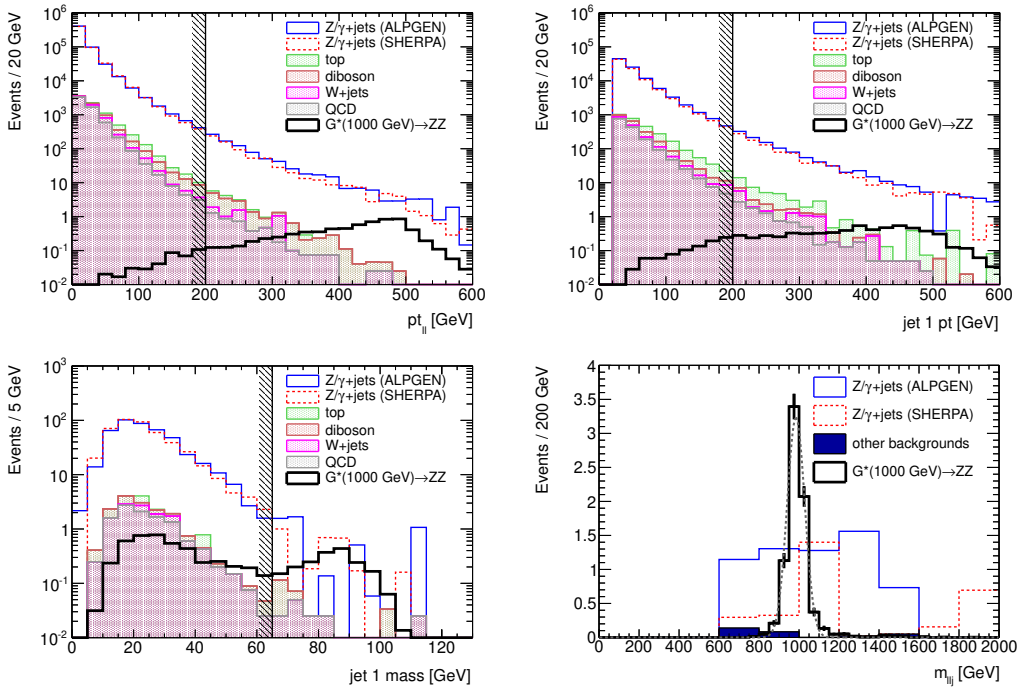

Figure 7.3: Definition for the **Merged jet** region. Distributions of the dilepton p_T and the dijet p_T after preselection cuts are shown. The leading dijet mass and three body mass $m_{\ell\ell j}$ are shown after cuts. Distributions for a graviton with mass of 1 TeV are shown. The $m_{\ell\ell j}$ distribution of the signal (bin width 50 GeV) is well described by a Gaussian fit. All distributions are normalized to 2 fb^{-1}.

ously for high masses. Events in the **Merged jet** region are removed from the **High Mass signal** region. This preserves the statistical independence of the two regions so that the results can be combined easily. The cuts used to define the three signal regions, and the range of graviton masses over which they are used, are summarized in Table 7.1.

Figures 7.3 – 7.5 show distributions for the variables used to define each of the signal regions, for SM background and a graviton signal. All samples are normalized to an integrated luminosity of 2 fb^{-1}. The transverse momenta of the dilepton ($p_T^{\ell\ell}$) and dijet (p_T^{jj}) systems after the preselection cuts are shown. The dijet mass is shown after cuts on $p_T^{\ell\ell}$ and p_T^{jj}. Finally, the reconstructed graviton mass is shown after all cuts. This is either a three body mass $m_{\ell\ell j}$ in the Merged jet region, or the

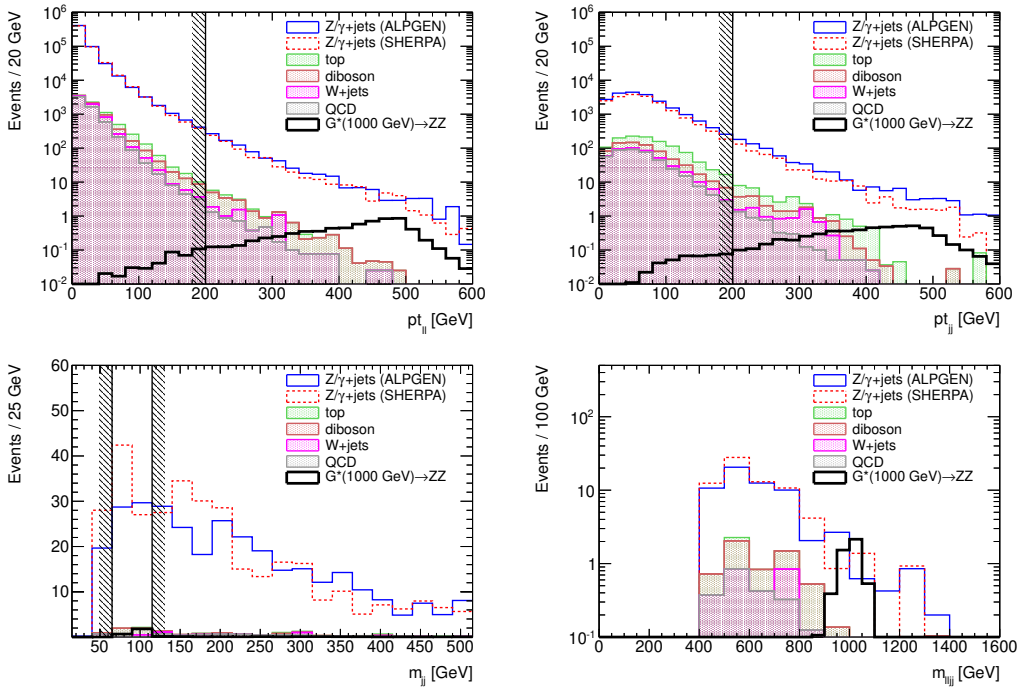

Figure 7.4: Definition for the **Resolved jets (High Mass signal)** region. Distributions of the dilepton p_T and the dijet p_T after preselection cuts are shown. The dijet mass and four body mass $m_{\ell\ell jj}$ are shown after cuts. Distributions for a graviton with mass of 1 TeV are shown. All distributions are normalized to 2 fb^{-1}.

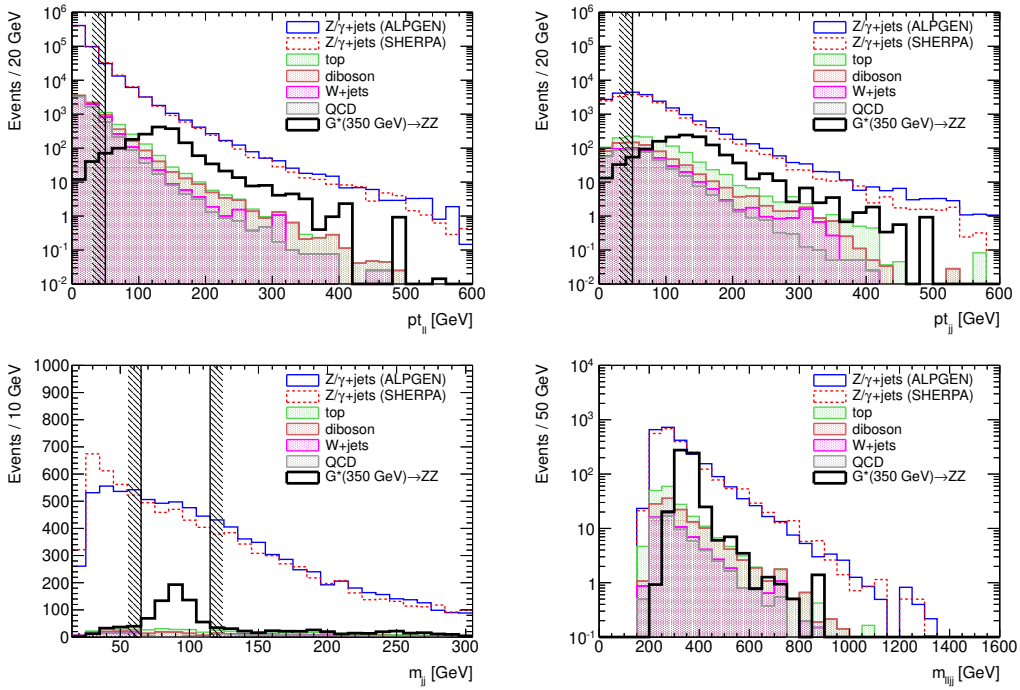

Figure 7.5: Definition for the **Resolved jets (Low Mass signal)** region. Distributions of the dilepton p_T and the dijet p_T after preselection cuts are shown. The dijet mass and four body mass $m_{\ell\ell jj}$ are shown after cuts. Distributions for a graviton with mass of 350 GeV are shown. All distributions are normalized to 2 fb^{-1}.

	Signal region
Merged jet	$m_j > 65$ GeV,
$m_{G^*} \geq 750$ GeV	$p_T^j > 200$ GeV,
	$p_T^{\ell\ell} > 200$ GeV.
Resolved jets	$65 < m_{jj} < 115$ GeV,
(High Mass signal)	$p_T^{jj} > 200$ GeV,
$m_{G^*} \geq 500$ GeV	$p_T^{\ell\ell} > 200$ GeV,
	veto events in **Merged jet** region.
Resolved jets	$65 < m_{jj} < 115$ GeV,
(Low Mass signal)	$p_T^{jj} > 50$ GeV,
$m_{G^*} < 500$ GeV	$p_T^{\ell\ell} > 50$ GeV.

Table 7.1: Summary of signal region selections. The range of graviton masses m_{G^*} over which the signal regions are used is shown. The **Merged jet** and **High Mass signal** regions are used simultaneously for high masses. The veto preserves the statistical independence of the two regions so that the results can be combined easily.

	Control region
Merged jet	$m_j < 65$ GeV,
	$p_T^j > 200$ GeV,
	$p_T^{\ell\ell} > 200$ GeV.
Resolved jets	$[m_{jj} < 65$ GeV or $m_{jj} > 115$ GeV],
(High Mass signal)	$p_T^{jj} > 200$ GeV,
	$p_T^{\ell\ell} > 200$ GeV,
	veto events in **Merged jet** region.
Resolved jets	$[m_{jj} < 65$ GeV or $m_{jj} > 115$ GeV],
(Low Mass signal)	$p_T^{jj} > 50$ GeV,
	$p_T^{\ell\ell} > 50$ GeV.

Table 7.2: Summary of control region selections used to normalize Z+jets background and estimate uncertainties.

four body mass $m_{\ell\ell jj}$ in the Resolved jets regions.

7.3 Control Region Definitions

One control region is chosen for each signal region by inverting the jet (dijet) mass cut in the Merged (Resolved) jets signal region. The cuts used to define the control regions are summarized in Table 7.2.

Each control region is used to determine the normalization of the dominant Z+jets background in the corresponding signal region. The Z+jets prediction is scaled to match the data in the control region. The control regions are also used to check the shape of the Z+jets distributions and to estimate the systematic uncertainties.

m_{G^*}	Mass Resolution [GeV]	
[GeV]	$\ell\ell j$	$\ell\ell jj$
500	34 ± 6	17 ± 1
750	31 ± 1	26 ± 1
1000	40 ± 1	31 ± 3
1250	42 ± 1	37 ± 5
1500	51 ± 1	–

Table 7.3: Resolution of the reconstructed graviton mass in the RS1 model. Resolutions in the Merged jet and Resolved jets signal regions are shown. The mass peaks are well-modeled by Gaussian distributions. The σ of the Gaussian fit is shown.

7.4 Signal Characterization

7.4.1 Mass Resolution

The resolution on the reconstructed graviton mass is mainly determined by the jet energy resolution and jet mass resolution, since the RS1 graviton is a narrow resonance. Both the $m_{\ell\ell j}$ and $m_{\ell\ell jj}$ distributions are well modeled by Gaussian distributions, with small non-Gaussian tails. The resolution on $m_{\ell\ell j}$ and $m_{\ell\ell jj}$ is shown in Table 7.3. The absolute value of the mass resolution increases with the mass, as expected since the absolute value of the jet energy resolution increases with the energy. The resolution is around 20% better if the jets can be resolved. The resolution is a few percent better in the electron channel than in the muon channel.

The graviton in the bulk RS model tends to be wider than in the RS1 model such that the intrinsic width is a large part of the reconstructed width. The mass resolution of truth and reconstructed particles is shown in Table 7.4.

7.4.2 Acceptance

The signal acceptance is calculated as the fraction of graviton events in the signal regions as a function of signal mass. The acceptance in the RS1 model is shown in

m_{G^*}	Mass Resolution [GeV]	
[GeV]	Reco.	True
500	25 ± 1	19 ± 1
600	35 ± 1	27 ± 1
700	39 ± 1	35 ± 1
800	45 ± 1	42 ± 1
900	53 ± 2	50 ± 2

Table 7.4: Resolution of the graviton mass in the bulk RS model. Only the Resolved jets signal region is used. Resolutions using truth particles and using full reconstruction are shown. The mass peaks are well-modeled by Gaussian distributions. The σ of the Gaussian fit is shown.

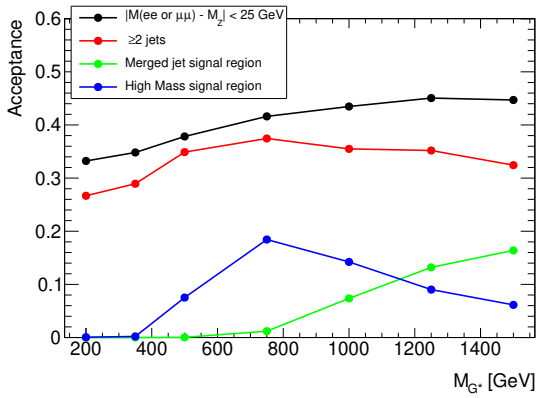

Figure 7.6: Acceptance for graviton signal points after preselection and signal selection cuts described in the text. One Z boson decays to electrons, muons or taus and the other decays hadronically. The acceptance represents the fraction of these events that pass the cuts specified.

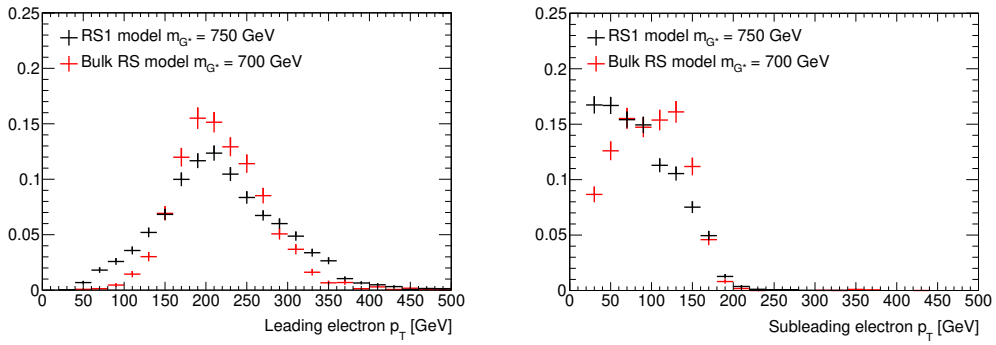

(a) Leading electron p_T **(b)** Subleading electron p_T

Figure 7.7: The p_T of reconstructed electrons from the decay of the Z boson in the two signal models. The p_T of the subleading electron is higher in the bulk RS model which contributes significantly to the larger acceptance.

Figure 7.6 as a fraction of events where one Z boson decays to electrons, muons or taus and the other decays hadronically.

About 40 – 45% events have a well reconstructed Z boson. Over 90% of these events have at least two jets for $500 < m_{G^*} < 750$ GeV. The acceptance in the Resolved jets (High Mass signal) region is as high as 20% for a 750 GeV signal. For higher masses, jet merging is important and a large fraction of high mass jets appear.

In the bulk RS model, longitudinally polarized Z bosons decay to leptons with a smaller difference in p_T which means that the subleading electron p_T is higher than in the RS1 model as shown in Figure 7.7. As a result, the acceptance, shown in Table 7.5 is almost twice as high as in the RS1 model.

m_{G^*} [GeV]	Acceptance
500	$21.6 \pm 0.2\%$
600	$35.5 \pm 0.1\%$
700	$40.5 \pm 0.1\%$
800	$39.6 \pm 0.1\%$
900	$34.7 \pm 0.1\%$

Table 7.5: Resolution of the graviton mass in the bulk RS model. Only the Resolved jets signal region is used. Resolutions using truth particles and using full reconstruction are shown. The mass peaks are well-modeled by Gaussian distributions. The σ of the Gaussian fit is shown.

Chapter 8

Background Estimation

With the dilepton mass required to be consistent with a Z boson, and one or two jets selected, Z+jets production is by far the dominant background among SM processes. In the Low Mass signal region, there are contributions of a few percent from top quark and diboson production. W+jets and multijet production are the smallest backgrounds. After requiring $p_T^{\ell\ell} > 200$ GeV, the top production background is significantly reduced. In the Merged jet region, multijet production represents a few percent of the background in the electron channel.

For the dominant Z+jets background, a semi-data-driven background estimate is used: MC is normalized using scale factors derived from control regions. Top quark, diboson and W+jets backgrounds are estimated with MC scaled to the cross section times luminosity. The cross sections and MC generators used are described in Chapter 5. The multijet background is modeled in a data-driven way. Each background is described in the sections to follow. Preselected events are shown in Figures 8.1 – 8.4. The number of electrons at low η is underestimated. SHERPA underestimates the number of jets by about 10%. ALPGEN overestimates p_T^j and p_T^{jj} in the high p_T region.

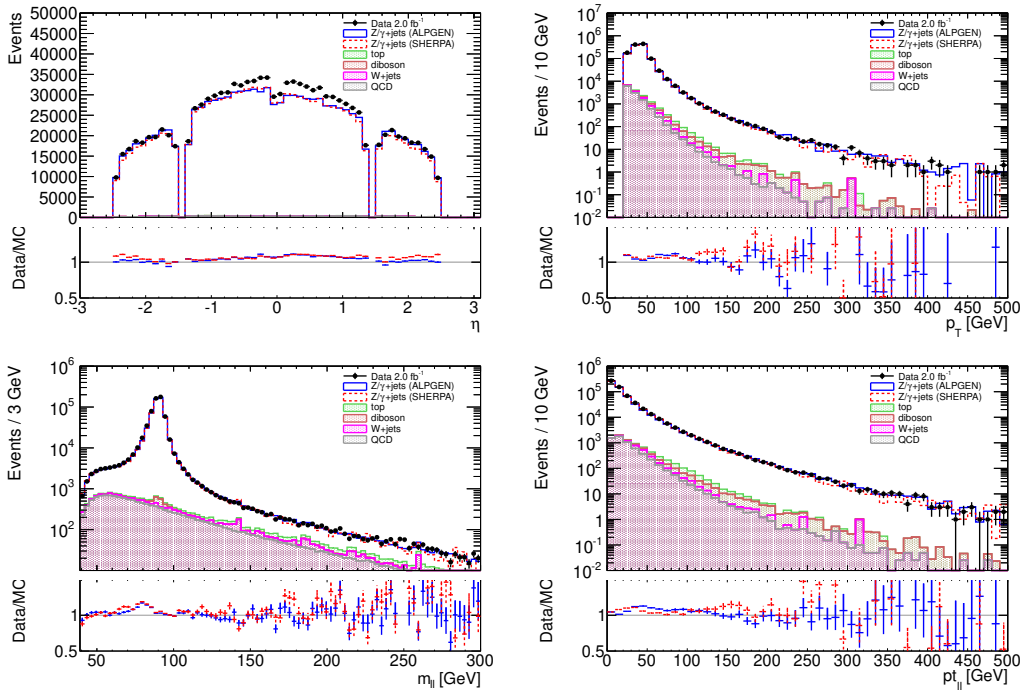

Figure 8.1: Electron channel after preselections: distributions of η and p_T are shown on the top row. Dielectron mass and p_T are shown on the bottom row.

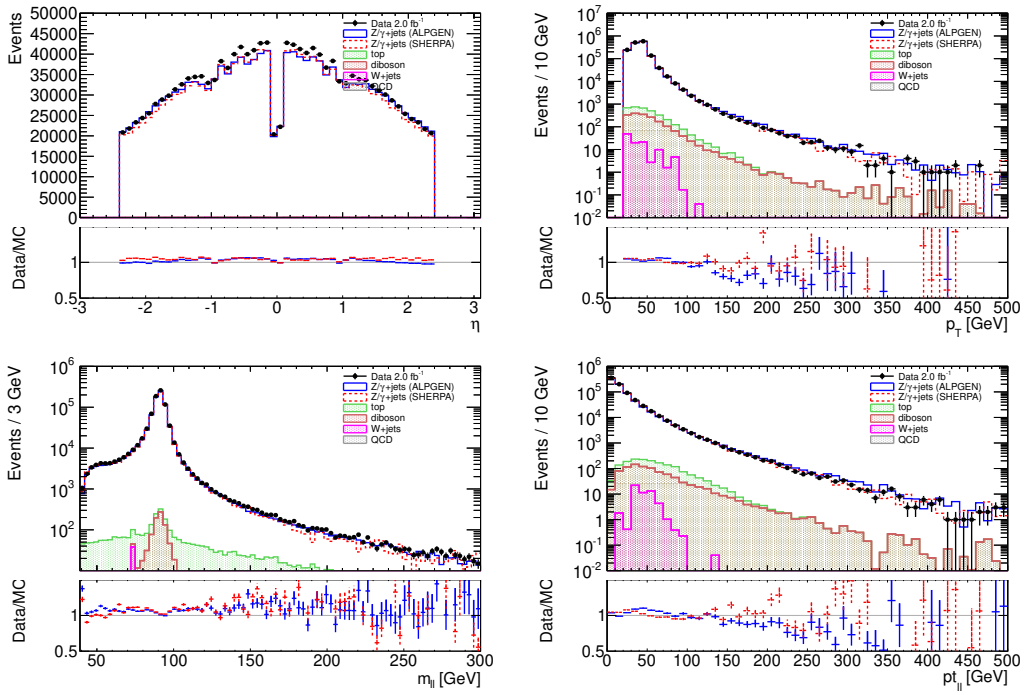

Figure 8.2: Muon channel after preselections: distributions of η and p_T are shown on the top row. Dimuon mass and p_T are shown on the bottom row. The high dilepton mass region is shown for reference only; these events are not used in this thesis.

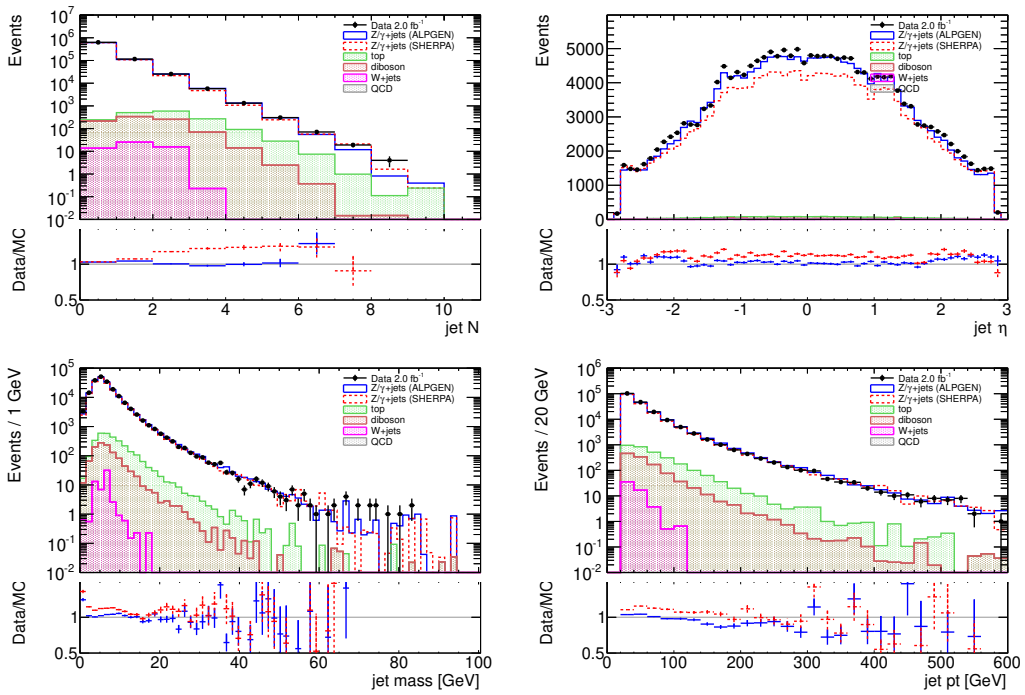

Figure 8.3: Preselected jets (Muon channel only). Distributions of N_{jets} and jet η are shown on the top row. Jet mass and p_T are shown on the bottom row.

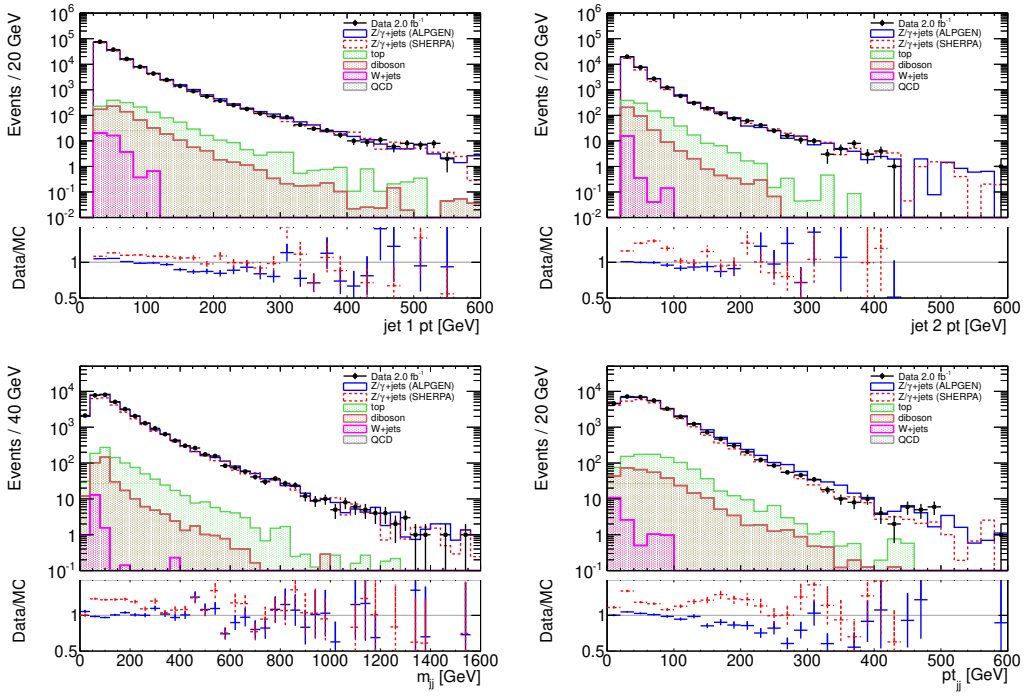

Figure 8.4: Dijet variables in preselected events (Muon channel only). The leading and sub-leading jet p_T is shown on the top row. These two jets are combined to give the dijet mass and p_T shown on the bottom row.

8.1 Z+jets Background

The Z+jets background is estimated using ALPGEN MC samples scaled to the data in control regions. In the preselected events, an excess in electrons in the low eta region is seen. Disagreement in p_T^j and p_T^{jj} is also seen. ALPGEN overestimates the number of events with jet $p_T \gtrsim 150$ GeV and dijet $p_T \gtrsim 150$ GeV, shown in Figure 8.4. After making cuts on dilepton and dijet p_T, the disagreement between data and MC can be as high as 30%. SHERPA samples underestimate the number of jets by about 10%. They are also scaled to the data in the control region and used to estimate the systematic uncertainty.

8.1.1 Scale Factors

The scale factor in each region is calculated from the number of events observed in data, the expected Z+jets background and the expected non-Z+jets backgrounds (top, diboson, W+jets and multijet): $R = (N^{\text{Data}} - N^{\text{MC}}_{\text{other}})/N^{\text{MC}}_{Z+\text{jets}}$. Scale factors for ALPGEN and SHERPA Z+jets samples for each control region are shown in Table 8.1. After these scale factor are applied, the ALPGEN sample is used as a central value for the Z+jets background estimate.

Control Region	Z+jets MC	Electron Channel	Muon Channel
Merged jet	ALPGEN	0.83 ± 0.04	0.78 ± 0.03
	SHERPA	1.03 ± 0.06	0.95 ± 0.05
Resolved jets	ALPGEN	0.84 ± 0.08	0.74 ± 0.09
High Mass	SHERPA	1.34 ± 0.12	1.20 ± 0.16
Resolved jets	ALPGEN	1.00 ± 0.02	0.96 ± 0.02
Low Mass	SHERPA	1.17 ± 0.02	1.11 ± 0.02

Table 8.1: Z+jets scale factors are determined from the control regions. Note that a scale factor less than one corresponds to MC overestimating the data. The uncertainties are statistical only.

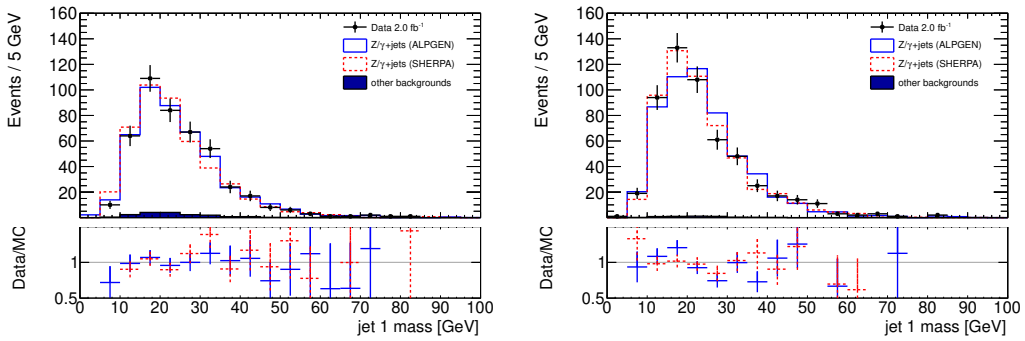

(a) Merged jet region

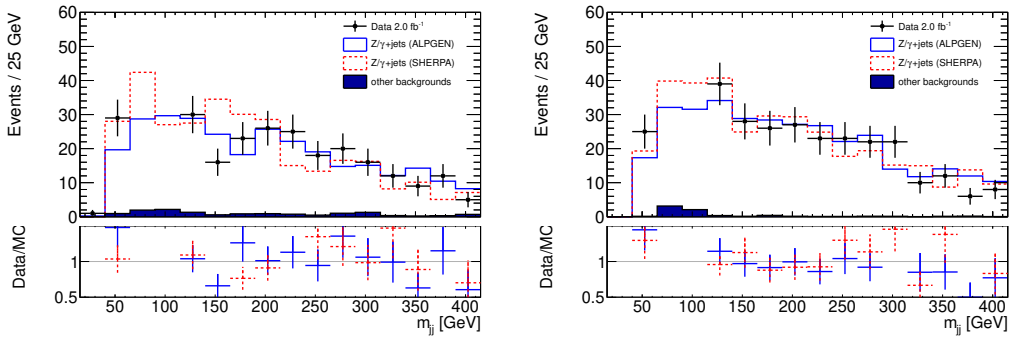

(b) Resolved jets (High Mass region)

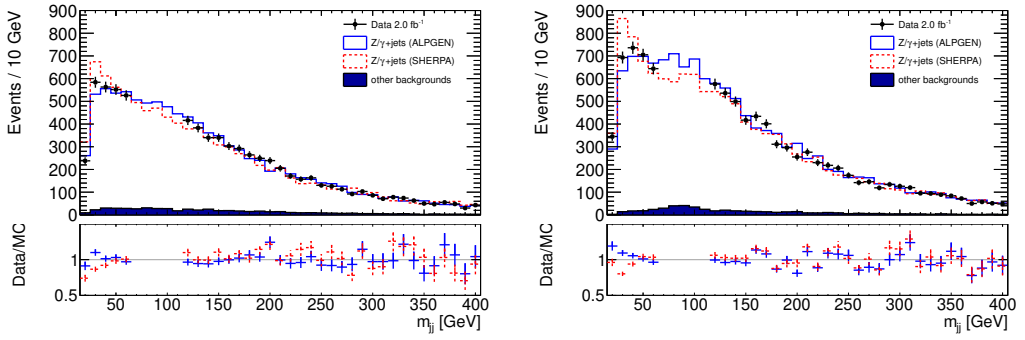

(c) Resolved jets (Low Mass Region)

Figure 8.5: Jet (dijet) mass in the Merged (Resolved) jet regions. Scale factors have been applied. Data is blinded in the signal regions.

8.1.2 Systematic Uncertainties

Systematic uncertainties on both the overall normalization and shape of the Z+jets background are estimated. Discrepancies between MC generators and between MC and data are considered, as well as contributions from MC statistics and heavy flavor composition. Approximate values are summarized at the end of the section in Table 8.5. Systematic uncertainties on the measurement of objects, described in Chapter 6, are also significant.

Overall Normalization In the Resolved jets control regions, the scale factors are calculated separately in the two m_{jj} sidebands ($m_{jj} < 65$ GeV and $m_{jj} > 115$ GeV); these are listed in Table 8.2. The uncertainty is taken as the maximum difference between the scale factor calculated in each sideband and in both sidebands taken together. Very few events fall in the low m_{jj} sideband of the High Mass control region, after a p_T^{jj} cut of 200 GeV. The full difference between the data and unscaled ALPGEN MC in the High Mass control region as a function of $m_{\ell\ell jj}$ is taken as an uncertainty. In other words, this is a 100% uncertainty on the deviation of the scale factors from one. This 100% uncertainty is also used for the Merged jet region.

Control Region	Z+jets MC	m_{jj} Range [GeV]	Electron Channel	Muon Channel
Low Mass	ALPGEN	$m_{jj} < 65$	0.96 ± 0.04	0.92 ± 0.04
	ALPGEN	$m_{jj} > 115$	0.95 ± 0.03	0.88 ± 0.02
High Mass	ALPGEN	$m_{jj} < 65$	1.65 ± 0.77	1.12 ± 0.75
	ALPGEN	$m_{jj} > 115$	0.69 ± 0.11	0.73 ± 0.12

Table 8.2: Z+jets scale factors determined in the lower and higher m_{jj} sideband regions for the Low and High Mass control regions. Due to the large statistical uncertainty on the low m_{jj} sideband in the High Mass region, these values are not used. The uncertainties are statistical only.

In the ALPGEN Z+jets sample, heavy flavor jets ($Z + b\bar{b}$) are simulated with parton shower only. This may underestimate the total contribution. In a separate ALPGEN sample, with $Z + b\bar{b}$ jets are produced in the matrix element; this is used

to estimate the systematic uncertainty. The sum of the two samples is likely to overestimate heavy flavor contribution since the parton-shower contribution will be double counted. The contribution to the uncertainty, given by the variation in the scale factor after including the $b\bar{b}$ sample, is 6%.

The MC statistics in the high p_T regions is especially limited as shown in Table 8.3. This is a significant contribution to the uncertainty on the background normalization.

Signal Region	Electron Channel	Muon Channel
Merged jet	16.9%	16.2%
Resolved jets (High Mass)	4.9%	4.8%
Resolved jets (Low Mass)	1.1%	1.0%

Table 8.3: Uncertainty on the expected event yields in the signal regions due to limited MC statistics.

Reconstructed Mass Shape Although ALPGEN and SHERPA are both normalized to data in the control region, differences in the m_j and m_{jj} distributions result in significantly different event yields in the signal regions, as shown in Figure 8.6. Table 8.4 shows the fractional difference between ALPGEN and SHERPA event yields after applying scale factors. The shape is also cross checked with the shape of the four body mass in the Resolved jets control regions, shown in Figure 8.7.

Signal Region	Electron Channel	Muon Channel
Merged jet	$43 \pm 11\%$	$85 \pm 20\%$
Resolved jets (High Mass)	$17 \pm 1\%$	$26 \pm 2\%$
Resolved jets (Low Mass)	$7.5 \pm 0.1\%$	$11.4 \pm 0.2\%$

Table 8.4: Fractional difference between ALPGEN and SHERPA event yields in the signal regions: |ALPGEN − SHERPA|/ALPGEN.

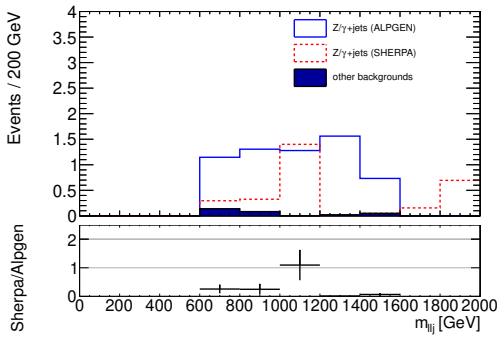

(a) Merged jet region

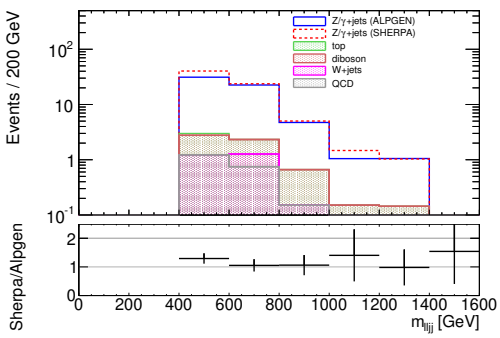

(b) Resolved jets (High Mass signal)

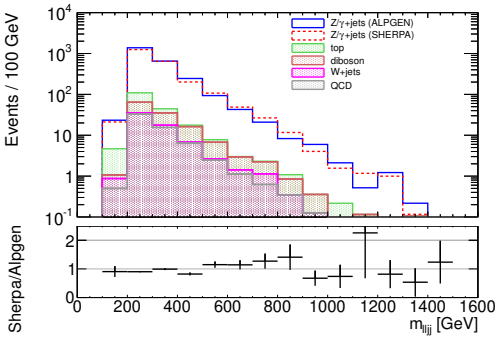

(c) Resolved jets (Low Mass signal)

Figure 8.6: The ratio of SHERPA to ALPGEN in the reconstructed mass distributions in the signal regions. Scale factors derived in the control regions have been applied. The deviation from one is used as the uncertainty on the shape of the Z+jets background.

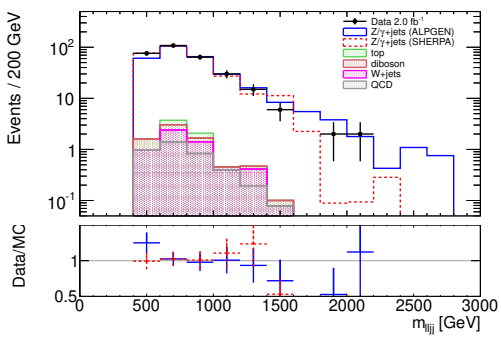

(a) High Mass control region (Electron channel)

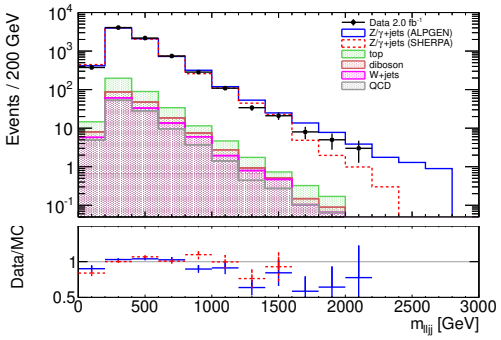

(b) Low Mass control region (Electron channel)

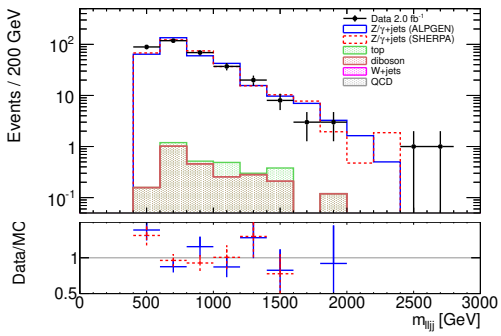

(c) High Mass control region (Muon channel)

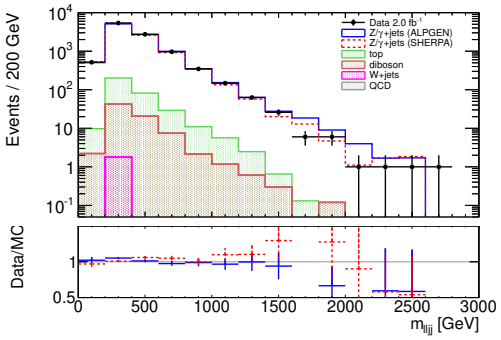

(d) Low Mass control region (Muon channel)

Figure 8.7: Four body mass distribution in the Resolved jets control regions

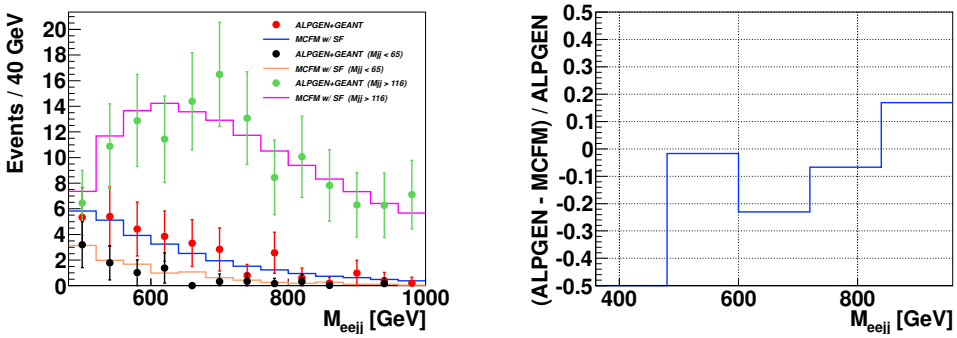

Figure 8.8: Comparison of MCFM and ALPGEN in the High Mass region.
Left: The four body mass m_{eejj} distributions in the High Mass region. The upper line corresponds to the high m_{jj} sideband; the lower line corresponds to the low m_{jj} sideband and the middle line to the signal region. Expected yields from MCFM (lines) are scaled to match the total ALPGEN (points) yields in the two sidebands. A weighted average scale factor is used for the signal region.
Right: The relative difference between MCFM and ALPGEN in the signal region.

The reconstructed mass shape in the High Mass region was cross-checked by comparing ALPGEN to the NLO prediction using MCFM. Three $m_{\ell\ell jj}$ distributions were computed: for the low m_{jj} sideband, the high m_{jj} sideband, and the signal region. The MCFM distribution in each sideband is normalized to the corresponding ALPGEN yield. The weighted average of MCFM scaling factors in the two sidebands is used to predict the MCFM event yield in the signal region.

The MCFM prediction in the signal region was found to be 28.5 ± 5.3 events per fb^{-1} compared to the ALPGEN yield of 34.1 ± 5.8 events. The difference between the MCFM and ALPGEN predictions varies at most by 20% between $450 < m_{\ell\ell jj} < 1000$ GeV as seen in Figure 8.8. No additional uncertainty is applied to the shape of the Z+jets distribution since this variation should be covered by the ALPGEN/SHERPA difference.

		Resolved jets	
Systematic effect	Merged jet	High Mass	Low Mass
Normalization:			
m_{jj} sidebands	–	–	5 – 15%
ALPGEN/Data	10 – 20%	15 – 30%	–
MC statistics	20%	5%	1%
Heavy Flavor	6%	6%	6%
Shape:			
ALPGEN/SHERPA	40 – 85%	15 – 25%	7 – 11%

Table 8.5: Summary of fractional uncertainties on the Z+jets scale factors in the various signal regions. The fractional uncertainty on the signal region yield, due to the difference between ALPGEN and SHERPA is given. However, this uncertainty may vary as a function of the reconstructed mass.

8.2 Other Backgrounds

8.2.1 Top

The top quark background is mostly due to $t\bar{t}$ production with a few percent from single top, which includes tb, tqb, and tW processes. Estimates for all processes use the MC@NLO generator normalized by cross section. The cross sections used and their theoretical uncertainties are listed in Chapter 5.

Systematic uncertainties are estimated using alternative $t\bar{t}$ MC samples produced using a variety different of generators and parameter settings. Table 8.6 lists the generators, cross sections and sources of uncertainty. No significant shape difference is seen with respect to the nominal sample. The maximum difference between the nominal MC@NLO and the two POWHEG samples (20%) is symmetrized. An estimate of the ISR/FSR effect is given by the symmetrized maximum difference between the nominal sample and the two ACERMC samples. These two uncertainties are added in quadrature to give a total uncertainty on the top quark background of 25%.

Generator	Dataset ID	$\sigma \times B \times \varepsilon_{\text{filter}}$	Purpose
MC@NLO+Jimmy	105200	89.02	Nominal $t\bar{t}$ Sample
Powheg+Jimmy	105860	89.41	Generator
Powheg+Pythia	105861	89.41	Generator, Hadronization
AcerMC	117259	89.09	Increased ISR
AcerMC	117260	89.09	Decreased ISR

Table 8.6: Nominal and systematic $t\bar{t}$ MC samples used in the analysis for systematic uncertainties on the acceptance due to generator difference, hadronization and initial/final state radiation effects.

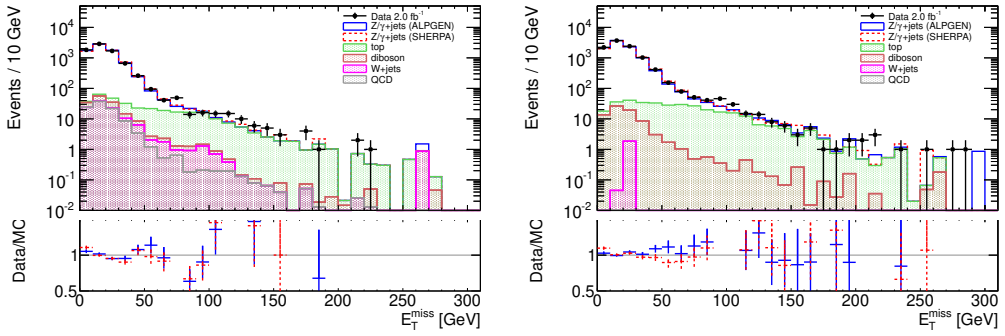

(a) Electron channel **(b)** Muon channel

Figure 8.9: Comparison of the data and the background prediction for the $E_{\mathrm{T}}^{\mathrm{miss}}$ distribution in the Low Mass control region.

The top MC normalization is also checked with the data in a top-dominated high $p_T^{\ell\ell}$ control region. Figure 8.9 shows the $E_{\mathrm{T}}^{\mathrm{miss}}$ distribution for the data and MC simulations in the Low Mass control region. Top dominates in the high $E_{\mathrm{T}}^{\mathrm{miss}}$ region. The top fraction for $E_{\mathrm{T}}^{\mathrm{miss}} > 80$ GeV is about 70%, event yields are shown in Table 8.7. The MC predicts 220 ± 40 events with top normalization uncertainty only while the observed number of events is 275. This is at the limit of consistency with the expectation.

Sample	Electron Channel	Muon Channel	Combined
Z+jets	9.7	44.0	53.6
Top	66.4	93.3	159.6
Diboson	1.0	2.9	3.9
W+jets	3.4	0.0	3.4
Multijet	2.4	0.0	2.4
Sum of Backgrounds	82.8	140.1	222.8
Data	94	181	275

Table 8.7: Event yields in the top-dominated high $p_T^{\ell\ell}$ control region.

8.2.2 Diboson

The diboson background is estimated with MC simulations normalized by cross section. Recent ATLAS measurements [121, 122, 123] used NLO diboson cross sections with systematic uncertainties of about 5% at accuracy. These values are used and 5% is taken as the diboson background systematic uncertainty.

8.2.3 W+jets

The W+jets background is also estimated with MC simulations normalized by cross section. The contribution from W+jets is small after requiring two leptons with Z boson mass. The W+jets cross section measurement [142] reports the systematic uncertainty on the $W+ \geq 2$jet cross section to be about 20% for both electron and muon channels. One jet would have to fake a lepton in order for these events to pass our selections. The jet-faking-leptons rate has been measured in data. The maximum difference between data and MC is given as 20% with little dependence on jet p_T. A systematic uncertainty of 20% is added linearly to the $W+ \geq 2$ jets uncertainty giving a total W+jets background uncertainty of 40%. This has a small impact on the total background uncertainty due to the small fraction of W+jets background.

8.2.4 Multijets

Multijet events with two fake leptons represent a significant background despite several effective cuts to reject fake leptons described in Chapter 6. The cross section for multijet events is vastly greater than the Z production cross section. It is difficult to model the tails of the QCD background, for example the rate of the very most electron-like jets or the extremes of the dijet p_T distribution. The multijet background is therefore estimated with a data-driven method. Kinematic multijet distributions are taken from a multijet dominated region. These 'template' distributions are then scaled to match the data in the required region.

In the electron channel, a control sample is selected with two loose electrons which both fail the medium quality requirement. These electrons are not required to pass the isolation requirement. This sample is mostly composed of multijet events, although there are small contributions from heavy flavor production. In particular it contains a negligible fraction of Z events as can be seen by the absence of a peak around 91 GeV in the m_{ee} distribution in Figure 8.10. Multijet events that pass the medium quality and isolation requirements are likely to include a larger contribution from heavy flavor. However, the distributions of kinematic variables are assumed to be the same. The data-derived multijet template and an MC-derived non-multijet template are combined to fit the m_{ee} distribution in data. A fitting algorithm adjusts the relative normalization of the two templates to best match the data.

Figure 8.10 shows the fitted fraction of multijet events in the m_{ee} distribution for preselected events. The multijet background is estimated to be about $2.5 \pm 0.1\%$ before the Z mass window cut and about $1.0 \pm 0.1\%$ after it.

The systematic uncertainty on the multijet background normalization is estimated from a separate fit to the $m_{\ell\ell}$ distribution after requiring two jets. The multijet background fraction in this fit is $4.8 \pm 0.6\%$ before the Z mass window cut. A 100% uncertainty is therefore assigned to the multijet background estimate. This has a small impact on the total background uncertainty due to the small fraction of multijet background.

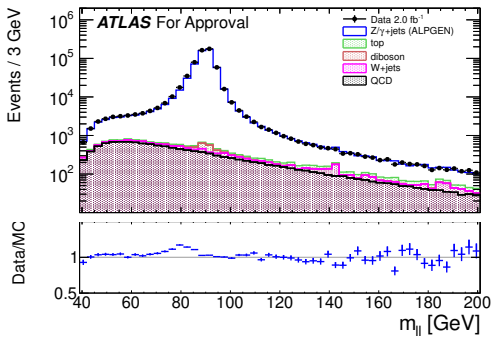

Figure 8.10: Dielectron mass distribution from the data. A data-derived multijet background template with the loose-but-not-medium criteria and an MC-derived non-multijet background template are used. The normalization is determined by a fitting algorithm.

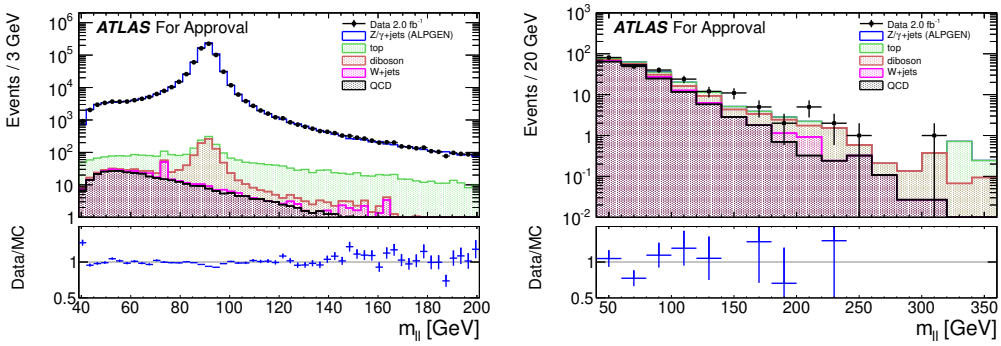

(a) Opposite-sign dimuon mass. **(b)** Same-sign dimuon mass.

Figure 8.11: Dimuon mass distributions from the data., A data-derived multijet background template with non-isolated muons and a MC-derived non-multijet background template is used. The same-sign dimuon distribution is used to set the normalization.

In the muon channel, the shape is taken from a sample of events with two non-isolated muons. This sample is expected to be dominated by heavy flavor production and K or π decays. There will be a contribution from fake muons from jets that punch through the calorimeter [143]. The normalization is estimated using a sample of same-sign dimuon events. The contribution from heavy flavor production in the same-sign sample in particular will be reduced since muon charge misidentification is negligible. After applying the Z boson mass window cut, the multijet background is less than 0.1%. It is therefore neglected in the rest of this analysis.

8.3 Signal Region Data

Process	Merged jet signal region yield (Electron and muon channel)
Backgrounds:	
Z+jets	$13 \pm 2 \,^{+15}_{-11}$
Other Backgrounds	$0.5 \pm 0.03 \pm 0.3$
Sum:	$13 \pm 2 \,^{+15}_{-11}$
Data:	12
Signals:	
$G^* \to ZZ$, $m_{G^*} = 750$ GeV	$2.8 \pm 0.1 \pm 1.0$
$G^* \to ZZ$, $m_{G^*} = 1000$ GeV	$3.8 \pm 0.1 \pm 0.6$
$G^* \to ZZ$, $m_{G^*} = 1250$ GeV	$1.8 \pm 0.02 \,^{+0.2}_{-0.3}$

Table 8.8: Event yields in the Merged jet signal region. The first uncertainty is statistical, the second is systematic.

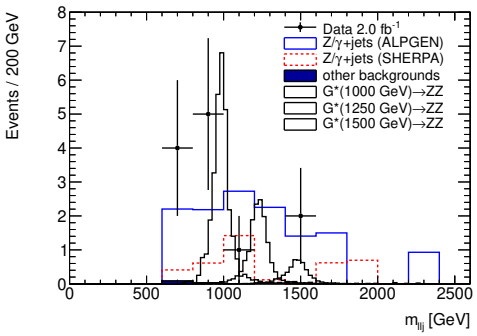

Figure 8.12: Reconstructed graviton mass distribution in the Merged jet region (Electron and muon channels combined).

Process	High Mass signal region yield (Electron and muon channel)
Backgrounds:	
Z+jets	$105 \pm 23 \,^{+\,26}_{-\,27}$
Top	$0.2 \pm 0.2 \pm 0.1$
Diboson	$8 \pm 0.4 \,^{+\,0.9}_{-\,0.5}$
W+jets	$0.5 \pm 0.5 \pm 0.2$
Multijet	$2 \pm 0.3 \pm 2$
Sum:	$116 \pm 23 \,^{+\,29}_{-\,30}$
Data:	157
Signals:	
$G^* \to ZZ$, $m_{G^*} = 500$ GeV	$131 \pm 2 \pm 13$
$G^* \to ZZ$, $m_{G^*} = 750$ GeV	$35 \pm 1 \pm 2$
$G^* \to ZZ$, $m_{G^*} = 1000$ GeV	$5.1 \pm 0.1 \,^{+\,0.4}_{-\,0.3}$
$G^* \to ZZ$, $m_{G^*} = 1250$ GeV	$0.78 \pm 0.01 \,^{+\,0.06}_{-\,0.05}$

Table 8.9: Event yields in the Resolved jets High mass signal region. The first uncertainty is statistical, the second is systematic. Electron and muon channel systematic uncertainties are assumed to be fully correlated for the purposes of this table.

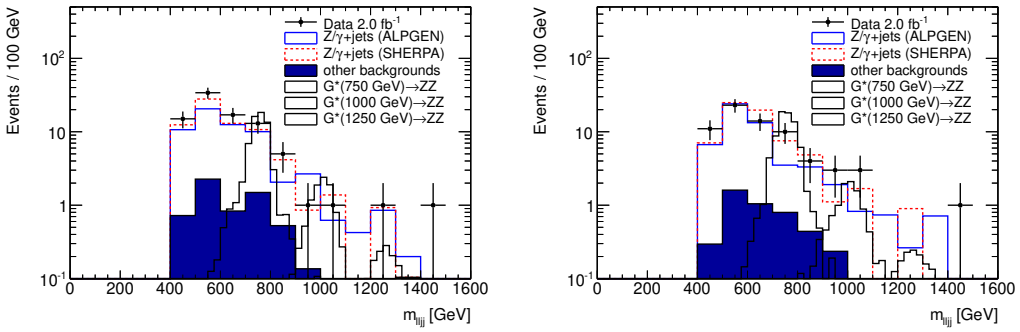

(a) Electron channel **(b)** Muon channel

Figure 8.13: Reconstructed graviton mass distribution in the Resolved jets High mass signal region.

Process	Low Mass signal region yield (Electron and muon channel)
Backgrounds:	
Z+jets	$5031 \pm 28 \,^{+\,805}_{-\,791}$
Top	$126 \pm 3 \,^{+\,21}_{-\,18}$
Diboson	$147 \pm 1 \,^{+\,16}_{-\,13}$
W+jets	$7 \pm 2 \pm 3$
Multijet	$60 \pm 3 \,^{+\,60}_{-\,60}$
Sum:	$5370 \pm 29 \,^{+\,906}_{-\,886}$
Data:	5616
Signals:	
$G^* \to ZZ$, $m_{G^*} = 350$ GeV	$1250 \pm 18 \,^{+\,84}_{-\,83}$

Table 8.10: Event yields in the Resolved jets Low mass signal region. The first uncertainty is statistical, the second is systematic. Electron and muon channel systematic uncertainties are assumed to be fully correlated for the purposes of this table.

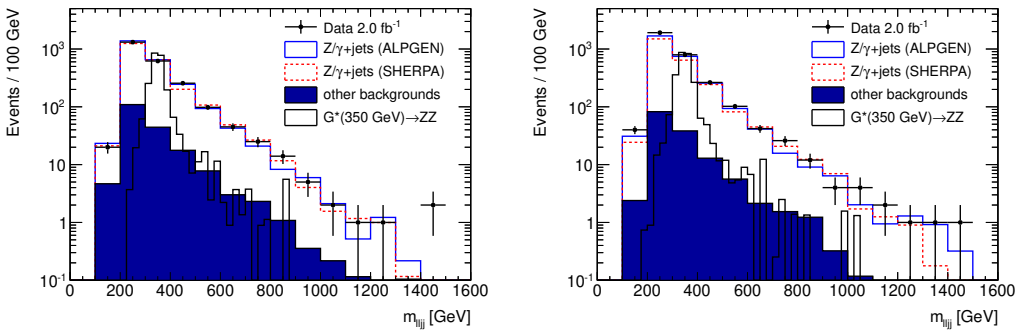

(a) Electron channel **(b)** Muon channel

Figure 8.14: Reconstructed graviton mass distribution in the Resolved jets Low mass signal region.

Chapter 9

Statistical Analysis

The degree to which the data is consistent with the background expectations is determined using the CL_s method [144, 145, 146]. The systematic and statistical uncertainties that affect the expected event yields must be combined. In the absence of a signal, confidence limits are set on the existence of a KK graviton decaying to ZZ. This chapter outlines the CL_s method, summarizes the systematic uncertainties included in this analysis and describes the procedure used for setting limits.

9.1 The CL_s Method

9.1.1 Log Likelihood Ratio

The log likelihood ratio (LLR) can be calculated for data observed in one (or many) bins in terms of the expected background yield(s) and the expected signal yield(s). The *likelihood* of an expected yield, given an observed number of events, is equal to the *probability* of observing that number of events, given that value of expected yield. The LLR is the logarithm of the ratio of two likelihoods: the likelihood of the signal+background yield $s + b$ and the likelihood of the background-only yield b. The ratio Λ is:

$$\Lambda(x) = \frac{\mathcal{L}(s+b|x)}{\mathcal{L}(b|x)}, \tag{9.1}$$

where x is the number of events observed in a single bin. The likelihood function $\mathcal{L}$, in this case, is a Poisson distribution, so the likelihood ratio can be expanded:

$$\Lambda(x) = \frac{(s+b)^x e^{-(s+b)}}{b^x e^{-b}}. \tag{9.2}$$

Multiple bins and orthogonal analysis channels can be easily accommodated. The combined likelihood is the product of the individual likelihoods of each bin in each channel. The likelihood ratio is then written as:

$$\Lambda(\mathbf{x}) = \prod_{i}^{\text{channels}} \prod_{j}^{\text{bins}} \frac{(s_{ij}+b_{ij})^{x_{ij}} e^{-(s_{ij}+b_{ij})}}{(b_{ij})^{x_{ij}} e^{-b_{ij}}}, \tag{9.3}$$

where $\mathbf{x}$ is a vector of the observed data in all the bins. When dealing with many bins and channels, the LLR is simpler to compute and so more commonly used:

$$\text{LLR}(\mathbf{x}) = -2\ln\Lambda(\mathbf{x}) = \sum_{i}^{\text{channels}} \sum_{j}^{\text{bins}} \left[s_{ij} - x_{ij} \ln\left(1 + \frac{s_{ij}}{b_{ij}}\right)\right]. \tag{9.4}$$

A low LLR value implies that the data is more 'signal-like' and less 'background-like'. The LLR is the optimal way to distinguish a signal from background [147].

9.1.2 Pseudo-Experiments

Expected yields are affected by systematic uncertainties. They can be incorporated into the significance calculation with the use of pseudo-experiments, which combine several systematic uncertainties with the Poisson statistical probability distribution.

For each pseudo-experiment, a value for each source of systematic uncertainty (e.g. jet energy scale), is sampled at random from the pre-calculated uncertainty distribution which is most often Gaussian. The jet energy scale uncertainty, affects the event yields in the electron and muon channels roughly the same amount; it affects signal and background by different amounts. To account for such correlated uncertainties, the same values are used for both the electron and the muon channel and for both signal and background where appropriate. These values are used to generate an expected background yield and an expected signal yield. The signal (background) event yield for the pseudo-experiment is sampled from a Poisson distribution centered on the *expected* signal (background) event yield. A value of the

LLR is calculated both for the background-only yield and for the signal+background yield of each pseudo-experiment. Distributions of the background-only LLR and the signal+background LLR, based on many pseudo-experiments, are used to calculate confidence levels.

9.1.3 Confidence Levels

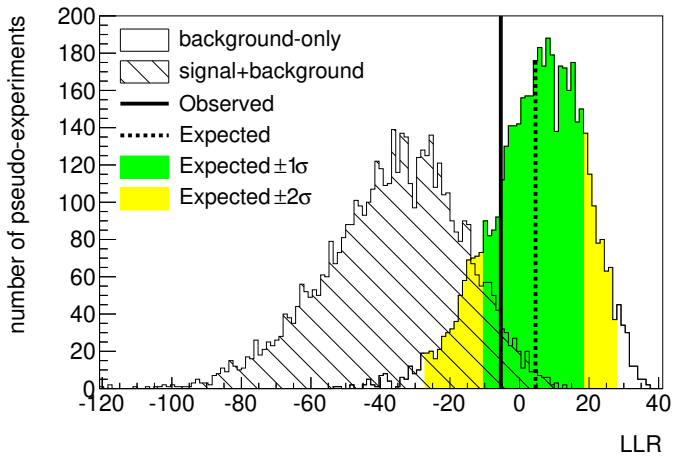

Figure 9.1: Log likelihood distributions for background-only and signal+background after 5,000 pseudo-experiments. The dotted vertical line gives expected LLR: the median of the background-only distribution. The green (yellow) band encloses 68% (95%) of background-only pseudo-experiments. The solid vertical line gives the observed value of the LLR.

Confidence levels (CL) are defined as fractions of the total number of pseudo-experiments. The strictly frequentist signal+background confidence level CL_{s+b} is the fraction of pseudo-experiments where the signal+background LLR is higher than the observed data $\mathbf{x}$; to the right of the solid line in Figure 9.1, where $CL_{s+b} = 0.040$. CL_{s+b} can be interpreted as the probability of observing data less signal-like than $\mathbf{x}$, for the signal+background yield in question. A small value of CL_{s+b} implies that the signal is unlikely to exist and can lead to an exclusion.

CL_b is the fraction of pseudo-experiments for which the background-only LLR is higher than the observed LLR; to the right of the solid line in Figure 9.1, where

$\mathrm{CL}_b = 0.79$. This can be interpreted as the probability of observing data less signal-like than $\mathbf{x}$ if there is no signal. If a signal-like excess is observed, a small value of $1 - \mathrm{CL}_b$ can lead to the rejection of the background-only hypothesis and a claim of a discovery. Commonly used 3σ and 5σ confidence levels correspond to values of $1 - \mathrm{CL}_b$ less than 2.7×10^{-3} and 4.3×10^{-7}, respectively.

Expected confidence levels are calculated by replacing the observed LLR with the median expected background-only LLR; the fraction of pseudo-experiments to the right of the *dotted* line in Figure 9.1. Confidence levels are also calculated for other points on the background-only LLR distribution; at either side of one-sigma and two-sigma uncertainty intervals, which include 68% and 95% of background-only outcomes respectively.

A difficult situation arises if the data does not agree with either the background-only or the signal+background hypotheses. It can lead to a strong exclusion of the signal while simultaneously calling the background prediction into question. One solution is to reduce the strength of the exclusion by instead using the modified frequentist confidence level:

$$\mathrm{CL}_s = \frac{\mathrm{CL}_{s+b}}{\mathrm{CL}_b} \tag{9.5}$$

CL_s gives a consistent and conservative measure of the confidence level, even if the data significantly disagrees with the expected background. The expected signal yield can be excluded at 95% confidence level when $1 - \mathrm{CL}_s > 0.95$. The signal shown in Figure 9.1 is excluded by a narrow margin.

The expected signal yield is proportional the production cross section of the KK graviton (σ) multiplied by its branching ratio (BR) to ZZ. In order to exclude a value of $\sigma \times \mathrm{BR}$, the expected signal yield is scaled by a discrete range of values and CL_s is calculated for each. The smallest value for which $1 - \mathrm{CL}_s > 0.95$ is taken as the limit. For the 750 GeV mass point, the smallest excluded signal is smaller than the nominal KK graviton signal by a factor of 0.66; as shown in Figure 9.1. Expected limits on $\sigma \times \mathrm{BR}$ with uncertainty bands are also calculated. These are values of $\sigma \times \mathrm{BR}$ for which the *expected* confidence level is small enough ($1 - \mathrm{CL}_s > 0.95$), calculated using either the median background-only LLR or the background-only

LLR ± 1 or $\pm 2\sigma$.

9.2 Limit Setting Procedure

Events were selected using the Low mass signal region for graviton samples with $m_{G^*} < 500$ GeV. For masses $m_{G^*} \geq 500$ GeV, the High mass signal region was used, and was combined with the Merged jet region for masses $m_{G^*} \geq 750$ GeV.

For each mass point and in each signal region, a window in the reconstructed graviton mass was chosen around the signal peak. The signal and background yields were then calculated in each window. For the Low and High mass signal regions, the windows were optimized by calculating expected cross section limits with full systematic uncertainties for a range of bin widths and positions. For the Merged jet signal region, larger-than-optimal windows were used in order to get a reliable estimate of the expected background yield in spite of low MC statistics. The window size was four times the mass resolution centered on the signal peak. In order to set limits on the bulk RS model, the window taken was double the mass resolution, centered on the signal peak; the Merged jet region was not used.

Systematic uncertainties from seven sources were incorporated for each bin: jet energy scale and resolution, jet mass scale, MC statistics, electron and muon identification efficiency and the model uncertainty. The model uncertainty was dominated by disagreement between the Z+jets prediction using Alpgen and Sherpa. Other uncertainties due to leptons and background cross sections, which each affected the background prediction by less than 1%, were covered by a constant value for all mass points. A global uncertainty of 3.7% was used for the luminosity uncertainty.

	JMS		JES		JER		Model	Other	MC stat.
	$+1\sigma$	-1σ	$+1\sigma$	-1σ	$+1\sigma$	-1σ			
Backgrounds:									
Z+jets	80%	-28%	14%	-15%	10%	0%	80%	3%	12%
Other Backgrounds	20%	-37%	20%	-22%	-22%	0%	40%	3%	6%
$G^* \to ZZ$:									
$m_{G^*} = 750$ GeV	31%	-31%	14%	-13%	2%	0%	–	10%	5%
$m_{G^*} = 1000$ GeV	10%	-12%	7%	-6%	1%	0%	–	10%	2%
$m_{G^*} = 1250$ GeV	6%	-11%	5%	-6%	-1%	0%	–	10%	2%

Table 9.1: Effect of various systematic uncertainties on the event yield in the Merged jet signal region. Model systematics are described in Chapter 6. The next most significant systematic uncertainties on the background are due to the lepton reconstruction and efficiency, and the background cross sections.

Source	Uncertainty
Trigger:	1%
Electron:	
E Resolution	$< 1\%$
E Scale	$< 1\%$
Reconstruction SF	1%
Identification SF	2%
Muon:	
p_T Resolution	$< 1\%$
p_T Scale	$< 1\%$
Identification SF	$< 1\%$

Table 9.2: Fractional uncertainties due to leptons.

Chapter 10

Results

10.1 Limits on excited (KK) gravitons

Limits on the production cross section of the KK graviton multiplied by its branching ratio to ZZ ($\sigma \times$ BR) were calculated independently for each signal region, shown in Figures 10.1 and 10.2. The effect of the large JMS uncertainty is shown to be modest. These limits were combined using using correlated systematic uncertainties where appropriate. Combined limits are shown in Figure 10.3 and Table 10.1. The Merged jet channel improves the limit on $\sigma \times$ BR of high mass signals by up to a factor of five.

By comparing limits on $\sigma \times$ BR to the leading order prediction in the RS1 signal model, they can be converted into a limit on the mass of the KK graviton in that model. Observed (expected) limits on the mass of the KK graviton in the RS1 model are 870 (950) GeV, as shown in Figure 10.3. Observed (expected) limits on the mass of the KK graviton in the bulk RS model are 630 (590) GeV, as shown in Figure 10.4.

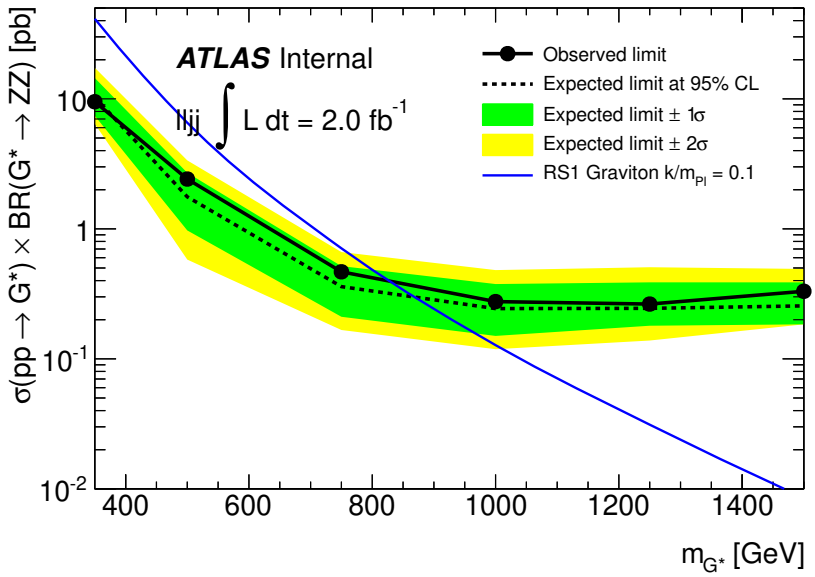

Figure 10.1: Limits on the cross section times branching ratio of the KK graviton in the RS1 model using the Resolved jets regions only. (Electron and Muon channels combined)

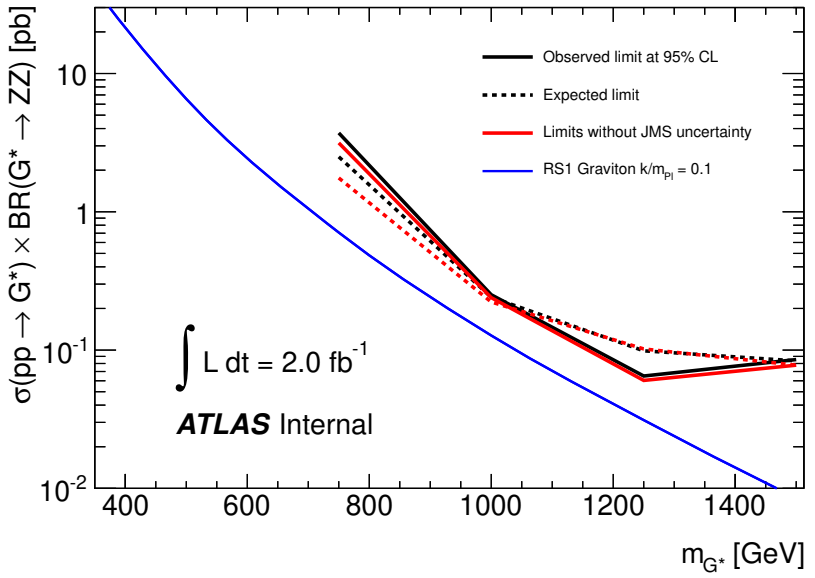

Figure 10.2: Comparison of sensitivity in the Merged jet region with and without the JMS uncertainty.

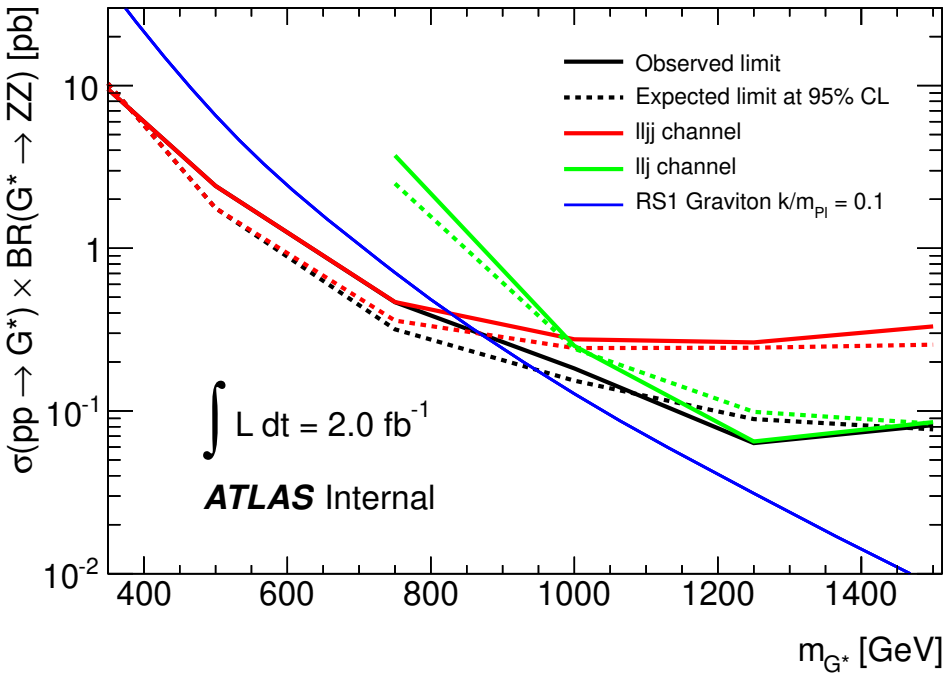

Figure 10.3: Combined limits on the cross section times branching ratio of the KK graviton in the RS1 model. Sensitivity in Merged jet ($\ell\ell j$) and Resolved jets ($\ell\ell jj$) regions can be compared.

m_{G^*} [GeV]	Observed Limit [fb]	Expected Limit [fb]
350	9500	10300
500	2400	1800
750	470	320
1000	180	150
1250	63	89
1500	82	77

Table 10.1: Limits on cross section times branching ratio of the KK graviton in the RS1 model, as shown in Figure 10.3.

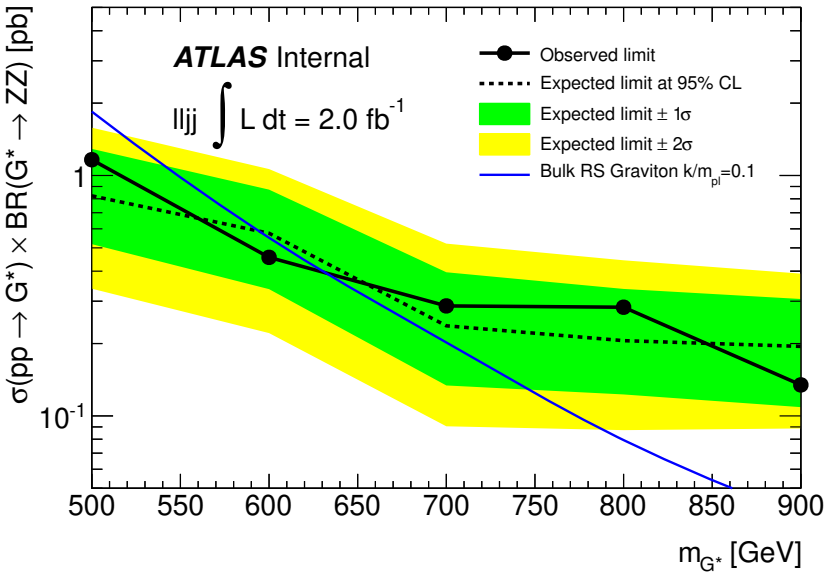

Figure 10.4: Limits on the cross section times branching ratio of the KK graviton in the bulk RS model.

10.2 Conclusions

The search presented in this thesis has set limits on anomalous production of a pair of gauge bosons (ZZ or WZ) from the decay of a narrow massive resonance over a range of masses from 350 GeV – 1.5 TeV. Limits on cross section times branching ratio substantially improve on previous searches. These limits are interpreted as limits on the mass of the graviton in two models of warped extra dimensions.

These results are currently being updated using all of the data taken in 2011, about 5 fb^{-1}. This search will also profit from an improved understanding of the ATLAS detector. For example, the methods used to model multiple proton collisions (pile-up) have been been extended in response to the greatly increasing luminosity. Many improvements in the object reconstruction and selection criteria have also been made, especially the track/cluster matching in electrons.

Searches for diboson resonances in several final states are currently in progress at ATLAS. In many cases, the results can be statistically combined to further improve sensitivity. Publications using the full 2011 data set are expected to include the following final states:

$$WW/WZ \to \ell\nu + \text{jets}$$

$$WW \to \ell\nu\ell\nu$$

$$WZ \to \ell\nu\ell\ell$$

$$ZZ \to \ell\ell\ell\ell$$

$$ZZ \to \ell\ell\nu\nu$$

The sensitivity in the $\ell\nu$ + jets channel is considerably improved by including a treatment of merged jets. An analysis along the lines of that presented here is in progress. Understanding of merged jets is especially important in two other final states, which gain from a large branching fraction but suffer from large backgrounds:

$$WZ/ZZ \to \nu\nu + \text{jets}$$

$$WW/WZ/ZZ \to \text{jets}$$

Analysis of these final states can particularly benefit from the use of more sophisticated 'jet substructure' variables. They are expected to contribute very significantly to the sensitivity to high mass resonances in the future.

Bibliography

[1] W. Pauli, "The Connection Between Spin and Statistics," *Phys. Rev.* **58** (Oct, 1940) 716–722.

[2] G. Kane, "The Dawn of Physics Beyond the Standard Model," *Scientific American* (June, 2003) .

[3] R. Feynman, *QED: The Strange Theory Of Light And Matter*. 1985.

[4] W. E. Lamb and R. C. Retherford, "Fine Structure of the Hydrogen Atom by a Microwave Method," *Phys. Rev.* **72** (Aug, 1947) 241–243.

[5] H. A. Bethe, "The Electromagnetic Shift of Energy Levels," *Phys. Rev.* **72** (Aug, 1947) 339–341.

[6] **Muon (g-2)** Collaboration, G. W. Bennett *et al.*, "Final report of the E821 muon anomalous magnetic moment measurement at BNL," *Phys. Rev. D* **73** (Apr, 2006) 072003.

[7] **Particle Data Group** Collaboration, K. Nakamura *et al.*, "Review of Particle Physics," *J. Phys. G* **37** (2010) 075021. `pdg.lbl.gov/2011/reviews/rpp2011-rev-g-2-muon-anom-mag-moment.pdf`.

[8] S. L. Glashow and S. Weinberg, "Natural conservation laws for neutral currents," *Phys. Rev. D* **15** (Apr, 1977) 1958–1965.

[9] S. L. Glashow, J. Iliopoulos, and L. Maiani, "Weak Interactions with Lepton-Hadron Symmetry," *Phys. Rev. D* **2** (Oct, 1970) 1285–1292.

[10] F. Englert and R. Brout, "Broken symmetry and the mass of gauge vector mesons," *Phys. Rev. Lett.* **13** (Aug, 1964) 321–323.

[11] P. W. Higgs, "Broken symmetries and the masses of gauge bosons," *Phys. Rev. Lett.* **13** (Oct, 1964) 508–509.

[12] G. S. Guralnik, C. R. Hagen, and T. W. B. Kibble, "Global conservation laws and massless particles," *Phys. Rev. Lett.* **13** (Nov, 1964) 585–587.

[13] V. Trimble, "Existence and Nature of Dark Matter in the Universe," *Ann. Rev. Astron. Astrophys.* **25** (1987) 425–472.

[14] G. Bertone, *Particle Dark Matter: Observations, Models and Searches*. Cambridge Univ. Press, Cambridge, 2010.

[15] L. Randall, "Extra Dimensions and Warped Geometries," *Science* **296** no. 5572, (2002) 1422–1427.

[16] L. Randall, *Warped Passages: Unravelling the Universe's Hidden Dimensions*. 2006.

[17] L. Randall and R. Sundrum, "A Large Mass Hierarchy from a Small Extra Dimension," *Phys. Rev. Lett.* **83** (1999) 3370–3373, `arXiv:hep-ph/9905221 [hep-ph]`.

[18] J. M. Maldacena, "The large N limit of superconformal field theories and supergravity," *Adv. Theor. Math. Phys.* **2** (1998) 231–252, `arXiv:hep-th/9711200`.

[19] E. Witten, "Anti-de Sitter space and holography," *Adv. Theor. Math. Phys.* **2** (1998) 253–291, `arXiv:hep-th/9802150 [hep-th]`.

[20] W. D. Goldberger and M. B. Wise, "Modulus Stabilization with Bulk Fields," *Phys. Rev. Lett.* **83** (1999) 4922–4925, `hep-ph/9907447`.

[21] M. A. Luty and R. Sundrum, "Radius stabilization and anomaly mediated supersymmetry breaking," *Phys. Rev.* **D62** (2000) 035008, arXiv:hep-th/9910202 [hep-th].

[22] P. J. Steinhardt, "General considerations of the cosmological constant and the stabilization of moduli in the brane world picture," *Phys. Lett.* **B462** (1999) 41–47, arXiv:hep-th/9907080 [hep-th].

[23] C. Csaki, M. Graesser, L. Randall, and J. Terning, "Cosmology of brane models with radion stabilization," *Phys. Rev.* **D62** (2000) 045015, arXiv:hep-ph/9911406 [hep-ph].

[24] E. E. Flanagan, S. H. H. Tye, and I. Wasserman, "Cosmological expansion in the Randall-Sundrum brane world scenario," *Phys. Rev.* **D62** (2000) 044039, arXiv:hep-ph/9910498 [hep-ph].

[25] H. B. Kim and H. D. Kim, "Inflation and gauge hierarchy in Randall-Sundrum compactification," *Phys. Rev.* **D61** (2000) 064003, arXiv:hep-th/9909053 [hep-th].

[26] G. F. Giudice, R. Rattazzi, and J. D. Wells, "Graviscalars from higher dimensional metrics and curvature Higgs mixing," *Nucl. Phys.* **B595** (2001) 250–276, arXiv:hep-ph/0002178 [hep-ph].

[27] D. Kazakov, S. Lavignac, and J. Dalibard (editors), "Particle Physics beyond the Standard Model,". Proceedings, Summer School on Theoretical Physics, 84th Session, Les Houches, France, August 1-26, 2005.

[28] T. Gherghetta, "Les Houches lectures on warped models and holography," arXiv:hep-ph/0601213 [hep-ph].

[29] H. Davoudiasl, J. Hewett, and T. Rizzo, "Bulk gauge fields in the Randall-Sundrum model," *Phys. Lett.* **B473** (2000) 43–49, arXiv:hep-ph/9911262 [hep-ph].

[30] A. Pomarol, "Grand unified theories without the desert," *Phys. Rev. Lett.* **85** (2000) 4004–4007, arXiv:hep-ph/0005293 [hep-ph].

[31] L. Randall and M. D. Schwartz, "Quantum field theory and unification in AdS_5," *JHEP* **0111** (2001) 003, arXiv:hep-th/0108114 [hep-th].

[32] M. S. Carena, E. Ponton, T. M. Tait, and C. Wagner, "Opaque branes in warped backgrounds," *Phys. Rev.* **D67** (2003) 096006, arXiv:hep-ph/0212307 [hep-ph].

[33] H. Davoudiasl, J. Hewett, and T. Rizzo, "Brane localized kinetic terms in the Randall-Sundrum model," *Phys. Rev.* **D68** (2003) 045002, arXiv:hep-ph/0212279 [hep-ph].

[34] S. Chang, J. Hisano, H. Nakano, N. Okada, and M. Yamaguchi, "Bulk standard model in the Randall-Sundrum background," *Phys. Rev.* **D62** (2000) 084025, arXiv:hep-ph/9912498 [hep-ph].

[35] S. J. Huber and Q. Shafi, "Fermion masses, mixings and proton decay in a Randall-Sundrum model," *Phys. Lett.* **B498** (2001) 256–262, arXiv:hep-ph/0010195 [hep-ph].

[36] image courtesy of Flip Tanedo.

[37] Y. Grossman and M. Neubert, "Neutrino masses and mixings in nonfactorizable geometry," *Phys. Lett.* **B474** (2000) 361–371, arXiv:hep-ph/9912408 [hep-ph].

[38] T. Gherghetta, "Dirac neutrino masses with Planck scale lepton number violation," *Phys. Rev. Lett.* **92** (2004) 161601, arXiv:hep-ph/0312392 [hep-ph].

[39] R. Contino, Y. Nomura, and A. Pomarol, "Higgs as a Holographic Pseudo-Goldstone boson," *Nucl. Phys.* **B671** (2003) 148–174, arXiv:hep-ph/0306259 [hep-ph].

[40] K. Agashe, R. Contino, and A. Pomarol, "The Minimal Composite Higgs model," *Nucl. Phys.* **B719** (2005) 165–187, arXiv:hep-ph/0412089 [hep-ph].

[41] K. Agashe and R. Contino, "The Minimal Composite Higgs Model and Electroweak Precision Tests," *Nucl. Phys.* **B742** (2006) 59–85, arXiv:hep-ph/0510164 [hep-ph].

[42] M. S. Carena, E. Ponton, J. Santiago, and C. Wagner, "Electroweak constraints on warped models with custodial symmetry," *Phys. Rev.* **D76** (2007) 035006, arXiv:hep-ph/0701055 [hep-ph].

[43] M. E. Peskin and T. Takeuchi, "New constraint on a strongly interacting Higgs sector," *Phys. Rev. Lett.* **65** (Aug, 1990) 964–967.

[44] K. Agashe, A. Delgado, M. J. May, and R. Sundrum, "RS1, Custodial Isospin and Precision Tests," *JHEP* **0308** (2003) 050, arXiv:hep-ph/0308036 [hep-ph].

[45] K. Agashe, R. Contino, L. Da Rold, and A. Pomarol, "A Custodial symmetry for Zb anti-b," *Phys.Lett.* **B641** (2006) 62–66, arXiv:hep-ph/0605341 [hep-ph].

[46] H. Davoudiasl, S. Gopalakrishna, E. Ponton, and J. Santiago, "Warped 5-Dimensional Models: Phenomenological Status and Experimental Prospects," *New J. Phys.* **12** (2010) 075011, arXiv:0908.1968 [hep-ph].

[47] A. L. Fitzpatrick, J. Kaplan, L. Randall, and L.-T. Wang, "Searching for the Kaluza-Klein Graviton in Bulk RS Models," *JHEP* **0709** (2007) 013, arXiv:hep-ph/0701150 [hep-ph].

[48] K. Agashe, H. Davoudiasl, G. Perez, and A. Soni, "Warped Gravitons at the LHC and Beyond," *Phys. Rev.* **D76** (2007) 036006, arXiv:hep-ph/0701186 [hep-ph].

[49] K. Agashe, A. Belyaev, T. Krupovnickas, G. Perez, and J. Virzi, "LHC Signals from Warped Extra Dimensions," *Phys. Rev.* **D77** (2008) 015003, arXiv:hep-ph/0612015 [hep-ph].

[50] B. Lillie, L. Randall, and L.-T. Wang, "The Bulk RS KK-gluon at the LHC," *JHEP* **0709** (2007) 074, arXiv:hep-ph/0701166 [hep-ph].

[51] **ATLAS** Collaboration, G. Aad *et al.*, "Search for high-mass dilepton resonances with 5 fb^{-1} of pp collisions at $\sqrt{s} = 7$ TeV with the ATLAS experiment," Tech. Rep. ATLAS-CONF-2012-007, CERN, Geneva, Mar, 2012.

[52] **ATLAS** Collaboration, G. Aad *et al.*, "Search for Extra Dimensions using diphoton events in 7 TeV proton-proton collisions with the ATLAS detector," arXiv:1112.2194 [hep-ex].

[53] **D0** Collaboration, V. M. Abazov *et al.*, "Search for resonant WW and WZ production in ppbar collisions at $\sqrt{s} = 1.96$ TeV," *Phys. Rev. Lett.* **107** (2011) 011801, arXiv:1011.6278 [hep-ex].

[54] **ATLAS** Collaboration, G. Aad *et al.*, "Search for new particles decaying to ZZ using final states with leptons and jets with the ATLAS detector in $\sqrt{s} = 7$ TeV proton-proton collisions," arXiv:1203.0718 [hep-ex].

[55] **ATLAS** Collaboration, G. Aad *et al.*, "A Search for $t\bar{t}$ Resonances in the Lepton Plus Jets Channel using 2.05 fb^{-1} of pp Collisions at $\sqrt{s} = 7$ TeV," Tech. Rep. ATLAS-CONF-2012-029, CERN, Geneva, Mar, 2012.

[56] M. Benedikt, P. Collier, V. Mertens, J. Poole, and K. Schindl, *LHC Design Report*. CERN, Geneva, 2004.

[57] A. M. Sessler and E. J. N. Wilson, *Engines of Discovery: A Century of Particle Accelerators*. World Scientific, Singapore, 2007.

[58] E. J. N. Wilson, *An Introduction to Particle Accelerators*. Oxford Univ. Press, Oxford, 2001.

[59] CERN, *LEP Design Report*. Geneva, 1984.

[60] L. Rossi, "Superconductivity: Its Role, Its Success and Its Setbacks in the Large Hadron Collider of CERN.," *Supercond. Sci. Technol.* **23** (Jan, 2010) 034001.

[61] Fermilab, "Proton-proton collider upgrade (new Main Injector, new Tevatron)," tech. rep., 1988.

[62] R. R. Wilson, "The Tevatron," *Phys. Today* **30N10** (1977) 23–30.

[63] I. Brock and T. Schorner-Sadenius, *Physics at the Terascale*. John Wiley & Sons, 2011.

[64] Commissariat à l'Énergie Atomique et aux Énergies Alternatives (CEA), "Superconducting magnets for the LHC," *Clef* (Winter, 2007) .

[65] **ATLAS** Collaboration, G. Aad *et al.*, "Luminosity Determination in pp Collisions at $\sqrt{s} = 7$ TeV Using the ATLAS Detector at the LHC," *Eur. Phys. J. C* **71** (2011) 1630, `arXiv:hep-ex/1101.2185 [hep-ex]`.

[66] **ATLAS** Collaboration, G. Aad *et al.*, "Luminosity Determination in pp Collisions at $\sqrt{s} = 7$ TeV using the ATLAS Detector in 2011," Tech. Rep. ATLAS-COM-CONF-2011-130, CERN, Geneva, Jul, 2011.

[67] S. Baird, "Accelerators for pedestrians," Tech. Rep. CERN-AB-Note-2007-014, CERN, Geneva, Feb, 2007.

[68] M. Perricone, "Hitting the broad side of a (classified) barn," *Symmetry Magazine* **3** (Feb, 2006) .

[69] G. Antchev, P. Aspell, I. Atanassov, V. Avati, J. Baechler, *et al.*, "First measurement of the total proton-proton cross section at the LHC energy of $\sqrt{s} = 7$ TeV," *Europhys. Lett.* **96** (2011) 21002, `arXiv:1110.1395 [hep-ex]`.

[70] **ATLAS** Collaboration, G. Aad *et al.*, "Measurement of the Inelastic Proton-Proton Cross-Section at $\sqrt{s}$=7 TeV with the ATLAS Detector.," *Nature Commun.* **2** (Apr, 2011) 463. 19 p, `arXiv:1104.0326 [hep-ex]`.

[71] CERN, "Summary of the Analysis of the 19 September 2008 Incident at the LHC," *Technical report* (Oct, 2008) .

[72] CERN, "Linac2 Website." `http://linac2.home.cern.ch/linac2`.

[73] **PS** Collaboration, "40 years of CERN's Proton Synchrotron," *CERN Courier* (Nov, 1999) . `http://cerncourier.com/cws/article/cern/28138`.

[74] **UA1** Collaboration, G. Arnison *et al.*, "Experimental observation of isolated large transverse energy electrons with associated missing energy at $\sqrt{s} = 540$ GeV," *Phys. Lett.* **B122** (1983) 103–116.

[75] **UA1** Collaboration, G. Arnison *et al.*, "Experimental observation of lepton pairs of invariant mass around 95 GeV/c^2 at the CERN SPS collider," *Phys. Lett.* **B126** (1983) 398–410.

[76] **UA2** Collaboration, P. Bagnaia *et al.*, "Evidence for $Z^0 \to e^+e^-$ at the CERN anti-p p collider," *Phys. Lett.* **B129** (1983) 130–140.

[77] CERN DSU Communications Group, "Ask An Expert service." `http://askanexpert.web.cern.ch`.

[78] **ALPHA** Collaboration, "Resonant quantum transitions in trapped antihydrogen atoms," *Nature* **483** no. 7390, (Mar, 2012) 439–443.

[79] **CLOUD** Collaboration, "Role of sulphuric acid, ammonia and galactic cosmic rays in atmospheric aerosol nucleation," *Nature* **476** no. 7361, (Aug, 2011) 429–433.

[80] L. R. Evans and P. Bryant, "LHC Machine," *J. Instrum.* **3** (2008) S08001. 164 p.

[81] **ATLAS** Collaboration, G. Aad *et al.*, "ATLAS Experiment at the CERN Large Hadron Collider," *JINST* **3** (2008) S08003.

[82] **Particle Data Group** Collaboration, K. Nakamura *et al.*, "Review of Particle Physics," *J. Phys. G* **37** (2010) 075021.

[83] T. LeCompte and H. T. Diehl, "The CDF and D0 Upgrades for Run II," *Annual Review of Nuclear and Particle Science* **Vol. 50: 71-177** (Dec, 2000) .

[84] A. Ceccucci, "Calorimeters for present and future accelerators: a Status Report," *Nucl. Instrum. Meth.* **A461** no. 1-3, (2001) 10 – 16.

[85] W. Cleland and E. Stern, "Signal processing considerations for liquid ionization calorimeters in a high rate environment," *Nucl. Instrum. Meth. in Physics Research Section A: Accelerators, Spectrometers, Detectors and Associated Equipment* **A338** no. 2-3, (1994) 467 – 497.

[86] M. Aharrouche *et al.*, "Measurement of the response of the ATLAS liquid argon barrel calorimeter to electrons at the 2004 combined test-beam," *Nucl. Instr. Meth.* **614** (2010) 400.

[87] **ATLAS** Collaboration, G. Aad *et al.*, "Drift Time Measurement in the ATLAS Liquid Argon Electromagnetic Calorimeter using Cosmic Muons," *European Physical Journal C* **70** (Dec., 2010) 755–785, `arXiv:1002.4189 [physics.ins-det]`.

[88] **ATLAS** Collaboration, G. Aad *et al.*, "Readiness of the ATLAS liquid argon calorimeter for LHC collisions," *European Physical Journal C* **70** (Dec., 2010) 723–753, `arXiv:0912.2642 [physics.ins-det]`.

[89] F. Ragusa and L. Rolandi, "Tracking at LHC," *New J. Phys.* **9** no. 9, (2007) 336.

[90] **ATLAS** Collaboration, G. Aad *et al.*, "ATLAS muon spectrometer: Technical Design Report," tech. rep., CERN, Geneva, 1997.

[91] **ATLAS** Collaboration, G. Aad *et al.*, "Updated Luminosity Determination in pp Collisions at $\sqrt{s} = 7$ TeV using the ATLAS Detector," Tech. Rep. ATLAS-CONF-2011-011, CERN, Geneva, Mar, 2011.

[92] **ATLAS** Collaboration, G. Aad *et al.*, "Luminosity Determination in pp Collisions at $\sqrt{s} = 7$ TeV Using the ATLAS Detector at the LHC," *Eur. Phys. J.* **C71** (2011) 1630, `arXiv:1101.2185 [hep-ex]`.

[93] S. van der Meer, "Calibration of the effective beam height in the ISR.," Tech. Rep. CERN-ISR-PO-68-31. ISR-PO-68-31, CERN, Geneva, 1968.

[94] **ATLAS** Collaboration, G. Aad *et al.*, "Performance of the ATLAS Trigger System in 2010," *Eur. Phys. J.* **C72** (2012) 1849, `arXiv:1110.1530 [hep-ex]`.

[95] **ATLAS** Collaboration, G. Aad *et al.*, "The ATLAS Simulation Infrastructure," *Eur. Phys. J.* **C70** (Dec, 2010) 823–874, `arXiv:1005.4568 [physics.ins-det]`.

[96] **GEANT4** Collaboration, S. Agostinelli *et al.*, "GEANT4: A Simulation toolkit," *Nucl. Instr. Meth.* **A506** (2003) 250.

[97] T. Sjostrand, S. Mrenna, and P. Z. Skands, "PYTHIA 6.4 Physics and Manual," *JHEP* **0605** (2006) 026, `arXiv:hep-ph/0603175 [hep-ph]`.

[98] G. Corcella, I. Knowles, G. Marchesini, S. Moretti, K. Odagiri, P. Richardson, M. Seymour, and B. Webber, "HERWIG6: an event generator for hadron emission reactions with interfering gluons (including supersymmetric processes)," *JHEP* **0101** (2001) 010.

[99] P. Lenzi and J. Butterworth, "A Study on Matrix Element corrections in inclusive Z/γ^* production at LHC as implemented in PYTHIA, HERWIG, ALPGEN and SHERPA," `arXiv:0903.3918 [hep-ph]`.

[100] S. Frixione and B. R. Webber, "Matching NLO QCD computations and

parton shower simulations," *JHEP* **0206** (2002) 029, arXiv:hep-ph/0204244 [hep-ph].

[101] J. M. Campbell and R. K. Ellis, "Next-to-leading order corrections to $W+2$ jet and $Z+2$ jet production at hadron colliders," *Phys. Rev.* **D65** (2002) 113007, arXiv:hep-ph/0202176 [hep-ph].

[102] M. L. Mangano, M. Moretti, F. Piccinini, R. Pittau, and A. D. Polosa, "AlpGen, a generator for hard multiparton processes in hadronic collisions," *JHEP* **07** (2003) 001, arXiv:hep-ph/0206293.

[103] T. Gleisberg, S. Hoeche, F. Krauss, M. Schoenherr, S. Schumann, F. Siegert, and J. Winter, "Event generation with Sherpa 1.1," *JHEP* **2009** no. 02, (2009) 007.

[104] S. Hoeche, F. Krauss, N. Lavesson, L. Lonnblad, M. Mangano, *et al.*, "Matching parton showers and matrix elements," arXiv:hep-ph/0602031 [hep-ph].

[105] M. Mangano, "The so-called MLM prescription for ME/PS matching," October, 2002. Talk presented at the Fermilab ME/MC Tuning Workshop.

[106] S. Catani, F. Krauss, R. Kuhn, and B. Webber, "QCD matrix elements + parton showers," *JHEP* **0111** (2001) 063, arXiv:hep-ph/0109231 [hep-ph].

[107] F. Krauss, "Matrix elements and parton showers in hadronic interactions," *JHEP* **0208** (2002) 015, arXiv:hep-ph/0205283 [hep-ph].

[108] J. Butterworth, J. R. Forshaw, and M. Seymour, "Multiparton interactions in photoproduction at HERA," *Z. Phys.* **C72** (1996) 637–646, arXiv:hep-ph/9601371 [hep-ph].

[109] J. Pumplin *et al.*, "New generation of parton distributions with uncertainties from global QCD analysis," *JHEP* **0207** (2002) 012, arXiv:hep-ph/0201195.

[110] P. M. Nadolsky *et al.*, "Implications of CTEQ global analysis for collider observables," *Phys. Rev. D* **78** (2008) 013004, arXiv:hep-ph/0802.0007 [hep-ph].

[111] A. Martin, W. Stirling, R. Thorne, and G. Watt, "Parton distributions for the LHC," *Eur. Phys. J. C* **63** (2009) 189, arXiv:hep-ph/0901.0002 [hep-ph].

[112] K. Agashe, H. Davoudiasl, S. Gopalakrishna, T. Han, G.-Y. Huang, *et al.*, "LHC Signals for Warped Electroweak Neutral Gauge Bosons," *Phys. Rev.* **D76** (2007) 115015, arXiv:0709.0007 [hep-ph].

[113] A. Pukhov, "CalcHEP 2.3: MSSM, structure functions, event generation, batchs, and generation of matrix elements for other packages," arXiv:hep-ph/0412191 [hep-ph].

[114] A. Datta, K. Kong, and K. T. Matchev, "Minimal universal extra dimensions in CalcHEP/CompHEP," *New J. Phys.* **12** no. 7, (2010) 075017.

[115] M. Botje, J. Butterworth, A. Cooper-Sarkar, A. de Roeck, J. Feltesse, *et al.*, "The PDF4LHC Working Group Interim Recommendations," arXiv:1101.0538 [hep-ph].

[116] R. Gavin, Y. Li, F. Petriello, and S. Quackenbush, "FEWZ 2.0: A code for hadronic Z production at next-to-next-to-leading order," *Comput. Phys. Commun.* **182** (2011) 2388, arXiv:hep-ph/1011.3540 [hep-ph].

[117] **ATLAS** Collaboration, G. Aad et al, "Measurement of the $W \to \ell\nu$ production cross-section and observation of $Z \to \ell\ell$ production in proton-proton collisions at $\sqrt{s} = 7$ TeV with the ATLAS detector," Tech. Rep. ATLAS-CONF-2010-051, CERN, Geneva, Jul, 2010.

[118] S. Moch and P. Uwer, "Theoretical status and prospects for top-quark pair production at hadron colliders," *Phys. Rev. D* **78** (2008) 034003, arXiv:0804.1476 [hep-ph].

[119] N. Kidonakis, "Next-to-next-to-leading logarithm resummation for s-channel single top quark production," *Phys. Rev. D* **81** (Mar, 2010) 054028.

[120] N. Kidonakis, "Next-to-next-to-leading-order collinear and soft gluon corrections for t-channel single top quark production," *Phys. Rev. D* **83** (May, 2011) 091503.

[121] **ATLAS** Collaboration, G. Aad *et al.*, "Measurement of the WW cross section in $\sqrt{s} = 7$ TeV pp collisions with ATLAS," *Phys. Rev. Lett.* **107** (2011) 041802, `arXiv:1104.5225 [hep-ex]`.

[122] **ATLAS** Collaboration, G. Aad *et al.*, "Measurement of the WZ production cross section and limits on anomalous triple gauge couplings in proton-proton collisions at $\sqrt{s} = 7$ TeV with the ATLAS detector," *Phys. Lett. B* (2011) , `arXiv:1111.5570 [hep-ex]`.

[123] **ATLAS** Collaboration, G. Aad *et al.*, "Measurement of the ZZ production cross section and limits on anomalous neutral triple gauge couplings in proton-proton collisions at $\sqrt{s} = 7$ TeV with the ATLAS detector," *Phys. Rev. Lett.* **108** (2012) 041804, `arXiv:1110.5016 [hep-ex]`.

[124] **ATLAS** Collaboration, G. Aad *et al.*, "Search for a heavy Standard Model Higgs boson in the channel $H \to ZZ \to llqq$ using the ATLAS detector," *Phys. Lett.* **B707** (2012) 27–45, `arXiv:1108.5064 [hep-ex]`.

[125] M. Aharrouche *et al.*, "Measurement of the response of the ATLAS liquid argon barrel calorimeter to electrons at the 2004 combined test-beam," *Nucl. Instr. Meth.* **A614** no. 3, (2010) 400 – 432.

[126] M. Aharrouche *et al.*, "Response uniformity of the ATLAS liquid argon electromagnetic calorimeter," *Nucl. Instr. Meth.* **A582** (Nov., 2007) 429–455, `arXiv:0709.1094 [physics.ins-det]`.

[127] **ATLAS** Collaboration, G. Aad *et al.*, "Electron performance measurements

with the ATLAS detector using the 2010 LHC proton-proton collision data," *Eur. Phys. J. C* (2011) , arXiv:1110.3174 [hep-ex].

[128] **ATLAS** Collaboration, G. Aad *et al.*, "Muon Momentum Resolution in First Pass Reconstruction of pp Collision Data Recorded by ATLAS in 2010," Tech. Rep. ATLAS-CONF-2011-046, CERN, Geneva, Mar, 2011.

[129] **ATLAS** Collaboration, G. Aad *et al.*, "Muon reconstruction efficiency in reprocessed 2010 LHC proton-proton collision data recorded with the ATLAS detector," *ATLAS-CONF-2011-063* (2011) .

[130] G. P. Salam, "Towards Jetography," *Eur. Phys. J.* **C67** (2010) 637–686, arXiv:0906.1833 [hep-ph].

[131] image courtesy of Kerstin Perez.

[132] S. D. Ellis and D. E. Soper, "Successive combination jand othersgorithm for hadron collisions," *Phys. Rev.* **D48** (1993) 3160–3166, arXiv:hep-ph/9305266 [hep-ph].

[133] M. Cacciari, G. P. Salam, and G. Soyez, "The Anti-k(t) jet clustering algorithm," *JHEP* **0804** (2008) 063, arXiv:0802.1189 [hep-ph].

[134] Y. L. Dokshitzer, G. Leder, S. Moretti, and B. Webber, "Better jet clustering algorithms," *JHEP* **9708** (1997) 001, arXiv:hep-ph/9707323 [hep-ph].

[135] M. Wobisch and T. Wengler, "Hadronization corrections to jet cross-sections in deep inelastic scattering," arXiv:hep-ph/9907280 [hep-ph].

[136] **L3** Collaboration, P. Achard *et al.*, "Inclusive jet production in two-photon collisions at LEP," *Phys. Lett.* **B602** (2004) 157–166, arXiv:hep-ex/0410012 [hep-ex].

[137] **ATLAS** Collaboration, G. Aad *et al.*, "Jet energy measurement with the ATLAS detector in proton-proton collisions at $\sqrt{s} = 7$ TeV," *Eur. Phys. J. C.* (2011) , arXiv:1112.6426 [hep-ex].

[138] **ATLAS** Collaboration, G. Aad *et al.*, "Jet energy scale and its systematic uncertainty in proton-proton collisions at $\sqrt{s} = 7$ TeV in ATLAS 2010 data," Tech. Rep. ATLAS-CONF-2011-032, CERN, Geneva, Mar, 2011.

[139] **ATLAS** Collaboration, G. Aad *et al.*, "Measurement of Jet Mass and Substructure for Inclusive Jets in $\sqrt{s} = 7$ TeV pp Collisions with the ATLAS Experiment," Tech. Rep. ATLAS-CONF-2011-073, CERN, Geneva, May, 2011.

[140] **ATLAS** Collaboration, G. Aad *et al.*, "Data-Quality Requirements and Event Cleaning for Jets and Missing Transverse Energy Reconstruction with the ATLAS Detector in Proton-Proton Collisions at a Center-of-Mass Energy of $\sqrt{s} = 7$ TeV," *ATLAS-CONF-2010-038* (2010) . `http://cdsweb.cern.ch/record/1277678`.

[141] **ATLAS** Collaboration, G. Aad *et al.*, "Performance of Missing Transverse Momentum Reconstruction in Proton-Proton Collisions at 7 TeV with ATLAS," *Eur. Phys. J.* **C72** (2012) 1844, `arXiv:1108.5602 [hep-ex]`.

[142] **ATLAS** Collaboration, G. Aad *et al.*, "Measurement of the production cross section for W-bosons in association with jets in pp collisions at $\sqrt{s} = 7$ TeV with the ATLAS detector," *Phys. Lett.* **B698** (2011) 325–345, `arXiv:1012.5382 [hep-ex]`.

[143] **ATLAS** Collaboration, G. Aad *et al.*, "Search for strong gravity signatures in same-sign dimuon final states using the ATLAS detector at the LHC," *Phys. Lett. B* **709** (2012) 322–340, `arXiv:1111.0080 [hep-ex]`.

[144] **D0** Collaboration, W. Fisher, "Systematics and limit calculations," tech. rep. FERMILAB-TM-2386-E.

[145] T. Junk, "Confidence level computation for combining searches with small statistics," *Nucl. Instrum. Meth.* **A434** (1999) 435–443, `arXiv:hep-ex/9902006 [hep-ex]`.

[146] A. L. Read, "Modified frequentist analysis of search results (the CL_s method),". `https://cdsweb.cern.ch/record/451614`. CERN-OPEN-2000-205.

[147] J. Neyman and E. S. Pearson, "On the problem of the most efficient tests of statistical hypotheses," *Phil. Trans. R. Soc. Lond.* **A231** no. 694-706, (1933) 289–337.